

Computational Study of Layered Zeolite MFI and Titanium-substituted Zeolite LTA and their Applications in Catalysis

Thesis submitted for the degree of Doctor of Philosophy (PhD), authored by

Carlos Ernesto Hernandez Tamargo

Supervisor:

Prof Nora H. de Leeuw

University College London

Department of Chemistry

September 2017

Declaration:

I, Carlos E. Hernandez Tamargo confirm that the work presented in this thesis is my own. Where information has been derived from other sources, I confirm that this has been indicated in the thesis.

Carlos E. Hernandez Tamargo

September 2017

Abstract

In this thesis, we have examined the layered morphology of zeolite MFI and the titanium substitution of zeolite LTA by using a combination of density functional theory and interatomic potential-based calculations. Layered MFI zeolite allows a straightforward hierarchization of the pore system which accelerates mass transfer and increases its lifetime as a catalyst. We have performed a theoretical study of the structural features of the pure-silica and aluminium-substituted MFI nanosheets. We have analysed the effects of aluminium substitution on the vibrational properties of silanols as well as the features of protons as counter-ions. The formation of the two-dimensional system did not lead to appreciable distortions within the framework, whilst dehydration of aluminium-substituted silanols is both kinetic and thermodynamically favoured. In addition, we have analysed the strength of Brønsted acid (BA) sites located at the internal and external surfaces of zeolite MFI by adsorbing trimethylphosphine oxide (TMPO) as a probe molecule and correlating structural information to experimental ^{31}P NMR data. We have been able to provide a possible explanation to the variable strength of the BA sites probed by TMPO by considering the basicity of the centres sharing the acid proton.

In addition, we have examined the possible role of the Lewis acid sites located at the external surface of zeolite MFI to catalyse the tautomerization of phenolic-type compounds. The tautomerization has been conceived as a three-step process involving two protons transfers between the molecule and the zeolite, and the rotation of a dihedral angle. The energy barrier of each step is lower than 55 kJ/mol, suggesting that this transformation is easily accessible under standard reaction conditions.

Finally, we have studied the structural, electronic and mechanical properties of the pure-silica zeolite LTA, as well as the single and double titanium-substituted material. The energetics of the titanium distribution within the zeolite framework suggest that the inclusion of a second titanium atom with configurations Ti-(Si)₀-Ti, Ti-(Si)₁-Ti and Ti-(Si)₂-Ti is more favourable than the mono-substitution. The energetics of the dissociation of water on these Lewis acid sites indicate that this process is only favoured when two titanium atoms form a two-membered ring (2MR) sharing both hydroxy groups, Ti-(OH)₂-Ti, showing that the presence of water may tune the distribution of titanium atoms within the framework of zeolite LTA.

Table of Content

Abstract	3
List of Publications.....	11
List of Conference Presentations.....	12
List of Figures	13
List of Tables.....	25
Chapter 1 Introduction	28
1.1 Zeolites – General Overview.....	28
1.1.1 Zeolite Structure.....	28
1.1.2 Framework Type Codes	29
1.1.3 Zeolite Synthesis and Composition	30
1.1.4 Micropore System of Zeolites.....	33
1.1.5 Applications	34
1.2 Zeolite MFI.....	35
1.3 Zeolite LTA	37
1.4 Two-dimensional Zeolites	39
1.5 Role of Zeolites in the Conversion of Lignin	41
1.6 Objectives of the Thesis	44
Chapter 2 Theoretical Methods	47
2.1 The Monoelectronic Approximation	47

2.2 Density Functional Theory	51
2.2.1 Hohenberg and Kohn's Theorems	51
2.2.2 Kohn-Sham Method.....	52
2.2.3 The Generalized Gradient Approximation (GGA)	55
2.2.4 Calculation of Forces	56
2.3 Periodic Systems.....	57
2.3.1 Bloch Theorem.....	58
2.3.2 Plane Wave Basis Set.....	60
2.3.3 The Pseudopotential Approximation	61
2.4 Analysis of the Electronic Structure	64
2.4.1 Density of States	64
2.4.2. Electronic Charge Density	65
2.4.3 Bader Charge Analysis	65
2.5 Dispersion Forces Correction	66
2.6 Geometry Optimization and Vibrational Analysis	68
2.6.1 Local Minimization Techniques	69
2.6.2 Molecular Dynamics	71
2.6.3 Vibrational Analysis	72
2.7 Methods to Evaluate Reaction Barriers	74
2.8 Born Model of Solids	76
2.8.1 Core-Shell Approximation.....	78

Chapter 3 Structure of MFI Nanosheets.....	80
3.1 Introduction	80
3.2 Computational Methods	83
3.3 Pure-silica MFI.....	85
3.3.1 Bulk Structure	85
3.3.2 Nanosheet Structure	88
3.4 Aluminium-substituted MFI.....	91
3.4.1 Bulk Structure	91
3.4.2 Nanosheet Structure	94
3.5 Silanols and Al-substituted Silanols.....	95
3.6 Lewis Centre Formation	99
3.7 Protonated Framework Oxygen Atoms	103
3.8 Projected Density of States.....	106
3.9 Chapter Conclusions.....	109
Chapter 4 Adsorption of Trimethylphosphine Oxide at the Internal and External Surfaces of Zeolite MFI	111
4.1. Introduction	111
4.2 Computational Methods	113
4.2.1 Classification of the Acid Strength.....	116
4.3 Adsorption of one TMPO Molecule.....	118
4.4 Adsorption of two TMPO Molecules	121
4.5 Adsorption of three TMPO Molecules	124

4.6 Full Deprotonation of the Brønsted Acid Site	130
4.7 Chapter Conclusions	134
Chapter 5 Zeolite-mediated Tautomerization of Phenol and Catechol	136
5.1 Introduction	136
5.2 Computational Methods	139
5.3 Slab Model and Aluminium Distribution	143
5.4 Adsorption of Phenol	146
5.4.1 Dissociation of Phenol	147
5.4.2 Rotation of Dissociated Phenol	150
5.4.3 Formation of Cyclohexa-2,4-dien-1-one	152
5.5 Adsorption of Catechol	154
5.5.1 Dissociation of Catechol	156
5.5.2 Formation of Catechol-derived Cyclo-hexadienones	161
5.6 Chapter Conclusions	164
Chapter 6 Periodic Modelling of zeolite Ti-LTA	166
6.1 Introduction	166
6.2 Computational Methods	167
6.2.1 DFT Calculations	167
6.2.2 Interatomic Potential Calculations	169
6.2.3 Simulation Model	170
6.2.4 Elastic Properties	171

6.3 Pure-silica Zeolite LTA	173
6.4 Ti-substituted Zeolite LTA	175
6.5 Electronic Structure	180
6.6 Vibrational Analysis	181
6.7 Hydration of Ti-substituted Zeolite LTA	185
6.8 Chapter Conclusions	192
Chapter 7 Conclusions and Future Work	194
7.1 Summary and Conclusions	194
7.2 Future Work	198
Appendix A. Chapter 3	202
A.1 Pure-silica Bulk Zeolite MFI	202
A.2 Pure-silica Zeolite MFI Nanosheet	203
A.3 Termination of Surface (010) of Zeolite MFI	204
A.4 Aluminium-substituted Zeolite MFI Nanosheet	206
A.5 Boltzmann Distribution and O-H Stretching Frequencies	207
References	209

Acknowledgments

Firstly, I want to thank my supervisor Prof Nora H. de Leeuw for giving me the unique opportunity of developing my academic education at the University College London and Cardiff University.

Secondly, I would like to express my gratitude to Dr Alberto Roldan for invaluable help and assistance during the entire duration of my PhD, and Dr Abdelaziz Essadek for always having something nice to say.

I give special attention to my fellow countrymen: Dr David Santos and Dr Sergio E. Ruiz. David and his wife Yolanda helped me from the first day I arrived in the United Kingdom. David and Yolanda's support made my life much easier at the beginning of this three-year experience, and they became my small family at Wembley. And Sergio, for his incessant promptitude to provide advice and guidance.

To my lovely Giuly, with whom I really started to speak English and has been the partner I always wanted. We have walked side-by-side all this time, and I hope, we will continue marching together.

Finally, to the members of my close family, my grandmother Bertina, my dad Ernesto, my mom Mercedes and my little sister Elisa, for all their support and love.

List of Publications

The content of this thesis has been published in the following papers:

- 1.- **C.E. Hernandez-Tamargo**, A. Roldan, N.H. de Leeuw, A density functional theory study of the structure of pure-silica and aluminium-substituted MFI nanosheets, *J. Solid State Chem.* 237 (2016) 192–203. doi:10.1016/j.jssc.2016.02.006.
- 2.- **C.E. Hernandez-Tamargo**, A. Roldan, N.H. de Leeuw, DFT Modeling of the Adsorption of Trimethylphosphine Oxide at the Internal and External Surfaces of Zeolite MFI, *J. Phys. Chem. C.* 120 (2016) 19097–19106. doi:10.1021/acs.jpcc.6b03448.
- 3.- **C.E. Hernandez-Tamargo**, A. Roldan, N.H. de Leeuw, Density functional theory study of the zeolite-mediated tautomerization of phenol and catechol, *Journal of Molecular Catalysis. A, Chemical* 433 (2017) 334–345. doi: 10.1016/j.mcat.2016.12.020.

To be published:

- 4.- **C.E. Hernandez-Tamargo**, A. Roldan, Phuti E. Ngoepe, N.H. de Leeuw, Periodic Modelling of Zeolite Ti-LTA, *submitted to the Journal of Chemical Physics*.
- 5.- **C.E. Hernandez-Tamargo**, A. Roldan, N.H. de Leeuw, Tautomerization of Phenol at the External Lewis Acid Sites of Sc-, Fe- and Ga-substituted Zeolite MFI, *in preparation*.

List of Conference Presentations

2015 10th SEADIM workshop in the “San Gerónimo” University College of Havana, Havana, Cuba. “*Exploring the Interaction of Trimethylphosphine Oxide with MFI zeolite: a DFT study*” **Oral Presentation.**

2015 CHITEL (Congress of Theoretical Chemistry of Latin Expression), Torino, Italy. “*MFI Nanosheets Characterized by Density Functional Theory Calculations*” **Poster Presentation**

2015 14th Southwest Computational Chemists Graduate Meeting, Bristol University, UK. “*DFT study of the perceived acidity of zeolites using trimethylphosphine oxide as probe molecule*” **Oral Presentation**

2016 Modelling of Advanced Functional Materials using Terascale Computing, University of Cardiff, Wales. “*DFT study of the perceived acidity of zeolites using trimethylphosphine oxide as probe molecule*” **Poster Presentation**

2016 Cardiff Catalysis Institute (CCI) Cardiff Conference, Cardiff University, UK. “*Modelling of the tautomerization of phenol mediated by zeolite MFI*” **Poster Presentation**

2016 Three-month visit to the Materials Modelling Centre (MMC), University of Limpopo, South Africa, under the supervision of Prof Phuti E. Ngoepe (from 15 September 2016 to 11 November 2016).

List of Figures

- Figure 1-1.** (a) Tetrahedral site; the red and orange balls represent oxygen and T atoms, respectively. (b) Smallest secondary building unit (SBU), labelled 3. (c) Unit cell of JST framework type (space group $Pa\bar{3}$) which is formed by the repetition of SBU 3. (d) Biggest SBU, labelled 8-8. (e) Unit cell of MER framework type (space group $I4mmm$) which is formed by the repetition of SBU 8-8. From (b) to (e) the oxygen atoms are not represented and the radius of the T atoms reduced for an enhanced view.29
- Figure 1-2.** Approved Framework Type Codes (FTC) by the Structure Commission of the International Zeolite Association (IZA) (Reproduced from IZA official webpage, <http://america.iza-structure.org/IZA-SC/ft.php>).30
- Figure 1-3.** Representation of the substitution of silicon by aluminium atoms in (a) one and (b) two T-sites of a zeolite. Counter-ions that balance the spare negative charge after the substitution: (c) proton, (d) metal cation M^{1+} and (e) metal cation M^{2+}32
- Figure 1-4.** Representation of the most frequent zeolite pore diameters: (a) 8MR, (b) 10MR and (c) 12MR. (d) Representation of the straight pore of the EON type.33
- Figure 1-5.** Schematic representation of (a) one-dimensional, (b) two-dimensional and (c) three-dimensional zeolite pore systems.34
- Figure 1-6.** (a) SBU of the MFI framework, labelled 5-1. (b) Pentasil unit. (c) Chain of pentasil units along the c direction, a single pentasil unit is highlighted in blue. (d) Pentasil layer formed by replication of the chain on the ac plane. (e) Pentasil layer formed by replication of the chain on the bc plane. The pentasil chain is

enclosed by red boxes. (f) Representation of the MFI framework on the <i>ab</i> plane, the <i>ac</i> and <i>bc</i> pentasil layers are enclosed by blue boxes.	36
Figure 1-7. Representation of the (a) SBU 6-2, (b) β -cage, (c) α -cage and (d) double 4-membered ring (D4R). The edges of the cubic unit cell are represented by black lines.	38
Figure 1-8. Di-quaternary ammonium surfactant used as bifunctional SDA to synthesize MFI nanosheets (adapted from Ref [52] with permission from Nature Publishing Group).	40
Figure 1-9. Representation of the MFI nanosheet as well as the bifunctional SDA (adapted from Ref [52] with permission from Nature Publishing Group).	40
Figure 1-10. Representation of the polymeric structure of lignin and its structural building blocks: coumaryl, coniferyl and synapyl alcohols (adapted from Ref [60] with permission from The Royal Society of Chemistry).	42
Figure 1-11. Representation of phenol tautomerization.	43
Figure 2-1. Representation of the exploration of the potential energy surface by the (a) steepest descents and (b) conjugated gradients methods.	70
Figure 2-2. Definition of the dimer in the 3n-space (adapted from Ref [135] with permission from AIP Publishing LLC).	75
Figure 3-1. (a) Lateral view of the three-pentasil slab (the framework is created by linking the silicon atoms, oxygen atoms are not shown). The pentasil layer at the centre of the slab is contained between dotted lines. The twenty four silicon atoms per unit cell at the external surface and those of the straight channel are highlighted with darker bonds. The sinusoidal channels run along the interception of two pentasil layers. (b) Top view of the three pentasil slab. The sinusoidal channel which connects neighbouring straight channels is highlighted with darker bonds.	82

Figure 3-2. MFI zeolite unit cell. The oxygen atoms were deleted for better view. The framework is created by linking the silicon atoms. The section in red represents the twelve non-equivalent T-sites with their numeration.....86

Figure 3-3. Pure-silica slabs formed by two (a) and three (b) pentasil layers; the black lines denote the supercell box. The silanol hydrogen atoms are oriented towards their nearest silanol groups. Following this scheme two configurations for the hydrogen atoms are obtained, labelled along the text as configuration A (c) and B (d). The silicon atoms are located at the interception of the grey sticks and the framework oxygens were eliminated for a better view. The silanol oxygens are represented with dark grey balls and the hydrogens with light pink balls. Each silanol is labelled according to the numbers of the T-site and oxygen atom that carries the hydrogen.....89

Figure 3-4. Scattering of the T-O distances (a), O-T-O angles (b) and T-O-T angles (c) for the framework T-sites and oxygen atoms in the Al-substituted bulk (horizontal lines in black) and two-pentasil slab (horizontal lines in blue). The horizontal lines establish the scattering ranges for the distances and angles; the average values are marked with small vertical lines. The structural scheme, besides each set of lines, highlights in red the distance or the angle to which the range of values is referring.92

Figure 3-5. Structural schemes representing the different types of silanol groups at the external surface of the zeolite: silanol of the pure-silica slab; *type (i)*, silanol whose silicon atom does not have the aluminium as nearest neighbour; *type (ii)*, silanol whose silicon atom is directly connected to the aluminium through the non-protonated oxygen; *type (iii)*, silanol whose silicon atom is directly connected to the

aluminium through the protonated oxygen; and *type (iv)*, aluminium-substituted silanol.96

Figure 3-6. Local structure for different aluminium-substituted sites highlighting the features of specific hydrogen-bonds. The silicon atoms are located at the interception of the light grey sticks, and the non-important oxygens are not shown for a better view. Silanol oxygens and framework oxygens involved in the hydrogen-bonds are represented with dark grey balls, the hydrogens with light pink balls and the aluminium with a black ball.97

Figure 3-7. Energy profile of the dehydration reaction of aluminium-substituted silanol T9-O25, when the proton is binding the oxygen atoms O8 (a), O18 (b) and O9 (c). The formation of a 2MR with a vicinal silanol group, once the Lewis center has been created, is considered (d). The Nudge Elastic Band Method (NEB) was used to optimize the structures along the reaction path [132,133]. The aluminium atom is represented with a black ball, oxygens with dark grey balls, hydrogens with light pink balls, and silicons are located at the interception of the light grey sticks. 100

Figure 3-8. Local structure of the aluminium-substituted zeolite framework. (a) Aluminium substitution at the T12 site, the silanol oxygen atom O24 is labelled for reference within the text. (b) Aluminium substitution at the T8 site, the protonated oxygen atom O12 is labelled for reference within the text. Silanol oxygens and framework oxygens are represented with dark grey balls, the hydrogens with light pink balls and the aluminium with a black ball. The silicons are located at the interception of the light grey sticks. 107

Figure 3-9. Projected density of states (PDOS) of the O(2p) states (black) and total DOS (grey, reduced 100 times with respect to O(2p) projections). (a) Silanol oxygen

O24 in pure-silica slab. (b) Silanol oxygen O24 when the aluminium substitution takes place at the T12 site of the slab (see **Figure 3-8a**). (c) Framework oxygen O12 at the external surface of the pure-silica slab. (d) Protonated oxygen O12 when the aluminium substitution takes place at the T8 site of the slab (see **Figure 3-8b**). The Fermi energy (0.0 eV) is highlighted with a dotted line. 108

Figure 4-1. Representation of the BA sites at the internal (bottom, left panel) and at the external (bottom, right panel) surfaces. One of the two pentasil layers that form the slab is identified by a black-line rectangle (top, right panel). The Al-substituted T2-site (light blue ball) with the proton (white ball) at the O1 position (red ball) are shown. The rest of the O atoms and silanol OH groups were deleted for a better view; Si atoms are represented by orange sticks. A molecule of trimethylphosphine oxide is shown in the bottom-right corner; H is represented in white, C in grey, P in brown and O in red. 114

Figure 4-2. Correlation of the $O_{(P)}-H$ distances and the ^{31}P chemical shifts using Zheng *et al.* data (black squares linked with black lines) [195]. The experimental classification of the acid sites of the zeolite MFI according to the TMPO ^{31}P chemical shift is indicated by vertical dashed blue lines [30,57]. The experimental classification is used to extrapolate the expected $O_{(P)}-H$ distances from its interception with the theoretical curve (indicated by red circles); the corresponding distance values are written above the horizontal dashed black lines. The spectrum of $O_{(P)}-H$ distances is divided into three zones taking the middle points between the extrapolated $O_{(P)}-H$ distances. These zones are shaded alternately in light grey and white, corresponding to (top) *weak* acids, (centre) *strong* acids, and (bottom) *very-strong* acids; the limits of each range are indicated by the red numbers at the left-hand side of the graph. 117

Figure 4-3. Representation of the interaction of a single TMPO molecule with (a, b) the internal, and (c, d) the external BA sites after local optimization; H in white, C in grey, P in brown, O in red, Al in light blue and Si represented by orange sticks. All the framework O atoms (except the protonated one), and silanol OH groups were deleted for an enhanced view. Related structural values are presented in Table 4-1	119
Figure 4-4. Configuration after 10 ps of MD simulation of the locally optimized structure in Figure 4-3b	121
Figure 4-5. Representation of the adsorption of two TMPO molecules on (a) the internal and (b) the external BA sites after local optimization. H in white, C in grey, P in brown, O in red, Al in light blue and Si represented by orange sticks. All the framework O atoms (except the protonated one), and silanol OH groups were deleted for an enhanced view. Related structural values are presented in Table 4-3	122
Figure 4-6. Representation of two TMPO molecules on (a) the internal BA site and (b) the external BA site after 10 ps of MD simulation of the locally optimized structure in Figure 4-5	123
Figure 4-7. Representation of the adsorption of three TMPO molecules on (a) the internal and (b) the external BA sites after local optimization. H in white, C in grey, P in brown, O in red, Al in light blue and Si represented by orange sticks. All the framework O atoms (except the protonated one), and silanol OH groups were deleted for an enhanced view. The interaction between one of the non-protonated TMPO and the Al atom is represented by a stick connecting $O_{(P2)}$ to the Al atom. Related structural values are presented in Table 4-5	126
Figure 4-8. Charge difference isosurfaces with values of 0.005 bohr^{-3} calculated from (4-1). (a) Internal BA site, (b) external BA site. The structures correspond to	

those shown in **Figure 4-7**. H in white, C in grey, P in brown, O in red, Al in light blue and Si represented by orange sticks. All the framework O atoms (except the protonated one), and silanol OH groups were deleted for an enhanced view. 127

Figure 4-9. Projected density of states (PDOS) of (a) O(p_2)(2p), (b) Al(3s) and (c) Al(3p) for the 3TMPO/1BA configuration observed in the cavity according to **Figure 4-7a**. PDOS of (d) Al(3s) and (e) Al(3p) for the structure without the non-protonated TMPO that interacts with the Al centre. 128

Figure 4-10. Representation of (a, c) TMPOH^+ and (b, d) $(\text{TMPO})_2\text{H}^+$ at more than 5 Å away from the BA site after local optimization. (a, b) Internal surface, (c, d) external surface. H in white, C in grey, P in brown, O in red and Si represented by orange sticks. All the framework O atoms (except the protonated one), and silanol OH groups were deleted for an enhanced view. Related structural values are presented in **Table 4-8**. 132

Figure 5-1. Top and lateral views of the optimized unit cell of the zeolite MFI. One of the two pentasil layers is highlighted within red lines. The O atoms are deleted for an enhanced view. Vicinal Si atoms are linked by orange sticks. 140

Figure 5-2. Lateral view of MFI slabs formed by (a) two and (b) one pentasil layer. (c) Top view of the slab with the numeration of the twelve non-equivalent T sites (balls in light blue). The framework O atoms are deleted for an enhanced view, silanol O atoms are shown in red, H in white. Vicinal Si atoms are linked by orange sticks. 144

Figure 5-3. (a) Lateral and (b) top views of the slab formed by one pentasil layer loaded with one molecule of tetramethyl ammonium. The Al substitution at T1 site is included as an example. The framework O atoms are deleted for an enhanced view,

silanol O atoms are shown in red, H in white, C in grey, N in dark blue and Al in light blue. Vicinal Si atoms are linked by orange sticks. 144

Figure 5-4. (a) Relative energy of the Al substitution at each non-equivalent T-site within the slabs formed by one and two pentasil layers. (b, c) Variation of the diameter of the straight pore considering the distances $d_{(T1-T7)}$ and $d_{(T6-T12)}$, and comparing against the values $d_{0(T1-T7)}$ and $d_{0(T6-T12)}$ of the pure silica zeolite. 145

Figure 5-5. (a) Non-planar and (b) co-planar adsorption configurations of phenol on the T9 site before optimization, setting an initial $O_{ph}-Al$ distance of 2.5 Å. The numeration of the C atoms is included in configuration (a). (c) Non-planar and (d) co-planar adsorptions with the strongest binding free energies after geometry optimization. Selected interatomic distances are included together with the binding free energy (*FBind.*). Most of the framework O atoms are deleted for an enhanced view, relevant O atoms are shown in red, H in white, C in dark grey and Al in light blue. Vicinal Si atoms are linked by orange sticks. 147

Figure 5-6. Optimized geometries after the transfer of H_{ph} to the closest framework O atom binding the Al. (a) Non-planar adsorption, (b) co-planar adsorption. Selected interatomic distances are included together with binding free energies (*FBind.*). Most of the framework O atoms are deleted for an enhanced view, relevant O atoms are shown in red, H in white, C in dark grey and Al in light blue. Vicinal Si atoms are linked by orange sticks. 148

Figure 5-7. Tautomerization pathways for the adsorption of phenol with (a) non-planar and (b) co-planar configurations of adsorbed phenol. The horizontal dashed line marks the reference energy (shifted to zero), constituted by the bare zeolite and a molecule of phenol in the gas phase. 150

- Figure 5-8.** Representations of successive geometries along the rotation pathways that places the C2 atom at favourable distance from H_{ph}. (a) Non-planar and (b) co-planar configurations..... 151
- Figure 5-9.** Optimized geometries after the rotation of the aromatic ring of the phenoxide adsorbed on the T9 site. (a) Non-planar and (b) co-planar configurations. Selected interatomic distances are included together with the binding free energies (*FBind.*). Most of the framework O atoms are deleted for an enhanced view, relevant O atoms are shown in red, H in white, C in dark grey and Al in light blue. Vicinal Si atoms are linked by orange sticks. 151
- Figure 5-10.** Optimized geometries of (a) non-planar and (b) co-planar configurations after the transfer of H_{ph} to the C2 of the phenoxide adsorbed on the T9 site. Selected interatomic distances are included together with the binding free energies (*FBind.*). Most of the framework O atoms are deleted for an enhanced view, relevant O atoms are shown in red, H in white, C in dark grey and Al in light blue. Vicinal Si atoms are linked by orange sticks. 153
- Figure 5-11.** Orientations of the catechol molecule. Orientation (a) is more stable than (b) by 67 kJ/mol (including zero-point energy and entropy corrections at 437 K)..... 154
- Figure 5-12.** Optimized geometries with the strongest binding free energies of catechol on Lewis acid site T9: monodentate adsorption (MOA) with (a) non-planar configuration and (b) co-planar configuration; bidentate adsorption (BIA) with (c) non-planar configuration and (d) co-planar configuration; the co-planar BIA relaxed to co-planar MOA. Selected interatomic distances are included together with the binding free energy (*FBind.*). Most of the framework O atoms are deleted for an

enhanced view, relevant O atoms are shown in red, H in white, C in dark grey and Al in light blue. Vicinal Si atoms are linked by orange sticks. 156

Figure 5-13. Optimized geometries after the H_{1ph} transfer of catechol to the closest framework O atom binding the Al. Representation of the MOA with (a) non-planar configuration and (b) co-planar configuration, and the BIA with (c) non-planar configuration and (d) co-planar configuration. Selected interatomic distances are included together with the binding free energy (F_{Bind}). Most of the framework O atoms are deleted for an enhanced view, relevant O atoms are shown in red, H in white, C in dark grey and Al in light blue. Vicinal Si atoms are linked by orange sticks. 158

Figure 5-14. Optimized TS_1 geometries for the transfer of catechol H_{1ph} to the closest framework O atom binding the Al. Representation of the MOA with (a) non-planar configuration and (b) co-planar configuration, and the BIA with (c) non-planar configuration and (d) co-planar configuration. Selected interatomic distances are included together with the binding free energy (F_{Bind}). Most of the framework O atoms are deleted for an enhanced view, relevant O atoms are shown in red, H in white, C in dark grey and Al in light blue. Vicinal Si atoms are linked by orange sticks. 160

Figure 5-15. Catechol-derived cyclo-hexadienones from the MOA with non-planar configuration. (a) cyclohexa-3,5-dien-2-hydroxy-1-one, derived from the H_{1ph} transfer to C2 that binds the second O_{2ph} ; (b) cyclohexa-2,4-dien-2-hydroxy-1-one, derived from the H_{1ph} transfer to C6. Hydrogen atoms are shown in white, C in dark grey and O in red. Relevant dihedral and bond angles, together with interatomic distances are shown. 161

Figure 6-1. Boltzmann distributions at 125 °C for the double Ti-substituted zeolite LTA as a function of the separation between the two Ti atoms within the framework. Segments of the optimized structures are shown for the peaks with significant probability. (a) The GGA using a 72-atom unit cell, (b) the IP method using a 576-atom supercell and considering only double substitutions within the same unit cell out of eight available and (c) IP using a 576-atom supercell and considering the full set of double substitution along the supercell. The number within the label of each peak specifies the number of Si atoms that bridge the two Ti atoms, the letter is only to specify the order of appearance..... 176

Figure 6-2. Representation of the isosurfaces of the electronic charge density associated with the unoccupied electronic band of lowest energy of relevant structures (0.0007 bohr^{-3}). (a) pure-silica LTA, (b) single Ti substitution, (c) 0_a and (d) 2_a. The framework O atoms are deleted for clarity, Ti atoms are represented by light blue balls and Si atoms by orange sticks. 181

Figure 6-3. Simulated infrared spectra of relevant structures (from bottom to top): pure-silica LTA (pure-Si), LTA with a single Ti substitution (1Ti), configuration 0_a and configuration 2_a. The labelling of each spectrum contains within parenthesis the level of theory with which it was simulated: the GGA or the IP method. 183

Figure 6-4. Representation of the adsorption of water in (a) the α -cage and (b) the β -cage, taking as an example the optimized structures of single Ti-substituted LTA. The framework O atoms are deleted for clarity, the water O atom is represented by a red ball, H atoms by white balls, Ti atoms by light blue balls and the silicon atoms by orange sticks..... 185

Figure 6-5. Representation of the optimized structure for the adsorption of water on 0_a opposite to the bridging O between the two Ti atoms. This adsorption takes place

- from loading in the α -cage. The framework O atoms are deleted for clarity (the only exception is the bridging O atom between the two Ti atoms), water O atoms are represented by red balls, H atoms by white balls, Ti atoms by light blue balls and the Si atoms by orange sticks. 186
- Figure 6-6.** Close-ups of the optimized structures of the two-membered rings (2MR) with different degree of Ti substitution. (a) 2MR for pure-silica zeolite, (b) 2MR for single Ti-substituted zeolite, and (c) 2MR for double Ti-substituted zeolite. (d) Location of the 2MR within the framework using the optimized structure of pure-silica zeolite as an example, the close-up specifies the labels used to distinguish the different atoms of the 2MR. The framework O atoms are deleted for clarity, the O atoms of the 2MR are represented by red balls, H atoms by white balls, Ti atoms by light blue balls and the Si atoms by orange sticks..... 187
- Figure 6-7.** Optimized structure for the adsorption of water forming 2Ti-2MR after the O-H bond dissociation. The close-up shows the LUMO of the material. The framework O atoms are deleted for clarity (except the bridging O between the two Ti atoms), the water O atom is represented by red balls, the H by white balls, the Ti atoms by light blue balls and the Si atoms by orange sticks. 190
- Figure 6-8.** Simulated IR spectra of the different 2MRs and their comparison with their equivalent structures without adsorbate. (From bottom to top) Pure-silica LTA (**pure-Si**), and **2Si-2MR**; single Ti-substituted LTA (**1Ti**) and **Si,Ti-2MR**; double Ti-substituted, with the Ti configuration shown in **Figure 6-7** and labelled as **0_b**, and **2Ti-2MR**. The splitting of one of the bands associated with D4R is marked with vertical arrows. 192

List of Tables

Table 3-1. Cell vectors and bulk modulus (B) of the orthorhombic MFI zeolite ($Pnma$) calculated with Interatomic Potentials (IP), pure PBE and GGA together with the long-range dispersion correction (PBE+D2).	87
Table 3-2. Summary for the O-H vibration frequency [$\nu(\text{O-H})$] and O-H bond distance (O-H dist.) of the different types of silanol groups within the pure-silica and aluminium-substituted slabs. Three values are given for each entry: minimum, average (bold numbers within parenthesis) and maximum values. The silanol types are represented in Figure 3-5	96
Table 3-3. Classification of the protons according to the framework oxygen binding them within the BULK and SLAB . The classification ranges from Inaccessible protons to Accessible protons . Also, accessible protons may be further divided into those with and without <i>intra-framework H-bonds</i> . Additionally, the oxygen-hydrogen bond distance (O-H dist.), its stretching frequency [$\nu(\text{O-H})$] and the hydrogen distance to the nearest framework oxygen atom are provided (OH\cdotsO).	104
Table 4-1. Relevant interatomic distances (\AA) of the 1TMPO/1BA configurations shown in Figure 4-3 (a to d) after local optimization.	119
Table 4-2. Relevant interatomic distances (\AA) after 10 ps of MD simulation taking the 1TMPO/1BA configurations shown in Figure 4-3 (a to d) as input geometries.	120
Table 4-3. Relevant interatomic distances (\AA) of the 2TMPO/1BA configurations shown in Figure 4-5 (a, b) after local optimization.	122

Table 4-4. Relevant interatomic distances (\AA) after 10 ps of MD simulation taking the 2TMPO/1BA configurations shown in Figure 4-5 (a, b) as input geometries.	124
Table 4-5. Relevant interatomic distances (\AA) of the 3TMPO/1BA configurations shown in Figure 4-7 (a, b) after local optimization.	126
Table 4-6. Relevant interatomic distances (\AA) for six different configurations 3TMPO/1BA after local optimization.....	129
Table 4-7. Relevant interatomic distances (\AA) after 10 ps of MD simulation taking the 3TMPO/1BA configurations shown in Figure 4-7 (a, b) as input geometries.	130
Table 4-8. Relevant interatomic distances (\AA) of the full protonated TMPO molecules at more than 5 \AA from the BA site.	132
Table 5-1. Structural parameters after optimization of the bulk unit cell of the zeolite MFI with the PBE functional in combination with the Grimme's methods (D2 and D3) that account for the Van der Waals interactions.	140
Table 5-2. Binding free energies (in kJ/mol) of each of the species involved in the tautomerization of catechol starting from the structures in Figure 5-12 (the barrier for the ring rotation is not included).....	157
Table 6-1. Optimized cell parameter a (\AA), average and standard deviation of the Si-O bond distance (\AA), O-Si-O and Si-O-Si angles ($^\circ$). Elastic constants C_{11} , C_{12} and C_{44} (GPa), bulk modulus B (GPa), shear modulus G (GPa), BG ratio, Young's modulus Y (GPa), Poisson's ratio σ and shear anisotropic factor A , obtained with the GGA and the IP method.	173
Table 6-2. Summary of average values and standard deviations of the T-O bond distances (\AA), O-T-O and T-O-T angles ($^\circ$) in the LTA structure (T=Si and Ti)	

obtained with the GGA and the IP method. The energy difference between the conduction and the valence bands Δ_{LUMO} (eV) obtained with the GGA is also listed for the electronic calculations. 179

Table 6-3. The energy difference between the conduction and the valence bands Δ_{LUMO} (eV) obtained with the GGA..... 180

Table 6-4. Vibrational frequencies (cm^{-1}) of the simulated IR spectra of **Figure 6-3**.
^a 181

Table 6-5. T-O distance (\AA) (T = Si and Ti), O-O distance (\AA), O-H distance (\AA) and relative energy against the non-dissociated water (kJ/mol) of different 2MRs.
 188

Chapter 1 Introduction

1.1 Zeolites – General Overview

1.1.1 Zeolite Structure

Zeolites are aluminosilicate materials with defined crystalline structure and micropore architecture. Tetrahedral TO_4 sites (in short T-sites) are the primary building units of zeolites (see **Figure 1-1a**), which are linked through the oxygen atoms at their corners forming secondary building units (SBU). The SBUs are non-chiral structures that consist of up to 16 T-sites. One SBU or a combination of SBUs forms the entire framework of any zeolite. **Figure 1-1** shows the smallest and biggest reported SBUs, which involve 3 and 16 T-sites and are labelled 3 and 8-8, respectively. For instance, the SBU 3 forms the JST framework type whilst MER type is one of the few frameworks made of 8-8 SBUs (see **section 1.1.2** for an explanation regarding these three-letter acronyms) [1].

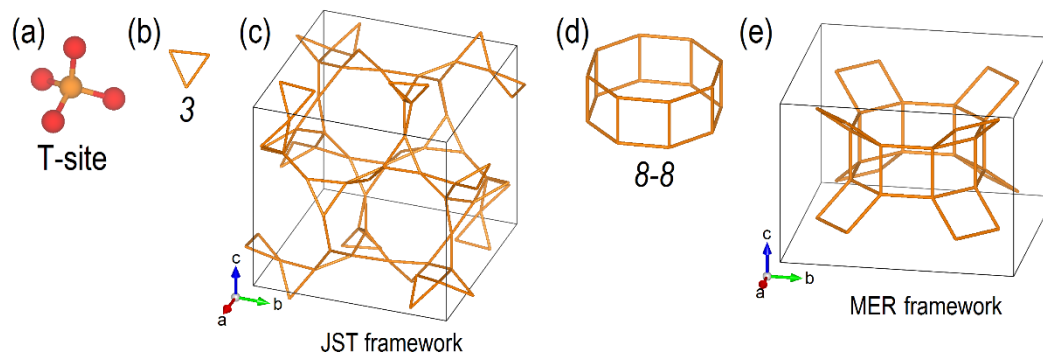


Figure 1-1. (a) Tetrahedral site; the red and orange balls represent oxygen and T atoms, respectively. (b) Smallest secondary building unit (SBU), labelled 3. (c) Unit cell of JST framework type (space group $Pa\bar{3}$) which is formed by the repetition of SBU 3. (d) Biggest SBU, labelled 8-8. (e) Unit cell of MER framework type (space group $I4/mmm$) which is formed by the repetition of SBU 8-8. From (b) to (e) the oxygen atoms are not represented and the radius of the T atoms reduced for an enhanced view.

1.1.2 Framework Type Codes

At present, the International Zeolite Association (IZA) recognizes 232 unique frameworks, either from natural or synthetic origins, and to each of them is assigned a framework type code (FTC) for identification (see **Figure 1-2**). The FTC is a three-letter acronym that identifies each distinctive zeolite framework and is derived from the name of the material used to determine the structure. For instance, AFG refers to the mineral **A**fghanite [2] and MTN designates the synthetic zeolite ZSM-39 (Zeolite Socony **M**obil – **T**hirty **N**ine) [3]. The last and 232th FTC to be approved by the Structure Commission of the IZA is denoted by ETL, and corresponds to the material H-EU-12 [4].

ABW	ACO	AEI	AEL	AEN	AET	AFG	AFI	AFN	AFO	AFR	AFS
AFT	AFV	AFX	AFY	AHT	ANA	APC	APD	AST	ASV	ATN	ATO
ATS	ATT	ATV	AVL	AWO	AWW	BCT	*BEA	BEC	BIK	BOF	BOG
BOZ	BPH	BRE	BSV	CAN	CAS	CDO	CFI	CGF	CGS	CHA	-CHI
-CLO	CON	CSV	CZP	DAC	DDR	DFO	DFT	DOH	DON	EAB	EDI
EEI	EMT	EON	EPI	ERI	ESV	ETL	ETR	EUO	*-EWT	EZT	FAR
FAU	FER	FRA	GIS	GIU	GME	GON	GOO	HEU	IFO	IFR	-IFU
IFW	IFY	IHW	IMF	IRN	IRR	-IRY	ISV	ITE	ITG	ITH	*-ITN
ITR	ITT	-ITV	ITW	IWR	IWS	IWV	IWW	JBW	JNT	JOZ	JRY
JSN	JSR	JST	JSW	KFI	LAU	LEV	LIO	-LIT	LOS	LOV	LTA
LTF	LTJ	LTL	LTN	MAR	MAZ	MEI	MEL	MEP	MER	MFI	MFS
MON	MOR	MOZ	*MRE	MSE	MSO	MTF	MTN	MTT	MTW	MVY	MWF
MWW	NAB	NAT	NES	NON	NPO	NPT	NSI	OBW	OFF	OKO	OSI
OSO	OWE	-PAR	PAU	PCR	PHI	PON	POS	PSI	PUN	RHO	-RON
RRO	RSN	RTE	RTH	RUT	RWR	RWY	SAF	SAO	SAS	SAT	SAV
SBE	SBN	SBS	SBT	SEW	SFE	SFF	SFG	SFH	SFN	SFO	SFS
*SFV	SFW	SGT	SIV	SOD	SOF	SOS	SSF	*-SSO	SSY	STF	STI
*STO	STT	STW	-SVR	SVV	SZR	TER	THO	TOL	TON	TSC	TUN
UEI	UFI	UOS	UOV	UOZ	USI	UTL	UWY	VET	VFI	VNI	VSV
WEI	-WEN	YUG	ZON								

Figure 1-2. Approved Framework Type Codes (FTC) by the Structure Commission of the International Zeolite Association (IZA) (Reproduced from IZA official webpage, <http://america.iza-structure.org/IZA-SC/ft.php>).

1.1.3 Zeolite Synthesis and Composition

Zeolites are commonly synthesized from an aqueous solution containing the source of framework atoms, a mineralizing agent and a structure directing agent (SDA). Hydroxyl or fluoride anions are usually used as the mineralizing agents, whilst the SDA can be an inorganic alkaline cation or a charged organic molecule such as a quaternary ammonium cation. During the reaction, the solution transforms into a gel-like system under temperatures that range from 100 to 200 °C [5–7]. The zeolite pore system is generated after removing the organic SDAs from the framework usually by calcination or chemical transformation, conserving the crystalline structure of the

material. The first report regarding the use of organic SDAs to synthesize zeolites was presented by Barrer and Denny, who employed tetraalkylammonium cations to prepare faujasites (FAU) and sodalites (SOD) [8]. Since then, a wide range of novel SDAs has been developed to finely tune the zeolite topology and pore architecture [9]. There exist effective experimental and computational techniques that allow to monitor and analyse the formation and growth of zeolite crystals, such as atomic force microscopy (AFM), high-resolution scanning electron microscopy (HRSEM) and Monte-Carlo simulations [10–12].

The main components of zeolites are oxygen and silicon atoms, though other elements can partially replace the silicon at the centre of the tetrahedra. This substitution enhances either the structure stability or the chemical properties of the zeolite for a specific application. Aluminium is the most common substituent in zeolites (see **Figure 1-3a** and **b**), with Si/Al ratios that can be as low as 1 [13]. The oxygen and silicon atoms have a formal charge of 2- and 4+ respectively, thus once aluminium or any other element with formal charge 3+ replaces the silicon, a negative charge is created within the structure. Together with the pore system of zeolites, the presence of this negative charge provides remarkable opportunities to use zeolites as solid acids, ion-exchange matrices and redox catalysts. For example, zeolites behave as Brønsted acids if a proton H^{1+} is the counter-ion (see **Figure 1-3c**). Alternatively, aluminium-substituted zeolites show Lewis acidity and redox properties if a metal cation is chosen instead to balance the electric charge (see **Figure 1-3d** and **e**) [14,15].

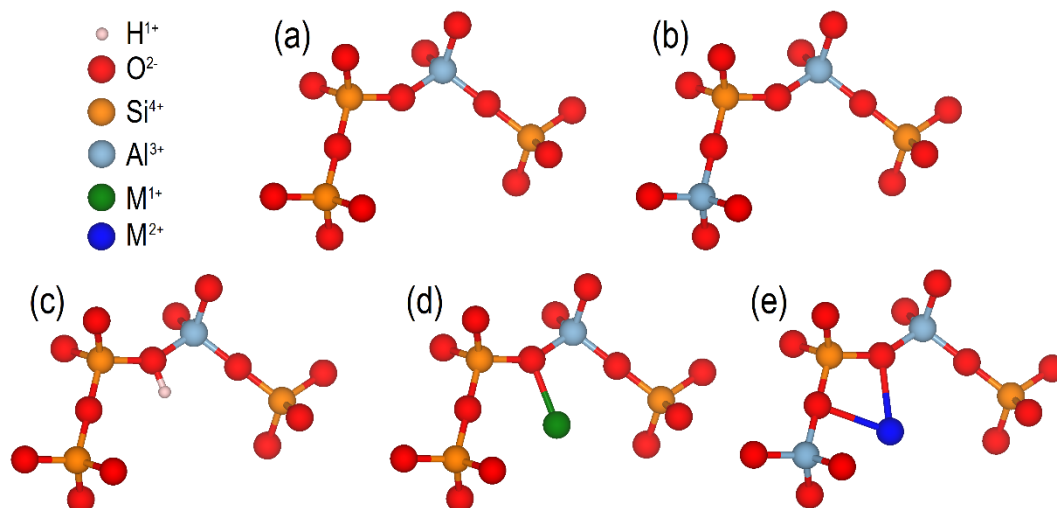


Figure 1-3. Representation of the substitution of silicon by aluminium atoms in (a) one and (b) two T-sites of a zeolite. Counter-ions that balance the spare negative charge after the substitution: (c) proton, (d) metal cation M^{1+} and (e) metal cation M^{2+} .

Aluminium is not the only element that replaces silicon in zeolites. For instance, it has been reported the substitution of silicon by B, Ga, In, Sc, Fe, Zr, Ti, Ge and Sn [16–24]. The substitution of silicon by other 4+ charged atom directly provides Lewis acid character to the zeolite without the need of extra-framework cations. For example, it has been reported that the Lewis acid sites of tin-substituted zeolites catalyse the isomerization of cellulosic sugars [24,25].

The proportion of T^{3+} elements occupying framework positions in relation to the total amount of silicon can be controlled by the type of SDA. For example, high-silica zeolites are obtained when an organic SDA is used, as opposed to an inorganic SDA, which generates structures with low Si/T^{3+} ratios [26,27]. However, the use of seeds in the synthesis process is known to favour high-silica zeolites even in the presence of inorganic SDAs [9].

1.1.4 Micropore System of Zeolites

The notable applications of zeolites as molecular sieves, adsorbents and catalysts are based on their micropore systems [28,29]. The micropores of each type of framework are characterized by their diameter, shape and channel dimensions.

The minimum number of interlinked T-sites that surround the pore provides an indication of the micropore diameter. The micropore is referred then as an n -membered ring (n MR), where n is the number of T-sites forming the pore. The most frequent diameters are 8MR, 10MR and 12MR as shown in **Figure 1-4**. The diameter of the pores represented in **Figure 1-4**, measured as the distance between the oxygen atoms diametrically opposed, are 7.00, 9.23 and 10.21 Å for 8MR, 10MR and 12MR, respectively. However, these values can change from one framework to another depending on structural distortions. Other less common pore diameters are 7MR (MEI), 9MR (CHI), 11MR (JSR), 14MR (AET), 15MR (IRY), 16MR (IFO), 18MR (ETR), 20MR (CLO) and 21MR (EWT). The micropore can also be straight, as shown in **Figure 1-4d**, or sinusoidal as observed in zeolites of lower symmetry.

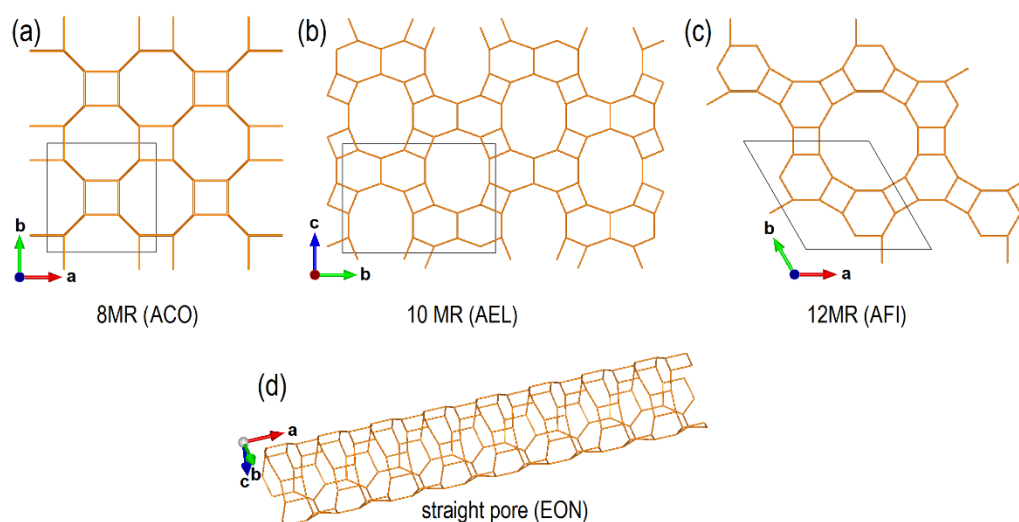


Figure 1-4. Representation of the most frequent zeolite pore diameters: (a) 8MR, (b) 10MR and (c) 12MR. (d) Representation of the straight pore of the EON type.

The pore system of zeolites is also characterized by the number of Cartesian directions or dimensions that a molecule can span within the channels. For instance, a molecule may be only able to diffuse along a pore, unable to move to another pore at an intersection. In this case, the pore system of the zeolite is defined as one-dimensional (see **Figure 1-5a**). Some examples of framework types with one-dimensional channels are AWW and ABW. The next level in this classification comprises in the two-dimensional pore system. Here, the molecule can move in the two-dimensional plane formed by a network of inter-linked pores as represented in **Figure 1-5b**. The UEI and ZON framework types are examples of zeolites with two-dimensional channels. Finally, in the three-dimensional pore system a molecule can cover the entire volume of the crystal by moving through the pores, as shown in **Figure 1-5c**. The MFI and LTA framework types, which have been extensively studied in the present thesis, contain three-dimensional channels.

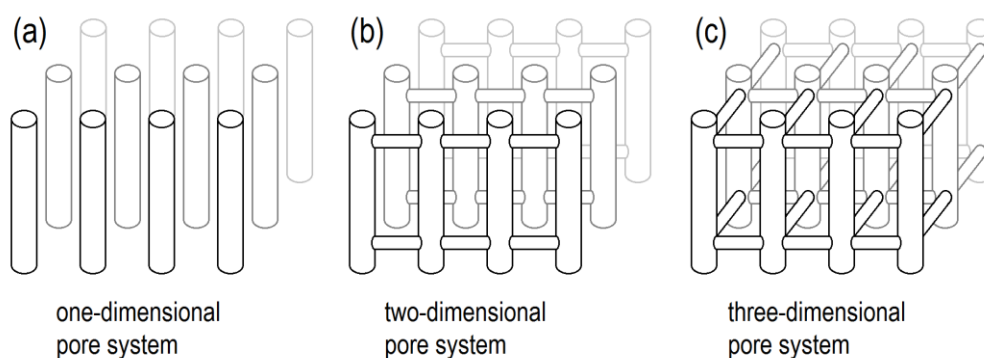


Figure 1-5. Schematic representation of (a) one-dimensional, (b) two-dimensional and (c) three-dimensional zeolite pore systems.

1.1.5 Applications

Zeolites are widely recognised for their extraordinary properties as solid acids [30–32], size-selective molecular sieves [28,33], and ion-exchange matrices [34–36]. Thus, these materials have important practical applications, ranging from water

treatment [37] and membranes for gas permeation [38] to fuel and solar cell materials [39,40]. Specifically, zeolites find their largest relevance as acid-base catalysts, being used for more than 40% of the catalysed industrial processes [41], with the environmental and petrochemical sectors among the main users [29].

1.2 Zeolite MFI

Zeolite Socony Mobil five or ZSM-5 (MFI framework type) is a synthetic zeolite firstly reported by Flanigen and collaborators, which was classified as “hydrophobic and organophilic” that “selectively adsorbs organic molecules over water” [42]. These authors observed that ZSM-5 can adsorb and remove small organic compounds, such as methanol, phenol and hexane, from water. They also remarked the higher thermal stability of this new material compared to carbon-based adsorbents, and larger resistance against acid and oxidative regeneration [42]. The applications of zeolite ZSM-5 have expanded beyond water purification to become one of the most used zeolites in the industry, fundamentally in the petrochemical sector, where its acid properties are very efficient to catalyse alkylation, isomerization, amination, hydrocracking, aromatization and disproportionation processes [41,43]. In addition, if the counter-ion is a transition metal instead of a proton, zeolite ZSM-5 can be used as a catalyst for redox reactions, such as the nitrous oxide decomposition, or as a support of metal nanoparticles with photochemical properties [35,44].

The pure-silica zeolite MFI ($\text{Si/Al} = \infty$) exhibits a monoclinic symmetry ($P2_1/n$) at temperatures below the range 317-325 K. However, at higher temperatures, the material experiences a phase transition, which increases the symmetry of the

structure from monoclinic to orthorhombic ($Pnma$). The increase of the aluminium content within the framework decreases the temperature of the phase transition [45].

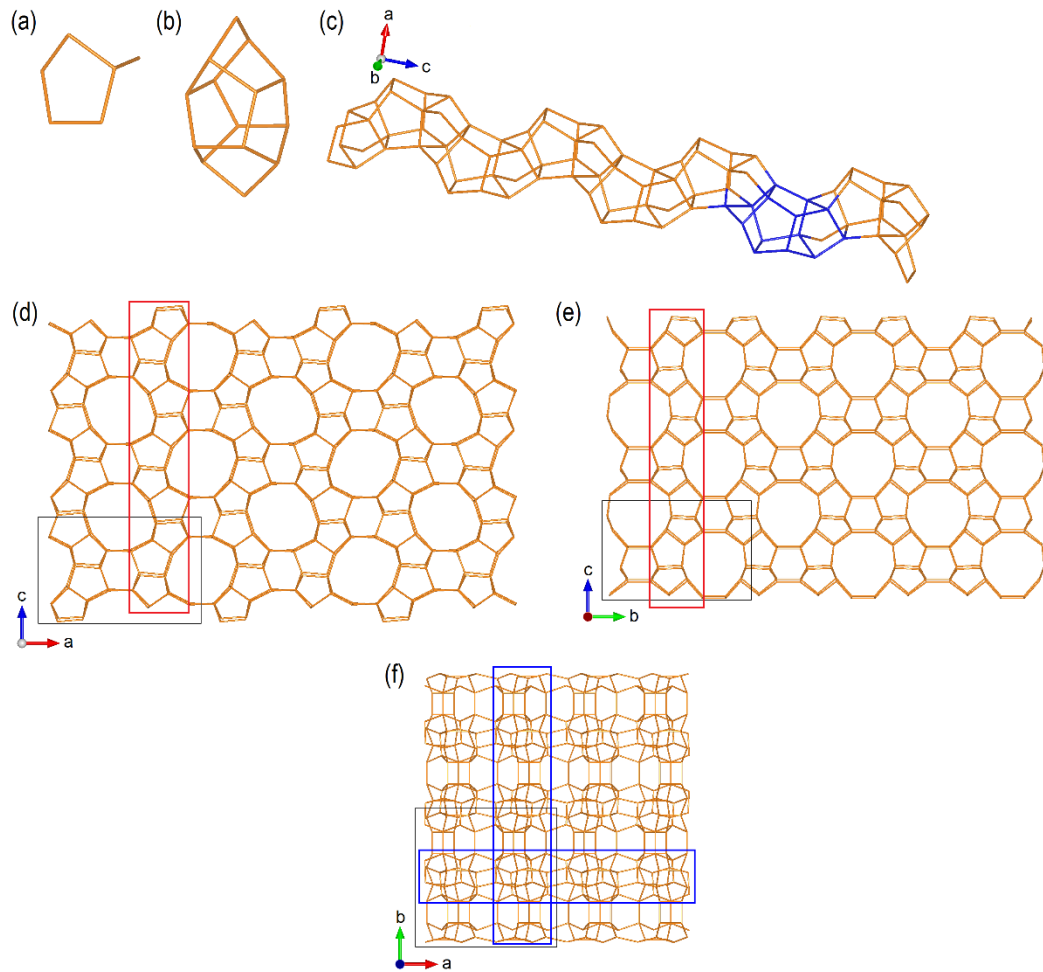


Figure 1-6. (a) SBU of the MFI framework, labelled 5-1. (b) Pentasil unit. (c) Chain of pentasil units along the c direction, a single pentasil unit is highlighted in blue. (d) Pentasil layer formed by replication of the chain on the ac plane. (e) Pentasil layer formed by replication of the chain on the bc plane. The pentasil chain is enclosed by red boxes. (f) Representation of the MFI framework on the ab plane, the ac and bc pentasil layers are enclosed by blue boxes.

The unit cell of zeolite MFI contains 96 T-sites, of which the number of non-equivalent positions are 24 in the monoclinic structure and 12 in the orthorhombic structure. The SBU of the MFI framework consists of 6 T-sites (labelled 5-1), which forms pentasil units (see **Figure 1-6**). These units repeat along the c or [001] direction forming a chain, which is replicated along the a and b directions

assembling two-dimensional pentasil layers that extends over the *ac* and *bc* planes (see **Figure 1-6**). These pentasil layers form periodic building units (PerBU) that, like the SBUs, reproduce the framework by periodic replication as shown in **Figure 1-6f**.

The orthorhombic MFI cell has lattice parameters of approximately 20 Å along *a* and *b*, and 13 Å along *c*. The pore system of this type of zeolite is three-dimensional, composed by straight 10MR channels along *b* and sinusoidal 10MR channels along *a* (see **Figure 1-6**).

1.3 Zeolite LTA

Zeolite Linde Type A (LTA) was originally reported as an aluminosilicate material with formula unit $\text{Na}_{12}[(\text{AlO}_2)_{12}(\text{SiO}_2)_{12}] \cdot 27\text{H}_2\text{O}$ [13,46]. The SBU of LTA is formed from the fusion of a 4MR and a 6MR and contains 8 T-sites (labelled 6-2), as shown in **Figure 1-7a**. The PerBU of LTA comprises three-dimensionally interconnected β -cages (see **Figure 1-7b**) which generates an α -cage at the centre of a cubic unit cell with $Pm\bar{3}m$ symmetry (**Figure 1-7c**). An alternative PerBU to the β -cage consists of double 4-membered rings (D4R, **Figure 1-7d**) [47]. The pore system of LTA is characterized by 8MR apertures connecting α -cages along the three Cartesian directions. The 24 T-sites contained within the unit cell of LTA are equivalent and related by symmetry operations.

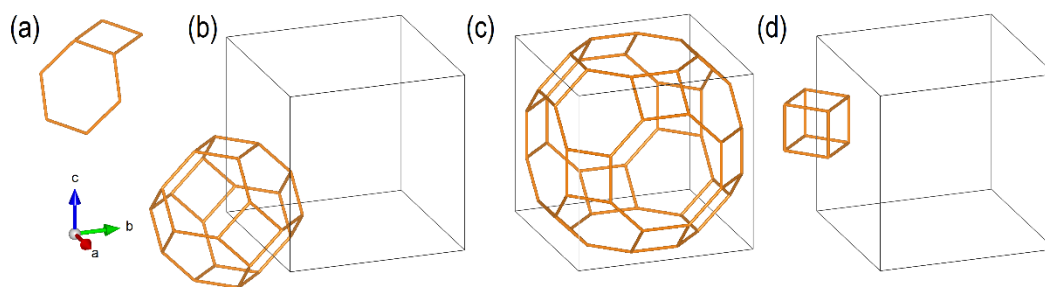


Figure 1-7. Representation of the (a) SBU 6-2, (b) β -cage, (c) α -cage and (d) double 4-membered ring (D4R). The edges of the cubic unit cell are represented by black lines.

The application of LTA as a molecular sieve was identified early on following its synthesis by Beck and collaborators, who reported that the Na^+ ion exchange by other monovalent and divalent cations allowed to tailor the adsorption capacity and selectivity for a wide array of small molecules [13]. The relatively large size of the α -cages of LTA, combined with the small apertures formed by 8MR, lead to attractive applications such as the formation and confinement of metal clusters, which are protected by the zeolite framework against poisoning, thereby allowing their selectivity towards the conversion of small molecules [48].

The LTA framework is also a good candidate for the selective catalytic reduction (SCR) of nitrogen oxides, the methanol-to-olefin (MTO) reaction and the separation of hydrocarbons, where similar zeolites with large cavities connected by small pore apertures have shown attractive results [49–51]. However, the usually low Si/Al ratios of zeolite LTA, in the order of 1 to 3, reduce its hydrothermal stability and acidity, increasing its hydrophilicity and hindering the utilization of LTA in these processes [9]. These drawbacks have been overcome by Corma and collaborators, who synthesized zeolite LTA with Si/Al ratios between 8 and ∞ [52]. These authors used self-assembled organic SDAs to maximize the size-to-charge ratio of the SDA, and made the directing agent bulky enough to fill the α -cages of LTA. As expected,

the high-silica LTA increased significantly its stability and hydrophobicity, improving the ability of this material to separate small organic molecules from water or other polar molecules. In addition, the controlled substitution of a small fraction of silicon by aluminium enhanced the acidic properties of the zeolite, and consequently, its catalytic properties in cracking and MTO reactions [52]. Apart from aluminium, other atoms such as germanium and titanium can replace the silicon in small fractions within the LTA framework [52,53].

1.4 Two-dimensional Zeolites

Zeolites are identified as three-dimensional structures with crystal sizes that can reach several hundreds of microns (μm) [5]. Therefore, the access of the reactants to the active sites and subsequent migration of the products out of the zeolite is controlled by the size and architecture of the micropores. This sieve behaviour, which discriminates molecules by size, forms part of the outstanding features of zeolites as catalysts. However, the limited molecular diffusion throughout the pore system causes the inefficient use of the active sites and the occurrence of undesirable secondary reactions that reduce the lifetime of the catalyst [54]. The synthesis of oriented films of zeolites has been proposed as an alternative to overcome the limitations of bulky zeolite crystals and obtain novel applications, such as selective sensors and electrodes. Initial attempts achieved polycrystalline films of several microns [55].

Corma and collaborators were the first to report the synthesis of a two-dimensional monocrystalline structure of few nanometers [56]. These authors delaminated the precursor of zeolites MCM-22 and ERB-1 (MWW framework type) to obtain two-

dimensional layers with 2.5 nm of thickness, which were designated as ITQ-2. The ITQ-2 sheets were found to maintain the crystalline structure of the conventional zeolite and its catalytic activity, with the additional advantages of reduced formation of coke and a more efficient utilization and accessibility of the active sites [56].

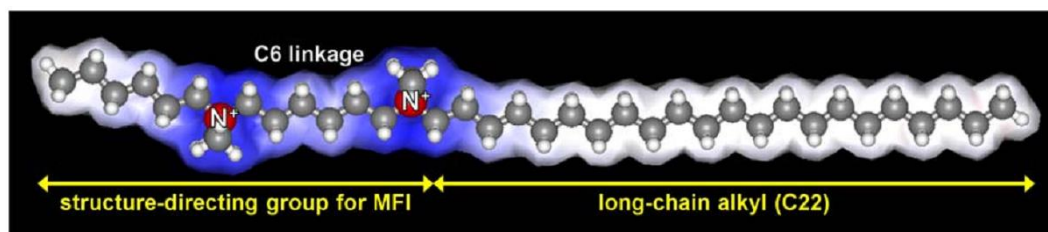


Figure 1-8. Di-quaternary ammonium surfactant used as bifunctional SDA to synthesize MFI nanosheets (adapted from Ref [54] with permission from Nature Publishing Group).

Choi and co-workers also provided a new type of bifunctional organic SDA to directly synthesize two-dimensional nanosheets of zeolite MFI. These authors used di-quaternary ammonium surfactants, as shown in **Figure 1-8**, to direct the formation of zeolite MFI in between the two ammonium groups, whilst the long alkyl chain avoided the growth of the crystalline structure along the normal direction to the nanosheet surface. The result was the direct synthesis of MFI nanosheets, which are schematically represented in **Figure 1-9** [54].

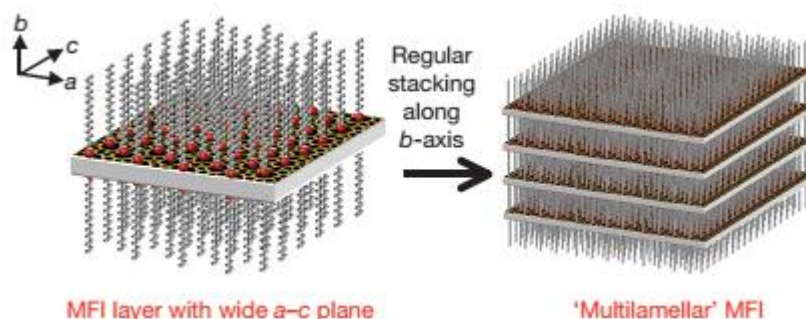


Figure 1-9. Representation of the MFI nanosheet as well as the bifunctional SDA (adapted from Ref [54] with permission from Nature Publishing Group).

The MFI nanosheet, which has been extensively studied in this thesis, preserves the crystalline structure and the micropore system of three-dimensional zeolite MFI throughout the *ac* plane, and can reach a minimum thickness of a single unit cell long the *b* direction [57]. These two-dimensional nanosheets improve the accessibility to the active sites, and consequently can be used to treat bulkier molecules with much more limited diffusion rates through the channels of conventional zeolites [58,59]. It has also been observed that MFI nanosheets have much longer lifetimes as catalysts than conventional zeolites owing to the reduction of secondary reactions and coke formation [54].

Attempts to systematically classify two-dimensional zeolites have placed the number of layered forms at 15, which are defined depending on the synthesis route and final topology [60]. Until this date, 13 framework types are known to have layered or two-dimensional forms, among them MFI and MWW [61].

1.5 Role of Zeolites in the Conversion of Lignin

Lignin is one of the main components of biomass, representing 20 to 30% of its composition [62]. This makes lignin highly abundant and very suitable as a renewable source of chemicals and fuels. However, the polymeric structure of lignin consists of interlinked phenolic monomers, with high oxygen content (see **Figure 1-10**), which requires appropriate catalysts to ensure selectivity and high yields during its processing [62–64].

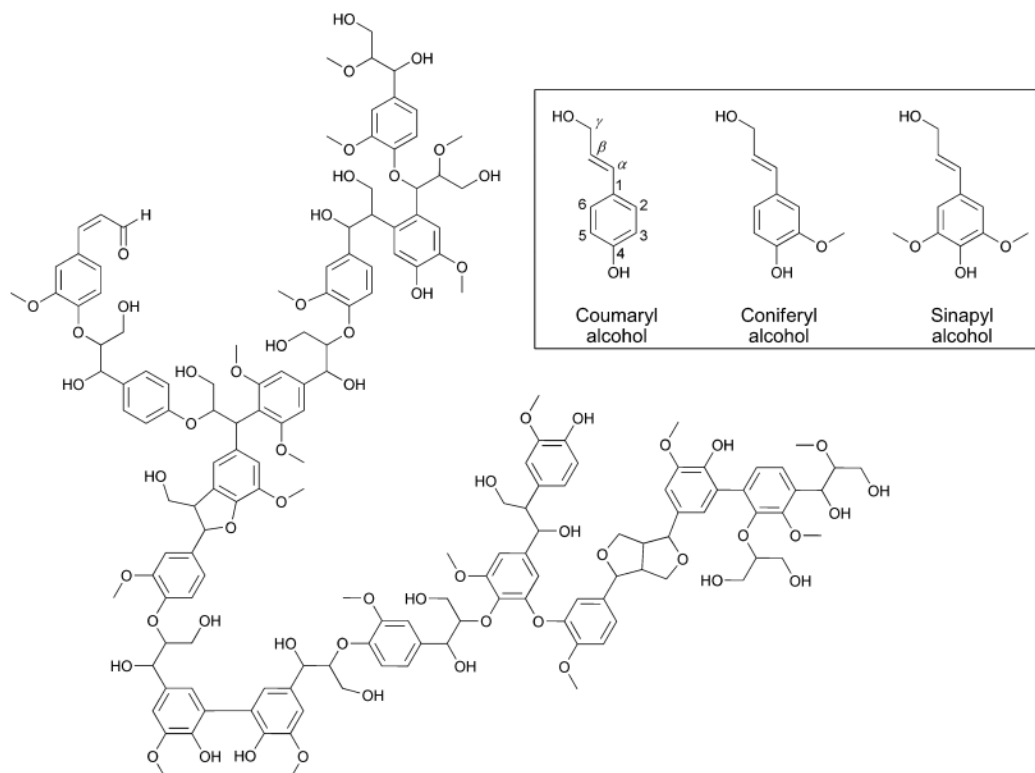


Figure 1-10. Representation of the polymeric structure of lignin and its structural building blocks: coumaryl, coniferyl and sinapyl alcohols (adapted from Ref [62] with permission from The Royal Society of Chemistry).

In the case of fuel-oriented utilization, it is desirable to increase the H:C and C:O ratios of the lignin-derived products in order to improve the efficiency of the combustion [62]. Several experimental methods have been designed to depolymerize, deoxygenate and hydrogenate lignin in the presence of zeolites. For instance, the catalytic fast pyrolysis (CFP) has been employed in presence of zeolites to decrease the oxygen content of organosolv lignin extracted from different sources (organosolv lignin refers to lignin that has been extracted from natural sources using organic solvents). However, this method generates a large number of different by-products without apparent selectivity, and has the drawback of generating solid residues that decrease the lifetime of the catalyst [65–68]. Alternatively, the hydrodeoxygenation (HDO) of organosolv lignin and lignin-derived compounds,

using bifunctional catalysts based on transition metal nanoparticles deposited on acid supports, outperforms the CFP method in selectivity, yields and reduction of solid by-products [69–72].

The bifunctional catalysts use transition metal nanoparticles, which promote the hydrogenation, supported on solid acids that mediate the dehydration and alkylation of the hydrogenated products [69,73–75]. For instance, it has been reported the use of Pt supported on zeolite HY (Pt/HY) [69], a combination of Pd/C and zeolite HZSM-5 [70] as well as Ru/HZSM-5 [71], and Ni/HZSM-5 and Ni/HBEA [72], to mention just few examples. A mixture of monocyclic and bicyclic alkanes are obtained with these methods, highlighting the synergy between the metallic component for hydrogenation and the acid support for dehydration.

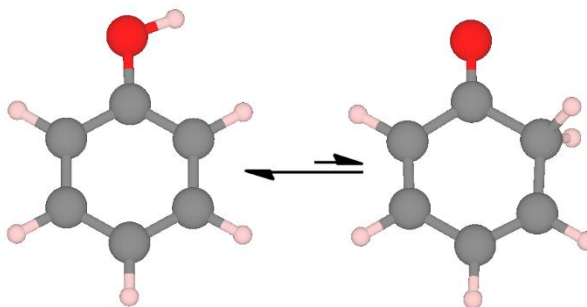


Figure 1-11. Representation of phenol tautomerization.

The HDO of phenolic monomers, such as phenol and cresol, have been the subject of extensive research, both experimental and theoretical, because they are good examples of the major recalcitrant species derived from the upgrading of lignin [76–80]. The type of modifications undergone by the phenolic species depend on the metal or support that is used. For example, 3-methyl-cyclohexanone is the main product obtained from the processing of m-cresol on Ni/SiO₂ or Pt/SiO₂, while toluene is produced with the highest selectivity when the conversion takes place on

Fe/SiO₂ or Pt/ZrO₂. This outcome has been explained by the presence of keto-enol tautomerism (represented in **Figure 1-11**) that transforms m-cresol into 3-methyl-3,5-cyclohexadienone. The cyclohexadienone may follow two different pathways: (i) hydrogenation of the C=C bonds, producing 3-methyl-cyclohexanone, or (ii) the hydrogenation of the C=O group followed by dehydration, generating toluene [78,79]. However, recent DFT calculations have shown that the most probable pathway to obtain toluene consists on the direct deoxygenation of m-cresol, promoted by the oxophilicity of metal surfaces, such as Ru(0001) [80]. Nevertheless, taking into account that the support is also able to influence the selectivity of the hydroprocessing, even when a no oxophilic metal is used [78,81], the keto-enol tautomerism is still a strong alternative to explain the product selectivity of the hydroprocessing. Following this idea, special attention has been given in the present thesis to the possible tautomerization of phenol and catechol on the external surface of MFI zeolite.

1.6 Objectives of the Thesis

This thesis is aimed at the study of the structural, physical and chemical features of MFI and LTA frameworks, focussing on the potential catalytic applications of these materials. In the case of MFI, the main goal is the analysis of its two-dimensional morphology. The simulated MFI nanosheets have been compared to the conventional three-dimensional zeolite regarding aluminium substitution, strength of the acid sites and catalytic utilization. Concerning zeolite LTA, this thesis presents a comprehensive study of its pure-silica and titanium substituted forms, analysing mechanical properties, vibrational spectra and water adsorption.

The results and discussion are divided into four chapters (from Chapter 3 to 6), which cover every aspect of the goals pursued in this thesis. Chapter 3 describes the structure of two- and three-pentasil MFI nanosheets using the slab model. The aluminium substitution at each non-equivalent T-site has been considered, forming a Brønsted acid site by counterbalancing the negative charges with protons. The structural parameters, aluminium substitution energies and vibrational frequencies of the MFI nanosheets and bulk have been compared. In addition, Chapter 3 presents the reaction pathways for the dehydration of aluminium substituted silanols with the subsequent formation of three-coordinated Lewis acid sites.

Chapter 4 delivers an exhaustive analysis of the strength of Brønsted acids located at the internal and external surfaces. The results presented in this chapter have allowed to propose an explanation to the presence of three different acidic strengths in zeolite MFI when it is probed with trimethylphosphine oxide and ^{31}P nuclear magnetic resonance (NMR). Furthermore, it has been discussed the differences and similarities between the behaviour of internal and external acid sites under different degrees of molecular agglomeration.

Chapter 5 uses the results of Chapter 3, i.e. that aluminium-substituted silanols located at the external surface of zeolite MFI dehydrate to form Lewis acids, to study the tautomerization of phenol and catechol catalysed by one of those Lewis sites. This chapter is aimed at understanding the possible role of zeolite MFI, acting as a support of metal nanoparticles, in the hydroprocessing of lignin-derived compounds.

Chapter 6 covers the simulations of zeolite LTA. Here, the mechanical and vibrational features of the pure-silica form are analysed and compared to the titanium-substituted structure. In addition, the distribution of titanium atoms in the

framework has been examined. The last section of the chapter is dedicated to study the water adsorption and its direct dissociation on the titanium-centred tetrahedra.

Chapter 2 Theoretical Methods

This chapter provides a summary of the theoretical methods that have been used to perform the calculations presented in this thesis. Most of the calculations have dealt explicitly with the electronic structure of the systems within the framework of the density functional theory (DFT), though classic interatomic potential (IP) simulations were occasionally used to complement the DFT results when the size and/or number of the calculations were too computationally expensive. The DFT calculations were carried out using the code **Vienna Ab-initio Simulation Package (VASP)** [82–85], and the classic IP simulations using the codes **Minimum Energy Technique Applied to Dislocations, Interfaces and Surfaces Energies (METADISE)** [86] and the **General Utility Lattice Program (GULP)** [87,88].

The DFT-related methods are explained from section 2.1 to section 2.7, and the IP-related methods are treated in section 2.8.

2.1 The Monoelectronic Approximation

The **time-independent Schrödinger** equation describes stationary systems, where quantum effects such as the particle-wave duality cannot be ignored [89]. Applied to the description of matter, this equation uses a *Hamiltonian* operator \hat{H} , which determines the simultaneous repulsions and attractions among nuclei and electrons, to extract the energy corresponding to the *wavefunction* Ψ_0 . The wavefunction Ψ_0 contains all physical information related to the system, and the product $\Psi_0^*\Psi_0$ provides the probability of finding the particles described by Ψ_0 in a given position (atomic units are used):

$$\hat{H}\Psi_0 = E_0\Psi_0 \quad (2-1a)$$

$$\hat{H} = -\frac{1}{2}\sum_a \nabla_a^2 - \frac{1}{2}\sum_A \frac{\nabla_A^2}{M_A} - \sum_a \sum_A \frac{Z_A}{r_{aA}} + \frac{1}{2}\sum_a \sum_b \frac{1}{r_{ab}} + \frac{1}{2}\sum_A \sum_B \frac{Z_A Z_B}{R_{AB}} \quad (2-1b)$$

where ∇^2 is the Laplacian operator, M_A is the mass of the nuclei, Z_A is the charge of the nuclei, and r_{aA} and R_{AB} are the electron-nucleus and nucleus-nucleus distances, respectively. The first two terms of (2-1b) correspond to the kinetic energy of electrons and nuclei, respectively; the third term represents the electron-nucleus attraction interactions; and the fourth and fifth terms describe the electron-electron and nucleus-nucleus repulsion interactions, respectively. The **Born-Oppenheimer approximation** simplifies the problem by considering the nuclei fixed, which makes their kinetic energy nil, while the electrons reach their state of minimum energy for a given atomic configuration [90]. It is then only necessary to focus on the quantum behaviour of the electrons moving under the influence of the external field created by the nuclei, adding later the contribution of the nucleus-nucleus repulsions as a classical correction. To this end, the electronic Hamiltonian \hat{H} can be expressed as:

$$\hat{H} = -\frac{1}{2}\sum_a \nabla_a^2 - \sum_a \sum_A \frac{Z_A}{r_{aA}} + \frac{1}{2}\sum_a \sum_b \frac{1}{r_{ab}} \quad (2-1c)$$

The direct solution of the differential equation (2-1a), which provides the exact form of Ψ_0 , is only possible for few simple cases, and thus practical calculations need to approximate Ψ_0 in order to solve this problem. On this point, the **Hartree-Fock approximation** uses a single *Slater determinant* formed by the spin orbitals $\{\chi_a\}$ to represent Ψ_0 , which guarantees the antisymmetry of Ψ_0 with respect to the

interchange of any two electrons as required by the Pauli principle [91]. In the Hartree-Fock method, the expected value of E_0 , calculated from $\int \Psi_0^* \hat{H} \Psi_0$, has the form:

$$E_0 = \sum_a^N H_a + \frac{1}{2} \sum_a^N \sum_b^N (J_{ab} - K_{ab}) \quad (2-2a)$$

where the terms of (2-2a) are expressed as:

$$H_a = \int d\mathbf{x}_1 \chi_a^*(1) \hat{h}(1) \chi_a(1) \quad (2-2b)$$

$$\hat{h}(1) = -\frac{1}{2} \nabla^2 - \sum_A \frac{Z_A}{r_{1A}} \quad (2-2c)$$

$$J_{ab} = \int d\mathbf{x}_1 d\mathbf{x}_2 \chi_a^*(1) \chi_a(1) r_{12}^{-1} \chi_b^*(2) \chi_b(2) \quad (2-2d)$$

$$K_{ab} = \int d\mathbf{x}_1 d\mathbf{x}_2 \chi_a^*(1) \chi_b(1) r_{12}^{-1} \chi_a^*(2) \chi_b(2) \quad (2-2e)$$

The differential $d\mathbf{x}_1$ considers infinitesimal variations of spin and position of electron 1, and r_{12} is the distance between electron 1 and 2. The integral J_{ab} represents the contribution of the Coulomb interactions to the total energy of the system. The integral K_{ab} does not have a classical interpretation, and its origin is given by the antisymmetry of the wavefunction; K_{ab} is known as exchange integral.

The expression (2-2a) is minimized with respect to the set of orthonormal spin orbitals $\{\chi_a\}$. The stationary point of E_0 , subject to the orthonormality constraint

$\int d\mathbf{r}_1 \chi_a^*(1) \chi_b(1) = \delta_{ab}$, is found by using the Lagrange's method of undetermined multipliers [92], giving the following solution:

$$[\hat{h}(1) + v^{HF}(1)]\chi_a(1) = \varepsilon_a \chi_a(1) \quad (2-3a)$$

where \hat{h} is given by (2-2c), and v^{HF} by:

$$v^{HF}(1) = \sum_b^N \int d\mathbf{x}_2 \chi_b^*(2) r_{12}^{-1} (1 - \hat{P}_{12}) \chi_b(2) \quad (2-3b)$$

$$\hat{P}_{12}(\chi_b(2)\chi_a(1)) = \chi_a(2)\chi_b(1) \quad (2-3c)$$

The potential v^{HF} contains the contributions from the Coulomb interactions and exchange in a single integral by using the operator \hat{P}_{12} , which interchanges electron 1 and 2 between the spin orbitals χ_a and χ_b . The expression within square brackets at the left of (2-3a) is known as Fock operator \hat{f} , which acts on the monoelectronic spin orbitals $\{\chi_a\}$ to give the set of Lagrange's multipliers $\{\varepsilon_a\}$ that represents the energy of the monoelectronic states. To this end, the Hartree-Fock approximation transforms the many-electron problem into a system constituted by non-interacting electrons under the influence of the mean field v^{HF} . The form of v^{HF} explicitly includes the spin orbitals $\{\chi_a\}$, which are the variational quantities during the minimization of the energy. Therefore, an iterative procedure is needed in order to find the solution of the monoelectronic Schrödinger equations (2-3a). An initial set $\{\chi_a\}$ is used to build the operator \hat{f} , which is then used to obtain a new, improved set of spin orbitals $\{\chi'_a\}$. This process is repeated until self-consistency, i.e. until a pre-fixed convergence criteria is reached by the quantities under analysis.

Afterwards, the total energy of the electronic system is calculated according to the equation:

$$E_0 = \sum_a^N \varepsilon_a - \frac{1}{2} \sum_a^N \sum_b^N (J_{ab} - K_{ab}) \quad (2-4)$$

The mere sum of all monoelectronic energies is not enough to compute the total energy of the system. The utilization of the mean field v^{HF} provokes the double counting of the electron-electron interactions, and thus half of them needs to be subtracted from the sum $\sum_a^N \varepsilon_a$.

2.2 Density Functional Theory

The density functional theory (DFT) is nowadays one of the most used theoretical approximations that explicitly deal with the electronic structure of matter at the quantum level. The DFT is very versatile, allowing to study both molecules in the gas phase and solid materials, with an accuracy high enough considering its favourable size-scaling. The practical implementation of DFT shows resemblances to the formulation of the Hartree-Fock approximation regarding the construction of the operators and the protocol of the self-consistent calculations. However, DFT is based on the electronic density, not the wavefunction, to determine the ground state of the system and associated properties.

2.2.1 Hohenberg and Kohn's Theorems

The Density as Basic Variable. P. Hohenberg and W. Kohn demonstrated in their seminal work that, for a system composed by an arbitrary number of electrons

subject to the effect of the external potential $v(\mathbf{r})$ and Coulomb interaction, the electronic density $\rho_0(\mathbf{r})$ in the non-degenerate ground state uniquely determines $v(\mathbf{r})$, except for a trivial additive constant [93]. Altogether, because the external potential $v(\mathbf{r})$ fixes the Hamiltonian, the wavefunction Ψ_0 of the ground state, its energy E_0 and associated properties are also uniquely determined by the electronic density. It is thus defined that the energy of the ground state is a functional of its electronic density, $E_0 = E_0[\rho_0(\mathbf{r})]$.

The Variational Principle. P. Hohenberg and W. Kohn also defined the energy functional:

$$E[\rho(\mathbf{r})] = \int v(\mathbf{r})\rho(\mathbf{r}) + F[\rho(\mathbf{r})] \quad (2-5)$$

where $F[\rho(\mathbf{r})]$ is an universal functional. The authors demonstrated that the correct electronic density $\rho_0(\mathbf{r})$ minimizes the ground state energy. Hence, the solution would be rather simple, involving only the direct minimization of $E[\rho(\mathbf{r})]$ with respect to the variation of the three-dimensional function $\rho(\mathbf{r})$. However, since the form of $F[\rho(\mathbf{r})]$ is unknown, the problem becomes much more complex.

2.2.2 Kohn-Sham Method

W. Kohn and L. J. Sham provided the practical implementation of the Hohenberg and Kohn's theorems following a formalism resembling the Hartree-Fock approximation [94]. These authors proceeded from the ground state energy of an inhomogeneous gas under the influence of a static potential $v(\mathbf{r})$ [93]:

$$E = \int d\mathbf{r}_1 \rho(\mathbf{r}_1) v(\mathbf{r}_1) + \frac{1}{2} \int d\mathbf{r}_1 d\mathbf{r}_2 \rho(\mathbf{r}_1) \mathbf{r}_{12}^{-1} \rho(\mathbf{r}_2) + T_s[\rho] + E_{xc}[\rho] \quad (2-6)$$

where E is a minimum for the correct $\rho_0(\mathbf{r})$. The functional $T_s[\rho]$ is the kinetic energy of a set of non-interacting electrons, and $E_{xc}[\rho]$ is the exchange and correlation energy determined by the density $\rho(\mathbf{r})$. Thereafter, the Lagrange's method was used to find the stationary point of E in function of $\rho(\mathbf{r})$ by using a procedure analogous to the Hartree-Fock approximation:

$$[\hat{h}(\mathbf{r}_1) + v^{KS}(\mathbf{r}_1)]\theta_a^{KS}(\mathbf{r}_1) = \varepsilon_a \theta_a^{KS}(\mathbf{r}_1) \quad (2-7a)$$

$$v^{HF}(\mathbf{r}_1) = v(\mathbf{r}_1) - \frac{1}{2} \nabla^2 + \int d\mathbf{r}_2 \mathbf{r}_{12}^{-1} \rho(\mathbf{r}_2) + \frac{\partial E_{xc}[\rho]}{\partial \rho(\mathbf{r})} \quad (2-7b)$$

$$v(\mathbf{r}_1) = - \sum_A \frac{Z_A}{r_{1A}} \quad (2-7c)$$

The minimization starts with an approximate guess for $\rho(\mathbf{r})$, for instance the superposition of the atomic electron densities, to build the operators in the set of equations (2-7), which are solved to obtain the first estimate of the Kohn-Sham orbitals $\{\theta_a^{KS}\}$. These orbitals are then used to improve the electron density by $\rho(\mathbf{r}) = \sum_{a=1}^N |\theta_a^{KS}|^2$. The cycle is repeated until the variation of the Kohn-Sham orbitals, the electronic density or the total energy of the system is lower than a fixed threshold. The energy of the system is calculated then as:

$$E_0 = \sum_a^N \varepsilon_a - \frac{1}{2} \int d\mathbf{r}_1 d\mathbf{r}_2 \rho_0(\mathbf{r}_1) \mathbf{r}_{12}^{-1} \rho_0(\mathbf{r}_2) + E_{xc}[\rho_0] - \int d\mathbf{r}_1 \rho_0(\mathbf{r}_1) \left. \frac{\partial E_{xc}[\rho]}{\partial \rho(\mathbf{r})} \right|_{\rho=\rho_0} \quad (2-8)$$

The Hohenberg and Kohn's theorems state that only $\rho_0(\mathbf{r})$ is needed in order to describe the ground state of the system, which in principle would skip the utilization of any representation of the wavefunction during the search for the minimum of E . Nevertheless, the Kohn-Sham method proposes to use a set of mono-electronic orbitals $\{\theta_a^{KS}\}$ to describe a system of non-interacting electrons under the influence of the potential $v^{KS}(\mathbf{r})$. The ground state of this fictitious system would have the same $\rho_0(\mathbf{r})$ as the real system where the electron-electron interaction is fully incorporated.

Assuming that the exact form of $E_{xc}[\rho]$ is known, the full spectrum of electron-electron interactions would be included in the description of the system. This would represent an important improvement with respect to the Hartree-Fock approximation, where the correlation effects are completely missed. However, the form of $E_{xc}[\rho]$ is unknown, which carries the main burden in the elaboration of the practical implementation of DFT. The representation of $E_{xc}[\rho]$ is given by different expressions of variable complexity that will be discussed below. For example, if the system is assumed to have a slowly varying density, the exchange and correlation energy per electron in a uniform electron gas, ϵ_{xc} , can be used to approximate $E_{xc}[\rho]$ [93,94]:

$$E_{xc}[\rho] = \int d\mathbf{r} \rho(\mathbf{r}) \epsilon_{xc} \quad (2-9)$$

The homogeneous electron gas is the only system that provides an exact expression for ϵ_{xc} . The expression (2-9) is known as the **local density approximation (LDA)**, which can be generalized in order to consider different spatial Kohn-Sham orbitals to describe electrons with different spin, i.e. dissociation reactions and open-shell

systems. In this case, the approximation receives the name **local spin density approximation (LSDA)** and the functional E_{xc} is determined by the spin densities ρ^α and ρ^β [95]. This local approximation, although very simple, shows remarkable accuracy to describe the structural properties of solids, which is attributed to the correct description of the *exchange hole* [96].

2.2.3 The Generalized Gradient Approximation (GGA)

Hohenberg and Kohn proposed the **gradient expansion (GE)** of the exchange and correlation energy E_{xc} incorporating the gradient of the density $\nabla\rho(\mathbf{r})$ within the functional form of E_{xc} [93]. The LDA preserves only the first term of this expansion neglecting those related to $\nabla\rho(\mathbf{r})$. However, initial efforts proved that the inclusion of higher order terms comprising $\nabla\rho(\mathbf{r})$ worsens the predictions made by the LDA [97,98]. Important improvements were made by restoring the correct behaviour of the exchange hole in the GE [96], which provided the basis for the future developments of the generalized gradient approximation (GGA).

The GGA has been established as a standard method for the study of solid materials and molecules owing to the improved description of the energy differences when compared with LDA, i.e. atomization energies, reaction barriers and phase transition in solids. Several approximate expressions have been proposed for the GGA functional, which are mainly divided in two groups: (i) functionals derived semiempirically by fitting analytical expressions to experimental data or high-level *ab-initio* calculations of a set of representative atoms and molecules [99], and (ii) nonempirical functionals created to obey essential properties of the exact exchange-correlation energy [100]. Although the semiempirical GGA functionals show high

accuracy for atoms and molecules, they tend to fail when applied to solids [101]. The GGA proposed by Perdew, Burke and Ernzerhof (PBE) is an example of nonempirical functional, which was designed to preserve the correct characteristics of the LDA while ensuring that the gradient contributions satisfy the correct behaviour under limiting conditions [100].

The Laplacian of the density $\nabla^2\rho(\mathbf{r})$ or the kinetic energy density $\tau(|\nabla\rho|^2)$ can also be included as input variables within the expressions to approximate E_{xc} . This natural extension of the GGA is known as **meta-GGA**. The meta-GGA contains more information related to the electronic density of the system and may potentially be more accurate than the GGA functionals [101].

2.2.4 Calculation of Forces

The Born-Oppenheimer approximation allows to treat separately the electronic system from the nuclei [90], and deal with the latter using the Newton's law of motion. The forces $\{F_A\}$ acting on the nuclei $\{A\}$ are derived by the **Hellmann-Feynman theorem**:

$$F_A = - \int d\mathbf{r} \rho(\mathbf{r}) \frac{\partial v(\mathbf{r})}{\partial R_A} - \frac{\partial E_{NN}}{\partial R_A} \quad (2-10)$$

where $v(\mathbf{r})$ is the external potential acting on the electrons that is created by the nuclei, E_{NN} is the total nucleus-nucleus repulsion energy and $\partial/\partial R_A$ is the partial derivative as a function of the nuclear position R_A . In addition, the basis functions used to describe the orbitals $\{\theta_a^{KS}\}$ in practical calculations may also move and change as a consequence of the variation of the nuclear coordinates, adding extra

terms to (2-10) [102]. This is a common problem of local basis sets, which are centred at the nuclear positions. Alternatively, plane wave basis sets have the important advantage of not being localized at any point of the system, allowing to directly use the expression (2-10) to compute the forces F_A .

2.3 Periodic Systems

The crystalline structure of solid materials is described by a mesh of points regularly distributed throughout space. A specific number of atoms or molecules is associated to each of these basic points, following in this way the periodicity of the mesh. The primitive lattice vectors $\{\mathbf{a}_i\}$ define the translational periodicity of the lattice:

$$\mathbf{T} = n_1 \mathbf{a}_1 + n_2 \mathbf{a}_2 + n_3 \mathbf{a}_3 \quad (2-11)$$

where n_i ($i = 1,2,3$) are integer numbers. The analysis of the crystal properties using Fourier series implies the existence of an equivalent mesh in the reciprocal space [103], which is defined by the primitive lattice vectors $\{\mathbf{b}_i\}$, and is related to the real space lattice by:

$$\mathbf{a}_i \cdot \mathbf{b}_j = 2\pi \delta_{ij} \quad (2-12)$$

The translational periodicity \mathbf{G} of the reciprocal lattice can be written as:

$$\mathbf{G} = m_1 \mathbf{b}_1 + m_2 \mathbf{b}_2 + m_3 \mathbf{b}_3 \quad (2-13)$$

where m_i ($i = 1,2,3$) are integer numbers. The vectors \mathbf{G} and \mathbf{T} satisfy the important expression:

$$e^{\pm i\mathbf{G}\cdot\mathbf{T}} = 1 \quad (2-14)$$

The *Wigner-Seitz primitive cell* is an alternative representation of the crystal periodicity. This cell is built as follows: planes are perpendicularly placed in the middle of the imaginary lines that connect the first-neighbour points of the real-space lattice; the smallest volume enclosed by these planes constitutes the Wigner-Seitz primitive cell, and it can completely fill the rest of the space by periodic replication. The equivalent construction in the reciprocal space is called the *first Brillouin zone*, and it plays a fundamental role in the description of the electronic band structure of solids [103].

2.3.1 Bloch Theorem

The periodic boundary condition model considers the crystalline structure of solids extending infinitely along the three spatial dimensions. This inevitably implies an infinite number of electrons. Fortunately, the Bloch theorem allows to transform this problem into a single-particle formulation dealing with a finite number of electrons [104]. It is then possible to apply available computational methods, such as the Kohn-Sham approximation, to the study of solid materials.

The Bloch theorem proposes a system of non-interacting electrons moving under the influence of a potential $U(\mathbf{r})$ with the periodicity of the real space lattice. This $U(\mathbf{r})$ determines the single electron Hamiltonian of the system:

$$\hat{H} = \frac{\hat{p}^2}{2m} + U(\mathbf{r}) \quad (2-15)$$

where \hat{P} is the momentum operator and m the mass of the electron. Each eigenfunction ψ of \hat{H} is orthogonal to all but one eigenvector of momentum \mathbf{k} , which permits to label ψ with the corresponding vector \mathbf{k} , $\psi_{\mathbf{k}}$ [105]. The standard expressions of the Bloch theorem are [103,105]:

$$\psi_{\mathbf{k}} = e^{i\mathbf{k}\mathbf{r}} u_{\mathbf{k}}(\mathbf{r}) \quad (2-16a)$$

$$\psi_{\mathbf{k}}(\mathbf{r} + \mathbf{T}) = e^{i\mathbf{k}\mathbf{T}} \psi_{\mathbf{k}}(\mathbf{r}) \quad (2-16b)$$

where $u_{\mathbf{k}}(\mathbf{r})$ is a function with the periodicity of the crystal. Therefore, according to Bloch, the eigenfunctions $\{\psi_{\mathbf{k}}\}$ are plane waves, periodically modulated by $u_{\mathbf{k}}(\mathbf{r})$, that treat two different point of the system, separated by a translational operation of symmetry, as exactly the same except for a phase factor $e^{i\mathbf{k}\mathbf{T}}$. Both, $\psi_{\mathbf{k}}(\mathbf{r} + \mathbf{T})$ and $\psi_{\mathbf{k}}(\mathbf{r})$, share the same probability $|\psi_{\mathbf{k}}|^2$, which means that the electron density has the periodicity of the crystal: $\rho(\mathbf{r} + \mathbf{T}) = \rho(\mathbf{r})$. In addition, the Bloch theorem specifies that it is only necessary to consider the set of vectors $\{\mathbf{k}\}_{\text{FBZ}}$ that fills the first Brillouin zone in order to have a complete description of the system. An infinite number of energy levels $\{n\}$ would be then associated to each vector \mathbf{k} , which is transformed into a finite number in practical implementations by considering only energies below a pre-fixed value. The contribution of the vectors $\{\mathbf{k}\}_{\text{FBZ}}$ to a particular energy level n forms an electronic band with a specific dispersion relationship, $E_n = E_n(\mathbf{k})$.

The number of allowed vectors $\{\mathbf{k}\}_{\text{FBZ}}$ is given by the number of primitive cells contained in the total volume of the crystal. Therefore, if the structure of the solid is assumed infinite for practical purposes, an infinite number of vectors $\{\mathbf{k}\}_{\text{FBZ}}$ is expected. However, only a finite number of vectors, regularly distributed over the

entire first Brillouin zone, is enough to describe the system [106–108]. The accuracy of the calculation is given by the density of the mesh. For instance, a relatively low number of \mathbf{k} vectors (or \mathbf{k} points of the mesh) is needed for insulators and semiconductors, while a finer distribution of \mathbf{k} points is required for metals to properly evaluate the fractional occupancy of the electronic bands close to the Fermi energy. The number of \mathbf{k} points for a particular calculation should be explicitly estimated by increasing the density of the mesh until convergence is achieved; a convergence of 1 meV/atom is usually recommended.

In summary, the Bloch theorem allows to describe an infinite crystal by considering only the finite number of electrons contained within a periodic unit cell with the symmetry of the crystal. The electrons are distributed over a finite number of electronic bands given by a reasonable cutoff that avoids to consider empty states above a specific energy. Finally, the infinite reciprocal space is fully sampled by a finite mesh of \mathbf{k} points over the first Brillouin zone.

2.3.2 Plane Wave Basis Set

The periodic function $u_{\mathbf{k}}$ within the Bloch wavefunction $\psi_{\mathbf{k}}$ can be expressed as a Fourier series [103]:

$$u_{\mathbf{k}}(\mathbf{r}) = \sum_{\mathbf{G}} C_{\mathbf{k},\mathbf{G}} e^{i\mathbf{G}\mathbf{r}} \quad (2-17)$$

where \mathbf{G} is the translational periodicity of the reciprocal lattice. It can be shown that (2-17) is periodic under a lattice translation \mathbf{R} by using (2-14). The Bloch wavefunction $\psi_{\mathbf{k}}$ can thus be rewritten as:

$$\psi_{\mathbf{k}}(\mathbf{r}) = \sum_{\mathbf{G}} C_{\mathbf{k},\mathbf{G}} e^{i(\mathbf{k}+\mathbf{G})\mathbf{r}} \quad (2-18)$$

Consequently, the wavefunction $\psi_{\mathbf{k}}$ can be expanded as a sum of plane waves weighted by the coefficients $C_{\mathbf{k},\mathbf{G}}$. The vector \mathbf{k} is within the first Brillouin zone and the sum over the vectors \mathbf{G} goes, in principle, up to infinity. However, the coefficients $C_{\mathbf{k},\mathbf{G}}$ lose significance for higher values of $|\mathbf{G}|$, and thus (2-18) can be transformed into a finite series by choosing a maximum value $|\mathbf{G}_{max}|$. This top limit for (2-18) is usually expressed as the kinetic energy of a plane wave with momentum $\hbar\mathbf{G}_{max}$. The accuracy of the plane wave basis set is straightforwardly improved by increasing the value of the cutoff kinetic energy. Nevertheless, it should be considered that the computational demands grow by increasing the number of basis functions in (2-18).

2.3.3 The Pseudopotential Approximation

A large number of plane waves is necessary to accurately describe the rapid oscillations of the wavefunctions close to the nucleus region, which renders the plane wave basis sets inefficient in all-electron calculations. This drawback is solved by replacing the real wavefunctions ψ with smooth, nodeless pseudo-wavefunctions $\tilde{\psi}$ that can be expanded with an affordable number of plane waves. Also, these pseudo-wavefunctions are only used to explicitly describe the valence electrons moving under the influence of an effective pseudopotential. The pseudopotential substitutes the strong electrostatic potential of the nuclei and its singularity at the nuclear site, and includes the screening of the valence layer by the internal electrons [109,110]. This approximation is based on the assumption that chemical and physical properties

of the system are mainly attributed to the valence electrons while the internal electrons remain unaffected by the chemical environment.

The pseudopotential needs to ensure that the pseudo-wavefunction and the real wavefunction match beyond a chosen radius r_c , which determines the core region ($r < r_c$) where the wavefunction nodes are replaced by the smooth approximation. In addition, the magnitude and first derivative of the pseudo-wavefunction and real wavefunction have to match at the boundary ($r < r_c$). These and other properties are incorporated into the following pseudopotential approximations: (i) the **norm-conserving** pseudopotentials [111], (ii) the **ultra-soft** pseudopotentials [112], and (iii) the **projector augmented-wave** method [113,114].

The norm-conserving approximation is characterized by the requirement that the total pseudo charge density must be equal to the real value inside the core region:

$$\int_0^{r_c} dr \tilde{\psi}^*(r)\tilde{\psi}(r) = \int_0^{r_c} dr \psi^*(r)\psi(r) \quad (2-19)$$

However, the imposition of this condition fails to achieve a notable reduction of the number of plane waves for several important cases such as the $2p$ orbitals of oxygen [112]. The ultra-soft pseudopotentials solve this problem by abandoning the norm-conservation restriction, and adding augmentation functions to account for the deficit of valence charge density within the core region [112]. The ultra-soft approximation allows to use larger r_c , which significantly reduces the size of the plane wave basis set without serious penalties in accuracy. Nevertheless, both the norm-conserving and ultra-soft pseudopotentials need to use non-linear core corrections when there is important exchange interactions between the valence and core electrons [115].

The projector augmented-wave (PAW) method eliminates the drawback related to the overlap between the core and valence electrons. This method uses plane waves to describe the smooth pseudo wavefunction, but restores the nodal features of the real wavefunction and its orthogonality to the core states by making use of all-electron radial solutions of the Schrödinger equation for isolated atoms. These radial solutions are called all-electron partial waves ϕ_i , and are evaluate only once and stored for future use. The equivalent pseudo partial waves $\tilde{\phi}_i$, which construct the pseudo wavefunction $\tilde{\psi}$ within the core region by their linear combination $\tilde{\psi} = \sum c_i \tilde{\phi}_i$, match the all-electron partial waves ϕ_i beyond the radius r_c . The real wavefunctions ψ are constructed then from the pseudo wavefunctions $\tilde{\psi}$ by replacing the smooth approximation within the core, represented by $\tilde{\phi}_i$, with the correct nodal features, represented by ϕ_i :

$$\psi = \tilde{\psi} - \sum c_i \tilde{\phi}_i + \sum c_i \phi_i \quad (2-20)$$

In practical applications, there is no need to directly calculate the real wavefunctions ψ , instead, the operators are transformed to obtain the observable quantities as expectation values of the pseudo wavefunctions [113].

Following this concept, the system is thought to be divided in electrons and ions, instead of electrons and nuclei. Also, when referring to the forces that tend to modify the nuclei coordinates, the terms *ionic force* and *ionic positions* are used.

2.4 Analysis of the Electronic Structure

In DFT calculations, it is always desirable to correlate modifications arising in the electronic structure with variations taking place in the ionic configuration. This could provide the means to explain the variable strength of several chemical processes, such as molecular adsorptions and interatomic bonding, which may help to correctly predict and design future material applications. Here, the essentials of the methods used in this thesis for the analysis of the electronic structure are given.

2.4.1 Density of States

The density of states (DOS) is the number of independent electronic states per unit of energy and volume:

$$D(\varepsilon) = \frac{1}{(2\pi)^d} \int_{BZ} d\mathbf{k} \delta(\varepsilon_{n,\mathbf{k}} - \varepsilon) \quad (2-21)$$

The integration of (2-21) is over the first Brillouin zone, and has been carried out in this thesis by the **modified tetrahedron method** [116] and the **Gaussian broadening method** [117]. The quantity $\varepsilon_{n,\mathbf{k}}$ is the energy corresponding to the band n and reciprocal space vector \mathbf{k} .

The DOS can be projected onto spherical harmonics Y_{lm}^A centered at the position of each ion A . These spherical harmonics are non-zero only within a sphere of radius r_w , which is defined according to the PAW method for each element. The profile of the **projected DOS (PDOS)** provides useful information regarding the interatomic interactions, i.e. the intensity and position of the PDOS peaks coincide for atoms close in space with strong interaction. In addition, the *Fermi energy* determines the

boundary between the electronic bands that are occupied and empty, and thus the PDOS plotting can also give information related to charge transfer. In this case, the transfer is asserted by calculating the profile for different conditions; the variation of the intensity of the peaks below and above the Fermi level expresses how effective the charge transfer is.

2.4.2. Electronic Charge Density

The electronic charge density is obtained from the occupied wavefunctions ψ_{nk} according to the equation:

$$\rho(\mathbf{r}) = \sum_{n, k \in occ} |\psi_{nk}|^2 \quad (2-22)$$

The electronic density of specific bands $\rho_n(\mathbf{r})$ can be plotted and visualized. For example, the highest occupied band and the lowest unoccupied band can be space-resolved in the form of their corresponding charge densities. This visualization would allow to observe which region of the structure donates and which accepts electrons, with the subsequent prediction in reactivity and adsorption.

2.4.3 Bader Charge Analysis

The theory of **atoms in molecules (AIM)**, proposed by Bader and collaborators, allows to assign a portion of the total number of electrons to each ionic centre. This is accomplished by dividing the total volume of the system into atomic volumes separated by zero-flux surfaces of electronic density [118]. In addition, this theory provides the physical basis for the Lewis and valence-shell electron pair repulsion

(VSEPR) methods [119]. Although this partition method is independent of the basis set that is used, the electron delocalization in DFT can introduce errors in the assessment of the ionic charges. Nevertheless, this scheme provides a simple method to evaluate the charge transfer in the system, and obtain useful trends.

2.5 Dispersion Forces Correction

The local and semilocal approximations of the DFT are unable to properly describe the non-local character of dispersion interactions [120]. High-level quantum chemistry calculations certainly account for these interactions [121,122], however, their computational cost is prohibitive for more than few dozen atoms. There are approximations that intent to account for dispersion interactions within the DFT framework, which either directly modify the correlation functional to include non-local contributions [123], or adjust the missing energy by adding a correction term to the standard DFT energy [120,124]. These methods are much less computationally expensive, while allowing to obtain a fair picture of non-local interactions.

In particular, the **Grimme's corrections (DFT+D2 and DFT+D3)** provide a reliable and fast method to account for dispersion interactions. In the first scheme (DFT+D2), the total energy of the systems is specified by [124]:

$$E_{DFT+D2} = E_{DFT} + E_{disp}^{(2)} \quad (2-23)$$

where E_{DFT} is the standard self-consistent energy of Kohn-Sham and $E_{disp}^{(2)}$ is the two-body dispersion correction:

$$E_{disp}^{(2)} = -\frac{s_6}{2} \sum_{i,j=i+1} \frac{C_6^{ij}}{r_{ij}^6} f_{dmp}(r_{ij}) \quad (2-23a)$$

$$f_{dmp}(r_{ij}) = \frac{1}{1 + e^{-d(r_{ij}/R_{vdw}^{ij}-1)}} \quad (2-23b)$$

The parameter s_6 is a global scaling factor that is specific for each DFT functional; the quantity C_6^{ij} is the two-body dispersion coefficient; R_{vdw}^{ij} is the sum of the Van der Waals radii of the atoms i and j , with r_{ij} as their internuclear distance; and $f_{dmp}(r_{ij})$ is a damping function. The function $f_{dmp}(r_{ij})$ avoids singularities for small values of r_{ij} , and minimizes the contribution of (2-23) for r_{ij} within bonding distances. The coefficients C_6^{ij} are obtained from the geometric mean $\sqrt{C_6^i C_6^j}$ for each atomic pair. The quantities C_6^i and R_{vdw}^i in DFT-D2 are independent of the chemical environment, and are tabulated for each atomic element.

The more recent variant of Grimme's method (DFT+D3) includes three-body contributions to the total energy [125]:

$$E_{DFT+D3} = E_{DFT} - E_{disp}^{(2)} - E_{disp}^{(3)} \quad (2-24)$$

Here, the expression for $E_{disp}^{(2)}$ is similar to (2-23a) but with inverse sign and adding the higher order term C_8^{ij}/r_{ij}^8 . The dispersion coefficients C_6^i in DFT-D3 are evaluated for each element *ab-initio*, including geometry information in the form of hydrides with different stoichiometry. The higher order coefficient C_8^i is estimated

from C_6^i using multipole-type expectation values. The expression for $E_{disp}^{(3)}$ is given by:

$$E_{disp}^{(3)} = \sum_{ijk} f_{dmp}^{(3)}(\bar{r}_{ijk}) E^{ijk} \quad (2-25a)$$

$$E^{ijk} = \frac{C_9^{ijk} (3 \cos \theta_i \cos \theta_j \cos \theta_k + 1)}{(r_{ij} r_{jk} r_{ki})^3} \quad (2-25b)$$

$$C_9^{ijk} = -\sqrt{C_6^{ij} C_6^{jk} C_6^{ki}} \quad (2-25c)$$

where $f_{dmp}^{(3)}$ is a damping function that uses the geometrically averaged radii \bar{r}_{ijk} . The quantities $\theta_{i,j,k}$ are the internal angles of the triangle formed by the atoms i , j and k . The coefficient C_9^{ijk} is the triple dipole constant and is evaluated from the two-body coefficients $C_6^{ij,jk,ki}$. The Axilrod–Teller–Muto dispersion term E^{ijk} turns the sign of the $E_{disp}^{(3)}$ contribution, which is positive (repulsive) for systems with many acute triatomic triangles. This repulsive contribution, which is important for densely packed systems, such as solid materials, helps to correct the overbinding of the DFT+D2 method [120].

2.6 Geometry Optimization and Vibrational Analysis

During DFT calculations, it is desirable to obtain the ionic structure corresponding to the global minimum in the potential energy surface or *ground state*. This process is referred to as *geometry optimization*, *minimisation* or *relaxation* of the initial structure given as an input at the beginning of the calculation. According to the Born-

Oppenheimer approximation [90], the electronic system is self-consistently optimized for a specific array of ionic coordinates, and that electronic information is used to move the ionic positions towards a lower configurational energy. This process, consisting in electronic iterations followed by a movement of the ions, is repeated until a minimum in the potential energy surface is found according to a pre-fixed threshold in the ionic forces or the total energy.

2.6.1 Local Minimization Techniques

The **steepest descents (SD)** method is a minimization algorithm that localizes the nearest minimum in the potential energy surface [126]. For an initial ionic configuration \mathbf{R}_0 , the SD uses the gradient at \mathbf{R}_0 :

$$\mathbf{g}_0 = -\left. \frac{\partial E}{\partial \mathbf{R}} \right|_{\mathbf{R}=\mathbf{R}_0} \quad (2-26)$$

to displace the system to the point \mathbf{R}_1 , which corresponds to the configuration with the lowest energy along \mathbf{g}_0 . Once at \mathbf{R}_1 , a new gradient \mathbf{g}_1 is calculated and the process is repeated until the minimum is located, as shown in **Figure 2-1a**. Although the SD method seems the most natural way to search for the minimum, it usually needs a large amount of iterations to converge, which makes this technique computationally expensive.

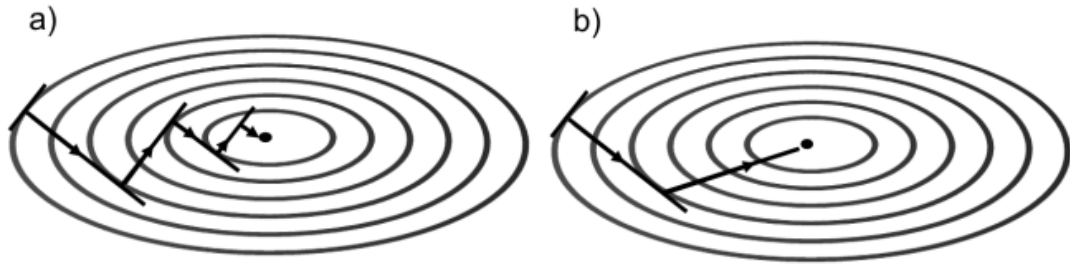


Figure 2-1. Representation of the exploration of the potential energy surface by the (a) steepest descents and (b) conjugated gradients methods.

The **conjugate gradient (CG)** method is based on the SD procedure, but instead of using the gradient \mathbf{g}_n calculated for a given configuration \mathbf{R}_n as a new search direction, the CG includes the information of previous configurations to create a modified path \mathbf{g}'_n to displace the system:

$$\mathbf{g}'_n = \mathbf{g}_n + \gamma_n \mathbf{g}'_{n-1} \quad (2-27a)$$

$$\gamma_n = \frac{\mathbf{g}_n \cdot \mathbf{g}_n}{\mathbf{g}_{n-1} \cdot \mathbf{g}_{n-1}} \quad (2-27b)$$

The search direction \mathbf{g}_0 of the SD and CG methods coincides for the first step of the iteration (see **Figure 2-1**), where the value of γ_0 is zero in (2-27a). The CG method is more efficient than the SD technique to explore the potential energy surface, and locate the nearest minimum to the initial configuration \mathbf{R}_0 . This is the result of following conjugate directions, which are optimally independent from each other, and reduce by one the number of dimensions to explore at each iteration [126]. Consequently, the CG method has been used for all geometry optimization in this thesis.

2.6.2 Molecular Dynamics

Molecular dynamics (MD) allows to analyse the time evolution of the ionic coordinates subject to Newton's equations of motion. The **Verlet algorithm** is a numerical method frequently used in MD to integrate these equations of motion, where the ionic coordinates at $\mathbf{r}(t + \Delta t)$ are calculated from the current (t) and previous ($t - \Delta t$) steps of the simulation [127]:

$$\mathbf{r}(t + \Delta t) = 2\mathbf{r}(t) - \mathbf{r}(t - \Delta t) + a(t)\Delta t^2 \quad (2-28)$$

In (2-28), Δt represents the time step, which should be as long as possible to speed up the calculation, but also short enough to account for the oscillations with the highest frequencies. The instantaneous acceleration $a(t)$ is calculated from the Hellmann-Feynman forces after each electronic self-consistent cycle. The numerical accuracy of the original Verlet algorithm is improved by the velocity-Verlet algorithm [128], which explicitly evaluates the velocities for the step $t + \Delta t$ based on the information of the current step:

$$\mathbf{r}(t + \Delta t) = \mathbf{r}(t) + \mathbf{v}(t)\Delta t + \frac{1}{2}a(t)\Delta t^2 \quad (2-29)$$

$$\mathbf{v}(t + \Delta t) = \mathbf{v}(t) + \frac{1}{2}[a(t) + a(t + \Delta t)]\Delta t \quad (2-29)$$

The temperature is introduced as a statistical quantity proportional to the velocity of the particles. The temperature is a measure of the energy of the system and its capacity to overcome the barriers that separate neighbouring local minima. Therefore, in contrast to the local optimization, the MD does not force the system to converge to the nearest energy minimum, but instead allows the structure to explore

a wider region of the potential energy surface, which may contain several local minima. The Nosé algorithm is a common method to control the fluctuation of the temperature, conserving its average constant along the simulation [129,130].

The physical properties that define the initial conditions of a system are the number of particles (N), the temperature (T), the pressure (P), the volume (V) and the total energy (E). When the MD simulation is initiated, a specific combination of these physical properties is kept constant, defining the type of *ensemble* that controls the evolution of the system. For example, this thesis uses a *canonical ensemble* (NVT) to obtain the statistical data related to the interaction of trimethylphosphine oxide with the Brønsted acid sites of zeolite MFI. This ensemble keeps constant the number of particles, the volume and the temperature of the system.

2.6.3 Vibrational Analysis

The vibrational modes and frequencies of the system are evaluated from the diagonalization of the Hessian matrix:

$$Hessian = \begin{bmatrix} \frac{\partial^2 E}{\partial x_1^2} & \cdots & \frac{\partial^2 E}{\partial x_1 \partial x_n} \\ \vdots & \ddots & \vdots \\ \frac{\partial^2 E}{\partial x_n \partial x_1} & \cdots & \frac{\partial^2 E}{\partial x_n^2} \end{bmatrix} \quad (2-30)$$

where each element of the matrix is the second derivative of the total energy E with respect to displacements of the ions. The second derivatives can be evaluated by **finite differences** or **density functional perturbation theory (DFPT)** [131], within the *harmonic approximation*. The eigenvalues of the Hessian matrix correspond the vibrational frequencies, and the eigenvectors to the vibrational modes of the system.

The calculation of the vibrational properties enables to identify whether the system arrived to a minimum or a saddle point after the geometry optimization. In the case of a local or a global minimum in the potential energy surface, all second derivatives are positives, and consequently all eigenvalues are real. In the case of saddle points, all second derivatives are positives except for the vibrational mode along the reaction coordinate, which corresponds to an imaginary frequency [132]. In addition, the vibrational frequencies can be directly compared to the experiment, which allows to validate the computational model, and to correlate specific structural defects to a given vibrational spectrum.

The vibrational partition function Z_v is calculated using the following equation [133]:

$$Z_v = \prod_{\alpha} \frac{e^{-\theta_{\alpha}/2T}}{1 - e^{-\theta_{\alpha}/T}} \quad (2-31a)$$

$$\theta_{\alpha} = \frac{h\nu_{\alpha}}{k_B} \quad (2-31a)$$

where T is the temperature, ν_{α} is the frequency of the α th eigenmode, h is the Planck constant and k_B is the Boltzmann constant. The partition function Z_v is used to calculate the contributions of the thermal energy E_v and the entropy S_v resulting from the vibration of the structure:

$$E_v = k_B T^2 \left(\frac{\partial \ln Z_v}{\partial T} \right)_v \quad (2-32a)$$

$$S_v = k_B \left[\ln Z_v + T \left(\frac{\partial \ln Z_v}{\partial T} \right)_v \right] \quad (2-32a)$$

The thermal energy E_v also includes the zero-point energy contribution. The free energy F , at the temperature T , can then be evaluated from the internal energy U , which is calculated at 0 Kelvin, the thermal energy E_v and the entropy S_v :

$$F = U + E_v - TS_v \quad (2-33)$$

2.7 Methods to Evaluate Reaction Barriers

In each elementary step of a chemical reaction, the reactants have to overcome an *energy barrier* or *activation energy*, following the minimum energy pathway, before transforming into the products. The structure with the highest energy along that minimum energy path is called *transition state* (TS). The energy barrier is defined then as the energy difference between the reactants and the TS. From a computational point of view, the energy barrier is evaluated by optimizing the structure at the TS. However, standard minimization methods will drive the system towards the reactants or the products, which are minima in the potential energy surface. It is therefore necessary to use modified procedures to find the optimum structure that is a maximum along the reaction coordinate and a minimum along any other direction, i.e. a saddle point in the potential energy surface. Two methods have been used in the present thesis: the **nudged elastic band (NEB)** method [134,135] and the **improved dimer method (IDM)** [136,137].

The NEB method needs the structures of the reactant and the product as input information in order to develop the search for the TS. This technique starts the exploration of the minimum energy pathway between reactants and products by using an arbitrary number of *images* between both states. The images are evenly

spaced and connected by harmonic springs. The number of images depends on the accuracy and complexity of the problem in question. The perpendicular component of the spring force, which tends to make the images collinear, is zeroed. The same treatment is given to the parallel component of the potential energy gradient, which tends to move the images towards the closest minimum. After a certain number of iterations, the path described by the succession of images should match the minimum energy pathway, and the image with the highest energy should be a good representation of the TS, which is refined using the IDM.

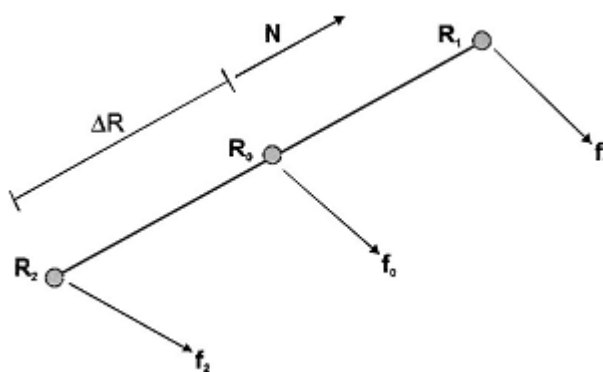


Figure 2-2. Definition of the dimer in the $3n$ -space (adapted from Ref [137] with permission from AIP Publishing LLC).

The IDM was proposed by Heyden and collaborators [137] based on the original dimer method (DM) proposed by Henkelman and Jónnson [136], which only uses potential energy gradients to search for local saddle points, avoiding in this way expensive evaluations of the Hessian matrix during the exploration. The original DM creates the so-called *dimer* with two configurations in the multi-dimensional space, R_1 and R_2 in **Figure 2-2**, separated by a small vector ΔR from the reference structure R_0 . The closer the structure R_0 is from the correct TS the faster the algorithm converges. Consequently, the approximate TS derived from the NEB calculation is an adequate choice to represent the initial configuration R_0 . The dimer is then built

by displacing \mathbf{R}_0 by a positive and a negative amount $|\Delta\mathbf{R}|$ along the hardest imaginary mode calculated for the NEB's TS. The dimer is periodically rotated in order to guarantee that it follows the lowest negative curvature of the potential energy surface until it arrives, after successive translations of \mathbf{R}_0 , to what should be the nearest saddle point. The accuracy of the calculation is controlled by setting a threshold for the ionic forces as a convergence criterion. The IDM retains this operation framework, but it improves the robustness and efficiency of the original DM by increasing the accuracy of the lowest negative curvature evaluation, and decreasing the number of gradients that need to be determined.

2.8 Born Model of Solids

In this thesis, the classic interatomic simulations are based on the Born model of solids [138], which presumes that short- and long-range interactions are sufficient to describe the interactions among ions in a periodic crystal. The potential energy $V(\mathbf{r}_{ab})$ associated with this model is written as:

$$V(\mathbf{r}_a, \mathbf{r}_b, \dots, \mathbf{r}_n) = \frac{1}{4\pi\epsilon_0} \sum_{ab} \frac{q_a q_b}{r_{ab}} + V_{sr}(\mathbf{r}_a, \mathbf{r}_b, \dots, \mathbf{r}_n) \quad (2-34)$$

In (2-34), the first term represents the long-range interaction and consists on the sum of Coulombic interactions between pairs of ions a and b with electric charges q_a and q_b , respectively. The second term describes the short-range interactions.

The real-space representation of the long-range term converges very slowly. This drawback is solved by splitting this term into a short-range contribution, which is treated in the real space, and a long-range contribution, which is represented in the

reciprocal space. Both components converge rapidly in their respective space representations. This procedure is known as the **Ewald method** [139], and allows to calculate the interaction between the ion and its periodic images, repeated infinitely along the three dimensions. The equivalent scheme for two-dimensional systems is given by the **Parry method** [140,141].

The short-range term $V_{sr}(\mathbf{r}_a, \mathbf{r}_b, \dots, \mathbf{r}_n)$ in (2-34) is described by a sum of two- and three-body interactions:

$$V_{sr}(\mathbf{r}_a, \mathbf{r}_b, \dots, \mathbf{r}_n) = \sum_{ab} U_{ab}(\mathbf{r}_a, \mathbf{r}_b) + \sum_{abc} U_{abc}(\mathbf{r}_a, \mathbf{r}_b, \mathbf{r}_c) \quad (2-35)$$

Expression (2-35) includes non-bonding contributions, electronic polarizability and covalent contributions in the form of interatomic potentials. The two-body component has been described in this thesis by the **Buckingham potential** [142]:

$$U_{ab}(\mathbf{r}_{ab}) = A_{ab} \exp\left(-\frac{\mathbf{r}_{ab}}{\rho_{ab}}\right) - \frac{C_{ab}}{\mathbf{r}_{ab}^6} \quad (2-36)$$

where the first term represents the repulsion emerging from the Pauli exclusion principle, and the second term corresponds to the attractive interaction originating from the Van der Waals interactions. The parameters A_{ab} , ρ_{ab} and C_{ab} are fixed during the simulation and are obtained by fitting to experimental data or *ab-initio* calculations.

The three-body term in (2-35) is described by a harmonic potential:

$$U_{abc}(\theta_{abc}) = \frac{1}{2} k_{abc} (\theta_{abc} - \theta_0)^2 \quad (2-37)$$

where k_{abc} is the harmonic force constant, θ_{abc} is the angle between the vectors \mathbf{r}_{ab} and \mathbf{r}_{bc} and θ_0 is the equilibrium angle.

2.8.1 Core-Shell Approximation

The ions in the lattice may be considered as point charges, with interionic interactions dictated by expression (2-34), and no possibility of developing a dipole moment when an electric field is applied. However, cases exist where it is needed to include the effects of the electronic polarization. The relation between the dipole moment $\boldsymbol{\mu}$ and the applied electric field \mathbf{E} is given by the electronic polarizability α of the ion:

$$\boldsymbol{\mu} = \alpha \mathbf{E} \quad (2-38)$$

The polarizability is classically included by dividing the ion into a core and a massless shell linked by a harmonic spring with force constant k_{csh} [143]:

$$V_{csh}(\mathbf{r}_{csh}) = \frac{1}{2} k_{csh} r_{csh}^2 \quad (2-39)$$

The force constant k_{csh} and the portion q_{sh} of the total ionic charge assigned to the shell are used then to calculate the electronic polarizability α :

$$\alpha = \frac{q_{sh}^2}{k_{csh}} \quad (2-40)$$

The values of q_{sh} and k_{csh} are fitted in order to reproduce experimental data, such as the dielectric or elastic constants. In the present thesis, the core-shell model was only applied to the oxygen atoms of the zeolite framework.

Chapter 3 Structure of MFI Nanosheets

3.1 Introduction

The confinement of molecules inside the zeolite micropore network affects the catalytic rate [144] and also determines the reaction selectivity by controlling the movement of reagents, intermediaries or products throughout the pore system [145]. However, although confinement effects form part of the exceptional features of zeolites as catalysts, it can also have an adverse effect, when the products get trapped inside the pores, thereby provoking undesired secondary reactions [54]. Several schemes have been launched to increase the mobility of molecules toward and from the active sites by combining micropore (< 2nm) and mesopore (2-50 nm) frameworks. This hierarchization of the zeolite pore structure allows an improvement in the catalyst efficiency, owing to faster diffusion to, and better accessibility of, the active sites [146].

The conventional three-dimensional (3D) zeolite structure may be confined into a two-dimensional (2D) one by reducing the size of the crystal along a specific direction to just few nanometers. These layered materials are obtained through different methods, including direct synthesis or modification of layered zeolite precursors [60,61]. The interlayer separation can be tailored within the mesoscale which, together with the micropore network, allows the hierarchization of the system. Thirteen zeolite frameworks are currently known to have 2D versions [60]. Among them, the MFI type [147] has been the subject of extensive experimental research, mainly by Ryoo and co-workers who reported the first method to synthesize

MFI nanosheets. Their method employs diquatary ammonium-type surfactants as structure-directing agents (SDA) with hydrophobic and hydrophilic functionalities [54]. Later works have focused on the control of the thickness and mesopore dimension, together with the function of each segment of the surfactant [57,58,148].

MFI nanosheets show remarkable thermal, hydrothermal and mechanical stability [54,58,149]. Furthermore, this material retains the acid strength displayed by the bulk crystal, which, in conjunction with the highly enhanced external surface, allows the treatment of larger molecules than normally fit inside the pores [58,150]. Although this structure is very thin (~ 2 nm), it conserves the crystallinity within the *a-c* plane and hence the pore system. Therefore, the nanosheet continues to show selectivity in the Beckmann rearrangement [151] and the epoxidation of large molecules [150], as well as the disproportionation and alkylation of toluene [152] and the selective oxidation of benzene [153].

Layered MFI has an effective lifetime as a catalyst. The nanosheets combine small pore lengths along the straight channels (*b*-axis) with an enhanced availability of active sites at the external surface (see **Figure 3-1**). As a result, not only is the residence time reduced, but the poisoning effects of secondary reactions taking place inside the pores are also diminished [54,151,153]. Accordingly, MFI nanosheets are an exceptional material which maintains the bulk-type features, but with additional improvements, such as increased mass-transfer and accessibility for bulky compounds.

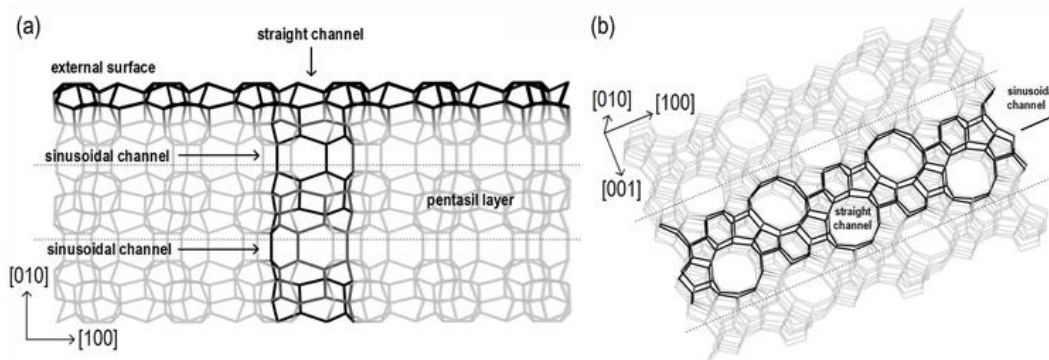


Figure 3-1. (a) Lateral view of the three-pentasil slab (the framework is created by linking the silicon atoms, oxygen atoms are not shown). The pentasil layer at the centre of the slab is contained between dotted lines. The twenty four silicon atoms per unit cell at the external surface and those of the straight channel are highlighted with darker bonds. The sinusoidal channels run along the interception of two pentasil layers. (b) Top view of the three pentasil slab. The sinusoidal channel which connects neighbouring straight channels is highlighted with darker bonds.

Although the experimental work on MFI nanosheets is extensive and has shown the interesting potentials of this type of structure, computational tools can provide a fundamental understanding of their properties at the atomic level, thereby helping to speed up the route to MFI applications. For instance, Varoon *et al.* reported the optimization of the layered structure of MWW and MFI zeolites for different thicknesses using Car-Parinello molecular dynamics [154], although they investigated the pure-silica structure under relaxation restrictions. Park *et al.* have carried out interatomic potential calculations to understand the effect of surfactants in the final arrangement of the nanosheets [148]. Molecular dynamics studies have examined the capacity of MFI to act as a membrane for seawater desalination [155] and argon adsorption in layered zeolites [156].

The properties of layered MFI remain of interest, both from a fundamental point of view and for new applications. In this study, we have carried out a systematic examination of a number of MFI nanosheets, including the substitution of silicon atoms in each independent T-site by aluminium. Furthermore, a complete vibrational

analysis was performed of both silanols and bridging oxygens binding a proton as counter-ion. Finally, the main features in the electronic structure before and after aluminium inclusion were analysed by means of the projected density of states (PDOS) scheme.

3.2 Computational Methods

We have carried out the present thesis using two techniques: (i) atomistic simulations based on the Born model of ionic solids [138] and (ii) Density Functional Theory (DFT) calculations [93,94]. The first method was used to study possible terminations of the MFI zeolite surface perpendicular to the [010] direction (the normal vector to the MFI nanosheet plane is collinear with [010] [54]). For this purpose we employed the METADISE code [86], considering the surface dipoles in accordance with the approach by Tasker [157,158]. The model definition is outlined in Section 1S of the Supplementary Information (ESI). By using these interatomic potentials the energy of the system comprised two main contributions: one arising from the Coulombic interactions computed using the Parry technique [140,141], and the other from the short-range repulsions and Van der Waals attractions defined by Buckingham potentials [142]. In the parameterization of the interatomic interactions we have used the potential model for SiO₂ derived by Sanders *et al.* [159], together with the compatible parameters for the hydroxide ion by Baram and Parker [160]. Sanders and co-workers showed the suitability and accuracy of the Born model (initially designed for the study of ionic solids) to simulate covalent materials in the form of SiO₂ polymorphs (α -Quartz, α -Cristobalite, Coesite and α -Tridymite) [159]. The main modifications consisted in the addition of harmonic bond-bending terms to describe the rigidity of the SiO₂ tetrahedra, and the inclusion of the shell model to effectively

describe the polarizability of the O atoms within the structure [159]. Later works have shown the validity and transferability of the model when studying different zeolite frameworks [161–163].

For the DFT calculations we have employed the Vienna Ab-initio Simulation Package (VASP) [82–85] to carry out full structural relaxations of the pure-silica and Al-substituted MFI within the slab model. The maximum kinetic energy for describing the valence electrons was set to 500 eV, while their nodal features and interactions with the internal electrons of the atoms were considered through the projector-augmented-wave method (PAW) [113,114]. The Generalised Gradient Approximation (GGA) within the Perdew, Burke and Ernzerhof (PBE) functional [100] accounted for the exchange and correlation effects of the electronic system under the Born-Oppenheimer approximation [90]. The Grimme method [124] was applied with the DFT methodology (DFT+D2) to include the effect of the long-range interactions [164–167]. The Monkhorst-Pack [108] scheme was used to generate the grid for the numerical integration over the Brillouin zone; we have only considered the Gamma point due to the large size of the MFI unit cell. The threshold was set at 10^{-5} eV for the electronic iterations and any movement of the ions was stopped when the forces were smaller than $0.03 \text{ eV}/\text{\AA}$. The threshold for the electronic iterations was further decreased to 10^{-7} eV in order to improve the accuracy of the forces when performing the vibrational analysis. The electronic convergence was improved via smearing of the electronic states by a fictitious temperature of $k_{\text{B}}T = 0.1 \text{ eV}$, although the final total energies were reported at 0 K [117]. The O-H frequencies were calculated using the finite difference technique where positive and negative displacements, along each Cartesian coordinate, are performed for each atom; these displacements ($\pm 0.015 \text{ \AA}$) are sufficiently small to keep the system within the

harmonic limit. The Hessian matrix (second derivative of the energy with respect to the atomic displacements) is then calculated and its diagonalization allows to obtain the vibration frequencies.

The slabs were constructed by truncating the bulk system along the [010] direction as shown in **Figure 3-1**. Two values for the thickness were used: (i) a single unit cell, or equivalent, consisting of two pentasil layers (312 atoms), and (ii) a second slab represented by three pentasil layers (456 atoms). The dangling Si-O bonds were saturated with H, thus generating silanol groups. The area of the slab surface was 272.5 \AA^2 . In order to minimize any interaction between periodic images, we set the thickness of the vacuum layer that separates successive slabs at 20 \AA . In addition, the correction for the dispersion forces was considered up to a maximum distance of 15 \AA (this cutoff was used for both bulk and slab calculations for consistency).

The visualization of the zeolite structure was generated with the code *Visualization for Electronic and Structural Analysis* (VESTA 3) [168].

3.3 Pure-silica MFI

3.3.1 Bulk Structure

Pure-silica MFI zeolite has a monoclinic structure ($P2_1/n$) which undergoes a phase transition toward an orthorhombic symmetry ($Pnma$) at temperatures above the range 317-325 K; these temperatures decrease with Al content [45]. The orthorhombic phase was employed throughout the present thesis mainly justified by the synthesis conditions and the use of this material as a catalyst above 320 K.

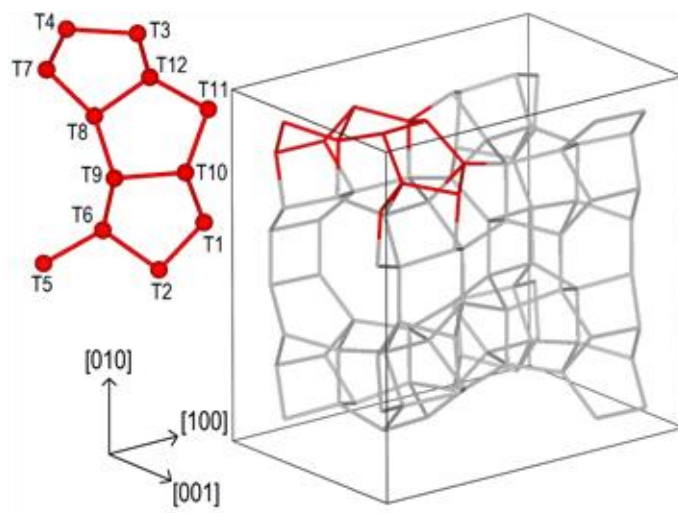


Figure 3-2. MFI zeolite unit cell. The oxygen atoms were deleted for better view. The framework is created by linking the silicon atoms. The section in red represents the twelve non-equivalent T-sites with their numeration.

The starting atomic positions and cell parameters were extracted from the structural database of the International Zeolite Association (IZA) and further optimized keeping the orthorhombic symmetry; **Figure 3-2** shows the MFI unit cell. For the GGA calculations under periodic boundary conditions, the energy cutoff for the plane wave basis set (500 eV) was still too small to avoid the effects of Pulay stress if the simultaneous optimization of the volume cell and atomic positions would have been chosen. This problem was overcome by performing fixed-volume relaxations of a set of lattices within the range $V_0 \pm 0.1V_0$, where V_0 was the volume of the cell from the IZA database. The Pulay stress is almost isotropic [169], and hence, cancels out when the correlation of the lattice energy versus the volume is fitted to an equation of state; in the present case the Birch-Murnaghan equation [170]. An additional advantage of this method is that the Bulk modulus is obtained directly from the fitting as an adjustable parameter. Whereas, the optimization of the lattice using the Interatomic Potential (IP) technique was carried out upgrading simultaneously the volume and the atomic positions. The final volume of the relaxed

IP lattice was then rescaled ($\pm 10\%$ of that volume) to create the set of fixed-volume relaxations to obtain the Bulk modulus by fitting to the Birch-Murnaghan equation. **Table 3-1** summarizes the results of the optimizations using the experimental work of Quartieri *et al.* [171] for comparison. The distribution of distances and angles for each method are shown in **Figure A-1**.

Table 3-1. Cell vectors and bulk modulus (B) of the orthorhombic MFI zeolite ($Pnma$) calculated with Interatomic Potentials (**IP**), pure **PBE** and GGA together with the long-range dispersion correction (**PBE+D2**).

	a (Å)	b (Å)	c (Å)	B (GPa)
IP	20.136	19.829	13.408	54.1
GGA	20.476	20.243	13.595	24.3
GGA+D2	20.317	19.979	13.413	18.0
Exp. ^a	20.140	19.930	13.426	18.2

^aFrom Ref [171]

The IP method accurately reproduced the cell parameters of the MFI framework. Although an underestimation of the three vectors was noted, the largest discrepancy (along b) remained below 1%. However, it was observed a large disagreement in the calculated bulk modulus with respect to the experimental reference (see **Table 3-1**). Pure PBE overestimated almost isotropically the experimental cell vectors by between 1.3 and 1.7% while the bulk modulus was 33% larger in comparison with the experimental value. Inclusion of the long-range correction was necessary to improve the DFT outcome [172]; the largest mismatch was reduced to less than 1% for PBE+D2, with a and b longer than the experimental values and c slightly shorter. In addition, the bulk modulus was only marginally different from the reported one by less than 1%. As such, the PBE+D2 combination appears suitable for the description of further distortions within the cell derived from the replacement of Si by Al atoms.

The IP Si-O distances spanned a range of 1.587 to 1.606 Å with an average value of 1.597 Å, with the main distribution peaks staying around 1.60 Å (see **Figure A-1**). In the case of PBE and PBE+D2 practically the same minimum and maximum values were found, extending from 1.615 to 1.631 Å with average values of 1.624 and 1.625 Å respectively. The intra-tetrahedral angle distribution for IP ranged from 106.4 to 112.4° which was larger than PBE (107.0 – 111.4°) and PBE+D2 (107.5 – 111.8°). However the three average angles were 109.5°, i.e. essentially the ideal tetrahedral angle. Finally, the inter-tetrahedral angles ranged over 26° for IP and 35° for PBE and PBE+D2 whose mean numbers were 152, 154 and 149° respectively.

Overall, the Si-O distances differed most when IP was compared with PBE and PBE+D2. The better performance of PBE+D2 over PBE to predict the Si-O character may be associated with the smaller inter-tetrahedral angles. The use of these techniques in the rest of this thesis was split in two: (i) IP was used to study the relative stability of the hydrated terminations of the (010) surface (see next section) and (ii) the DFT+D2 was employed to perform all calculations concerned with Al substitution.

3.3.2 Nanosheet Structure

The MFI nanosheet was first reported as a layered structure composed of three pentasil sheets [54]. Further work showed the possibility of reducing its thickness to two pentasils layers leading to a single row of micropores along the [001] direction [58]. We have carried out a full geometry optimization with both thicknesses and compared their structural features with the bulk system.

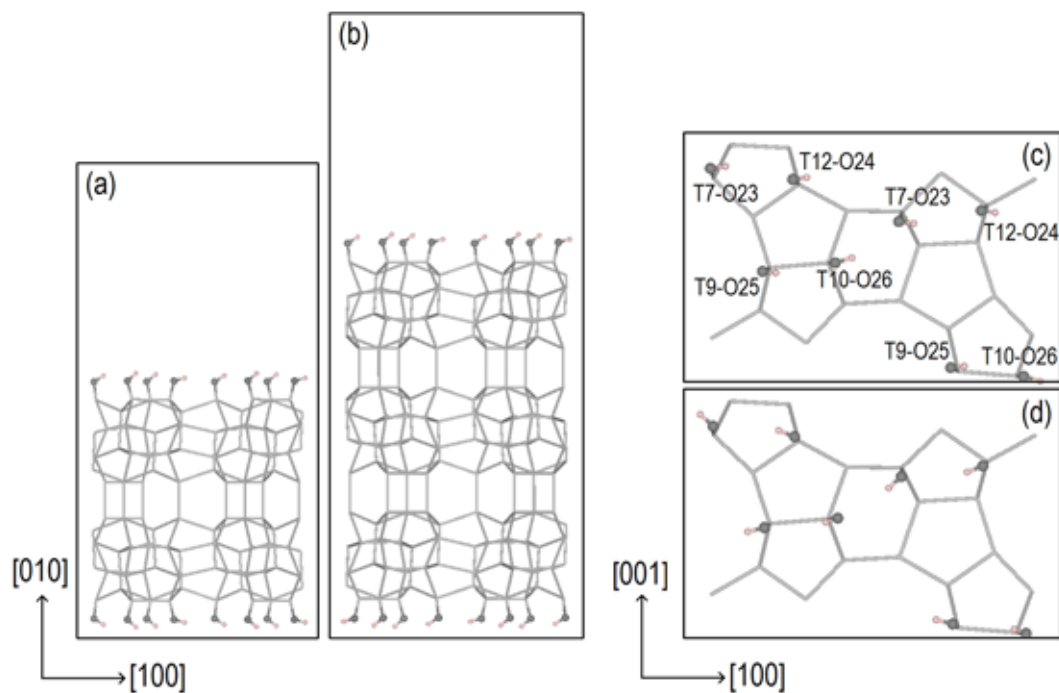


Figure 3-3. Pure-silica slabs formed by two (a) and three (b) pentasil layers; the black lines denote the supercell box. The silanol hydrogen atoms are oriented towards their nearest silanol groups. Following this scheme two configurations for the hydrogen atoms are obtained, labelled along the text as configuration A (c) and B (d). The silicon atoms are located at the interception of the grey sticks and the framework oxygens were eliminated for a better view. The silanol oxygens are represented with dark grey balls and the hydrogens with light pink balls. Each silanol is labelled according to the numbers of the T-site and oxygen atom that carries the hydrogen.

Previous experimental [59] and computational [154,156] studies of layered MFI have not considered any other surface termination than the full pentasil layer. However, we have also investigated other terminations to identify surfaces with maximum numbers of Si-O-Si bridges and minimum numbers of hydroxy groups per terminal Si. As a result, 203 different structures were obtained, each of them carrying a single hydroxy group per Si atom and ranging in the number of hydroxy groups per unit cell from eight to twenty depending on the termination. These surfaces were optimised using IP with five cells representing the bulk and a single cell for the surface (see ESI for more information). We have plotted the energies

against the number of hydroxy groups per unit of area, revealing the full pentasil layer as the most likely hydrated surface for the MFI zeolite perpendicular to the [010] direction (see **Section 3S**, ESI). Hence, the full pentasil layer with eight hydroxy groups per unit cell at its surface was chosen as the slab model for the remaining calculations employing DFT.

The orientation of the H atoms in the surface silanol groups are expected to change constantly under experimental conditions. However, if this effect is considered, the number of possible configurations to be examined is too large. We weighted two different options: *(i)* to orientate the H atoms randomly, or *(ii)* to orientate the H atoms in the same direction toward their nearest silanol O atoms as shown in **Figure 3-3**. The second alternative was preferred and as a result two H configurations were investigated (see **Figure 3-3**).

Non-terminal atoms did not suffer any appreciable distortion when the optimized slabs were compared with the bulk (see **Figure A-2**). The distances and angles essentially spanned the same ranges as the bulk-type structure: 1.61 and 1.63 Å for the Si-O distances and 107 – 112° and 134 – 170° for the intra- and inter-tetrahedral angles, respectively. Consequently, the average values remained unchanged, with a 0.001 Å variation for the Si-O distances, and constant 109.5° and 150° values for the intra- and inter-tetrahedral angles, respectively.

Two methods have been used experimentally to obtain the nanosheet thickness: *(i)* AFM showing a thickness of 3.4 ± 0.3 nm [154], which is very similar to the 3.0 nm value calculated here if the hydroxy O atoms are used as limits for the three-pentasil slab, and *(ii)* transmission electron microscopy (TEM) images (2.5 nm) [59] which are also close to the 2.7 nm obtained here considering the Si heights for the same

slab. As to the two-pentasil nanosheets, a maximum value of 1.7 nm, with an average of 1.5 nm, is reported by TEM studies [58] which corresponds to our 1.7 nm if the Si atoms are assumed as slab limits. Overall the nanosheets do not suffer of any expansion or contraction in the b direction as a result of the crystal truncation.

Finally, the relative energies of the two hydroxy orientations depicted in **Figure 3-3** showed a slight preference for configuration B independent of the slab thickness; the two-pentasil configuration B was favoured by 14 kJ/mol, decreasing in the three-pentasil to 5 kJ/mol relative to configuration A. It is perhaps worth mentioning that the distances between the silanol H atoms and their nearest silanol hydroxy groups were smaller in configuration B.

The above results confirm a highly stable two-dimensional framework with practically no modification compared to the bulk crystallinity [154]. The minor structural variations in the bond distances and angles are restricted to the atoms related to the silanol groups, which will be analysed in subsequent sections. The overall trends are also shown not to be dependent on the thickness of the sheets.

3.4 Aluminium-substituted MFI

3.4.1 Bulk Structure

The Si substitution by Al atoms within the 3D MFI framework has been studied before using both cluster methods [173–176] and those based on periodic boundary conditions [172,177–179]. We performed a similar analysis in order to compare these results with those derived from the Al-substituted 2D structure. To this end, we systematically studied the substitution of one Si by Al per orthorhombic unit cell in all non-equivalent T-sites (12 configurations), allowing full relaxation of the

atomic positions. To determine the energetic stability of the doped systems, we have mainly focused on the location of the proton near each individual Al-centred tetrahedron, instead of using an Al-siting probability determination, because the Al occupation of a particular T-site is not random but depends highly on the synthesis conditions and Si/Al ratio [180]. The protons are added by the calcination of the ammonium-exchanged zeolite with the Al atoms already in the framework.

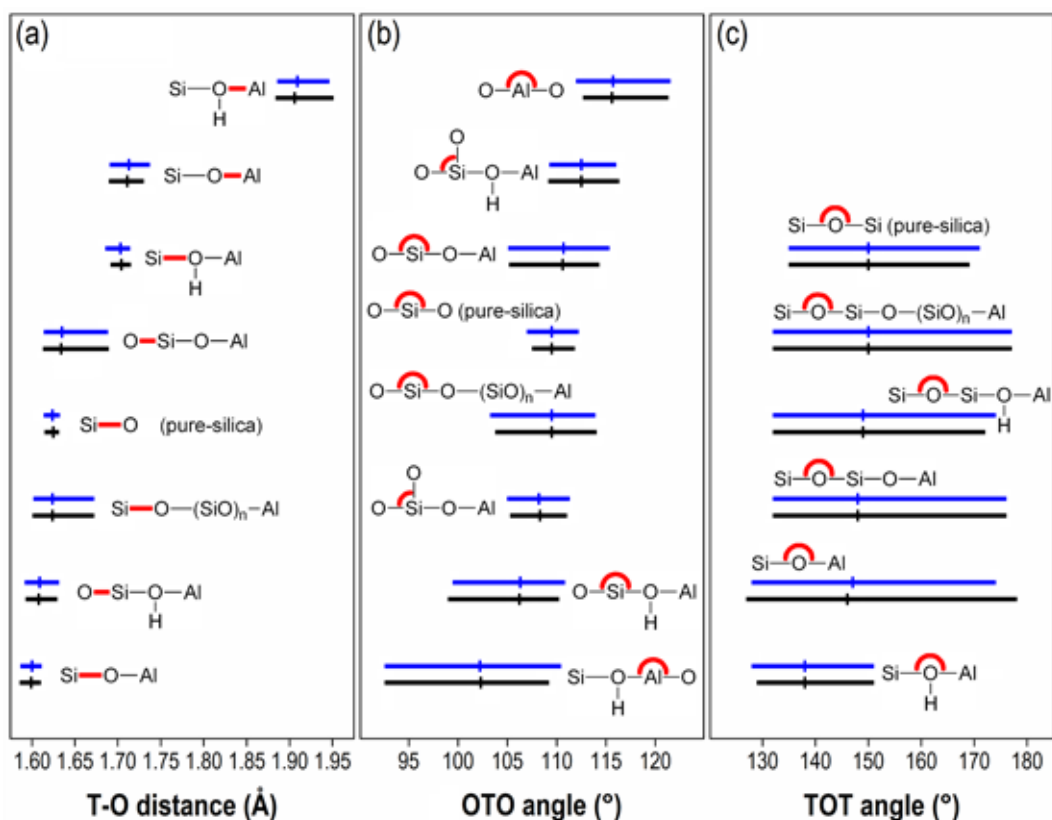


Figure 3-4. Scattering of the T-O distances (a), O-T-O angles (b) and T-O-T angles (c) for the framework T-sites and oxygen atoms in the Al-substituted bulk (horizontal lines in black) and two-pentasil slab (horizontal lines in blue). The horizontal lines establish the scattering ranges for the distances and angles; the average values are marked with small vertical lines. The structural scheme, besides each set of lines, highlights in red the distance or the angle to which the range of values is referring.

The position of the proton as counter-ion was also varied among the four O atoms that form the Al tetrahedron. As such, a total of 48 structures were fully optimized

using the PBE+D2 method. A summary of the final structural parameters is compiled in **Figure 3-4**. We observed that the first neighbouring layer around the Al atom captures the main distortions within the structure.

The biggest distortions in the Si-O distances are observed for those tetrahedra sharing corners with Al. They ranged between 1.586 and 1.715 Å, which represents a 0.029 Å decrease of the lower limit and a 0.084 Å increase of the upper limit when compared with the pure-silica bulk (see **Figure 3-4**). The contraction of the Si-O distances was mainly due to Si binding the non-protonated O atom that is directly bonded to Al, spanning from 1.586 to 1.610 Å with 1.599 Å as the mean. The expansion of the Si-O distances was related to Si atoms binding the protonated O, varying between 1.692 and 1.715 Å with an average of 1.704 Å. Further expansions and contractions were found, although to a lesser extent, for the Si-O distances that connect the nearest Si atoms to the Al atom with the rest of the framework (see **Figure 3-4**). Those atoms beyond the first Si-coordination sphere of the Al atom conserved features very close to that of the pure-silica structure. Nevertheless, expansion of some Si-O distances was found for Si atoms at more than one O from the Al, due to H-bond formation between the proton as counterion and a framework O atom. This additional elongation of the Si-O bond will be analysed in detail when discussing the silanol groups. The Al-O bonds showed similar trends, but escalated according to the covalent radius ratio Al/Si: the Al-O bond varied between 1.690 and 1.730 Å, while the Al-O(H) stayed within 1.884 to 1.951 Å.

As to the intra-tetrahedral angles, the main changes were also limited to those Si atoms at less than 4.0 Å from the Al. The (Si-)O-Si-O(-Al) intra-tetrahedral angles varied from 105.2 to 114.3°, an average 1.1° above the mean of the pure-silica bulk. The inverse trend was noted for (Si-)O-Si-OH(-Al) angles, at an average 3.3° smaller

than that corresponding to the pure-silica structure. Meanwhile, the Al atoms showed the same tendency: intra-tetrahedral angles formed by the protonated O were always smaller than those without proton, differing their average angles by 13.3° (see **Figure 3-4**). Thus, either the Si or the Al tended to get closer to a plane formed by the three O atoms of the tetrahedron opposite to the OH group, thereby decreasing the corresponding intra-tetrahedral angles; the inverse trend occurred with the non-protonated O atoms.

The main feature in the inter-tetrahedral angles was the narrower distribution for the OH groups (see **Figure 3-4**), whose angles varied between 129 and 151° , i.e. 11° below the mean of the pure-silica framework. This is a clear indication that OH tends to have inter-tetrahedral angles closer to 120° which corresponds to the ideal value of a tri-coordinated species.

3.4.2 Nanosheet Structure

The differences encountered between both H configurations (configurations A and B in **Figure 3-3**) for the pure-silica nanosheets were negligible. The same applies for the slab thickness. Therefore, to avoid the duplication of the calculations, we chose the two-pentasil slab with H configuration B (see **Figure 3-3**), whose pure-silica version was 14 kJ/mol more stable than A, to examine the effect of a single Al substitution on the nanosheet framework.

The number of non-equivalent T-sites for the two-pentasil slab increased to 24. For each framework T-site (20 sites), the proton may be bonded to four different O atoms. In the case of substitutions taking place in silanol positions (4 sites, see

Figure 3-3) the number of possible positions for the counter-ion reduces to three (one of the O atoms forms part of the silanol group); a total of 92 structures.

Practically none of the features described in the previous subsection changed when the slab framework was compared with the bulk-type structure. The average Si-OH(-Al) distance increased to 1.703 Å, observing the opposite effect for Si-O(-Al) distances; in this case the average value dropped to 1.600 Å. The (Si-)O-Si-OH(-Al) and (Si-)O-Al-OH(-Si) intra-tetrahedral angles tended to decrease (106.3° for Si and 102.2° for Al on average). The inverse trend occurred when the O atom was not protonated but served as a bridge between a Si and an Al (110.7° for Si and 115.7° for Al in average). As in the bulk, the inter-tetrahedral angle was prone to decrease towards the ideal value (120°) for protonated bridging O atoms (see **Figure 3-4**). The main distortions appeared, however, when the silanols and the Al-substituted silanols were analysed.

3.5 Silanols and Al-substituted Silanols

Four sets of silanol groups were derived from the Al substitution: (i) silanols without Al as a nearest neighbour, (ii) silanols with Al as a nearest neighbour connected through the non-protonated O atom, (iii) silanols with Al as a nearest neighbour connected through the protonated O atom and (iv) the Al atom replacing the Si at the silanol position. **Figure 3-5** shows the structural schemes that represent each type of silanol, while **Table 3-2** compiles the values of O-H vibration frequency and O-H bond distance corresponding to the silanol hydroxyl groups.

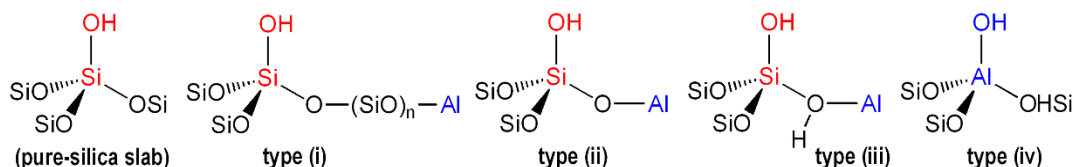


Figure 3-5. Structural schemes representing the different types of silanol groups at the external surface of the zeolite: silanol of the pure-silica slab; *type (i)*, silanol whose silicon atom does not have the aluminium as nearest neighbour; *type (ii)*, silanol whose silicon atom is directly connected to the aluminium through the non-protonated oxygen; *type (iii)*, silanol whose silicon atom is directly connected to the aluminium through the protonated oxygen; and *type (iv)*, aluminium-substituted silanol.

Table 3-2. Summary for the O-H vibration frequency [$\nu(\text{O-H})$] and O-H bond distance (**O-H dist.**) of the different types of silanol groups within the pure-silica and aluminium-substituted slabs. Three values are given for each entry: minimum, average (bold numbers within parenthesis) and maximum values. The silanol **types** are represented in **Figure 3-5**.

	$\nu(\text{O-H})$ (cm^{-1})	O-H dist. (\AA)
pure-silica silanols	3792 (3805) 3815	0.969 (0.970) 0.970
type (i) silanols	3735 (3803) 3824	0.969 (0.970) 0.973
type (ii) silanols	3752 (3803) 3818	0.969 (0.970) 0.972
type (iii) silanols	3785 (3793) 3800	0.970 (0.971) 0.971
type (iv) silanols	3825 (3853) 3871	0.965 (0.966) 0.968

The silanol O-H bond distances, within the pure-silica two-pentasil slab with H configuration B (see **Figure 3-3**), varied within a very narrow interval: from 0.969 to 0.970 \AA (see **Table 3-2**), and the stretching frequency of these O-H groups remained in the range of 3792 – 3815 cm^{-1} . The average value was 3805 cm^{-1} , although this is 60 cm^{-1} above the experimental value [150,151]. The overestimation of the O-H frequencies is inherent to the harmonic approximation used here to perform the vibrational analysis. Previous reports have shown that the frequencies decrease and get closer to the experimental references if the anharmonicity is taken into consideration [181–183]. However, the suitability of the finite-difference method has been reported before in the case of the mordenite surfaces using the PW91 functional [184]. Furthermore, the comparison between isolated and non-

isolated hydroxy groups is of interest when studying their accessibility and proton-donor capacity; the shift provoked by the H-bond interaction (500 cm^{-1}) [185,186] is well above the 60 cm^{-1} error.

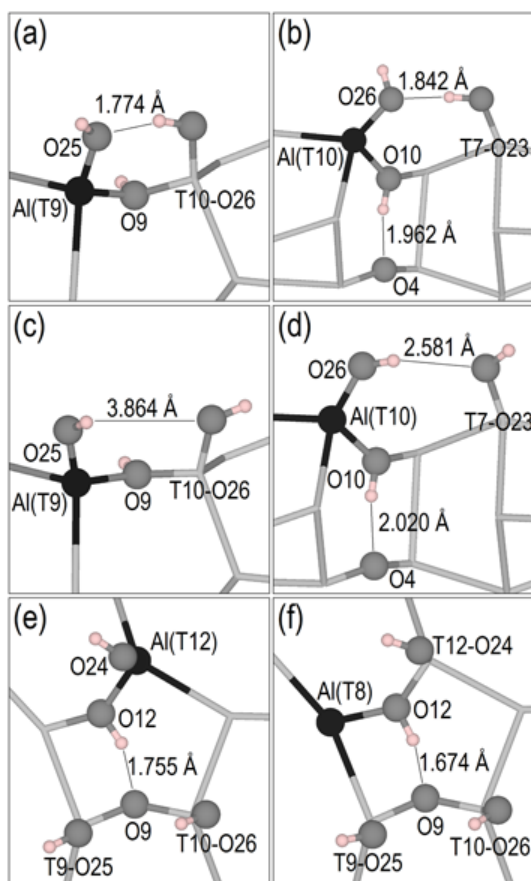


Figure 3-6. Local structure for different aluminium-substituted sites highlighting the features of specific hydrogen-bonds. The silicon atoms are located at the interception of the light grey sticks, and the non-important oxygens are not shown for a better view. Silanol oxygens and framework oxygens involved in the hydrogen-bonds are represented with dark grey balls, the hydrogens with light pink balls and the aluminium with a black ball.

Once the Al substitution has taken place, some of the non-substituted silanol O-H distances suffered a slight elongation up to 0.973 Å . The related O-H frequencies decreased to a lower value of 3735 cm^{-1} . There were no appreciable differences in the average values between those silanols with Al as nearest neighbour and those at more than two bridging O atoms away from the Al (see **Table 3-2**). However, there

were two exceptions to the average as a consequence of H-bond formation between the non-substituted silanol H atom and the Al-substituted silanol O atom as shown in **Figure 3-6a** and **Figure 3-6b**. In both cases, the silanol O-H frequencies dropped below 3300 cm^{-1} and the O-H distances increased above 0.990 \AA . The first resulted from the vicinal interaction of silanols when the Al occupies the T9 position (**Figure 3-6a**), and the second derived from the interaction between the Al-substituted silanol T10 and the silanol T7 two O atoms farther away (**Figure 3-6b**). However, no H-bond formation between the Al-substituted silanol H and the non-substituted silanol O atoms was observed. As shown in **Figure 3-6c** and **Figure 3-6d**, the (Al)O-H \cdots OH(Si) distance was always larger than 2.5 \AA . Meanwhile, the O-H stretching frequencies for the Al-substituted silanols increased with respect to the conventional silanol average by at least 36 cm^{-1} . This highlights a weaker Al-OH_{surf} bond which may evolve into Lewis acid formation by dehydration.

Regarding the silanol-related structural parameters (see **Figure A-5**), the Si-OH_{surf} distances were the properties that differed the most compared to the bulk values. In the case of the pure-silica slab, an elongation of the Si-OH_{surf} bond is noted with an average of 1.637 \AA versus 1.625 \AA of the bulk. The Al inclusion increased further this value if the silanols were bridged through the non-protonated O to the Al atom. The opposite tendency occurred with the protonated bridging O, reducing the Si-OH_{surf} distance to an average of 1.628 \AA .

Intra-framework H-bonds also caused the elongation of the Si-O distances for Si at more than two O atoms away from the Al. For instance, in **Figure 3-6e**, if the Al is substituting the silanol T12-O24 and the proton is on O12, it forms a 1.755 \AA H-bond with O9. Consequently, the T9-O9 and T10-O9 distances increase to 1.654 and 1.671 \AA , respectively. This effect is repeated for every intra-framework H-bond

formed in the bulk and slab; O atoms with the correct environment to establish this kind of interaction are compiled in **Table 3-3**.

Overall, the alterations of the zeolite structure after the Al substitution have a local character that do not extend beyond the first sphere of tetrahedra around the Al centre. This applies identically for both the 2D and 3D systems. Also, the crystalline structure formed by sharing-corner SiO₄ tetrahedra is highly stable, making the 2D segment indistinguishable from the equivalent portion within the 3D framework (see **Figure A-2**, **Figure 3-4** and **Figure A-5**). Therefore, differences in chemical behaviour will be only derived from the morphology modification, because the increment of the external area versus the total volume will allow to larger molecules to have access to the active sites. In addition, Lewis centres will be easily found at the external surface once the dehydration of Al-substituted silanols takes place; in the 2D system the role of the Lewis acidity will increase with respect to that of the Brønsted acids.

3.6 Lewis Centre Formation

The dehydration process of Al-substituted silanols, with the subsequent formation of Lewis centres, was considered by analysing Al-silanol T9(Al)-O25. This position has the additional feature of an intra-framework H-bond between O9 and O12, when O9 (connected to T9) binds the proton; the O9-H...O25 distance was 1.694 Å after optimization. Also, this silanol is in vicinal position with respect to silanol T10-O26 (see **Figure 3-6c**). We have studied three different paths for the dehydration reaction, each of them accounting for a different framework O atom that simultaneously binds

the proton and the Al atom (for T9 site, O8, O9 and O18). We followed the sequence O8, O18 and O9 as shown in **Figure 3-7**.

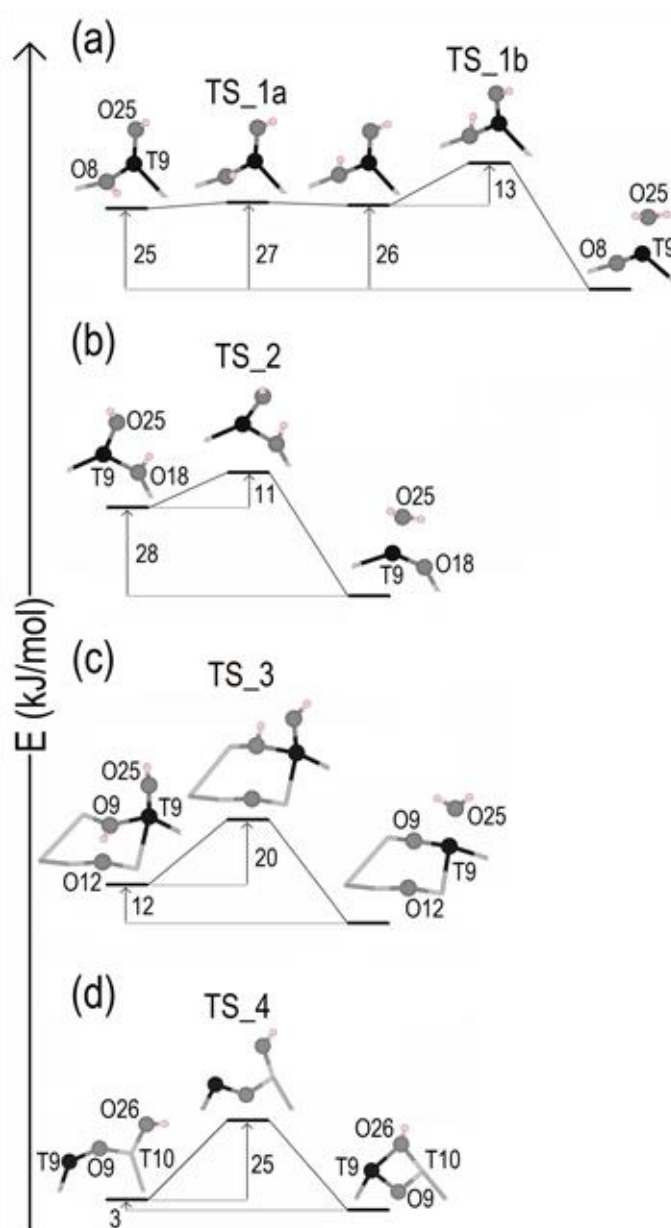


Figure 3-7. Energy profile of the dehydration reaction of aluminium-substituted silanol T9-O25, when the proton is binding the oxygen atoms O8 (a), O18 (b) and O9 (c). The formation of a 2MR with a vicinal silanol group, once the Lewis center has been created, is considered (d). The Nudge Elastic Band Method (NEB) was used to optimize the structures along the reaction path [134,135]. The aluminium atom is represented with a black ball, oxygens with dark grey balls, hydrogens with light pink balls, and silicons are located at the interception of the light grey sticks.

When O8 is protonated, the O8-H bond is almost parallel to the surface, and thus far from O25 (see **Figure 3-7a**). The first stage of the dehydration is featured by the vertical tilt of the proton with a mere activation energy of 2 kJ/mol, which points to a constant flipping of the O8-H bond at normal temperatures. The energy barrier for the proton transfer toward O25 is 13 kJ/mol. Thereafter, the lattice energy decreases to a stable configuration where a water molecule is adsorbed on the Lewis centre. This final arrangement is 25 kJ/mol more stable than the initial Al-silanol. Bučko and co-workers, studying Al-silanols at the (001) surface of mordenite, found an energy barrier of 10 kJ/mol for the proton transfer, and a further system stabilization of 45 kJ/mol following the dehydration. These results allowed the authors to explain why it is less probable to find Brønsted acids at the external surface of zeolites: the less stable external acid sites are destroyed even at modest temperatures releasing water during the process [187].

In the second dehydration path (proton attached to O18, see **Figure 3-7b**), the O18-H bond is almost perpendicular to the surface, placing the proton at close distance from O25. Hence, we have found a single energy barrier of 11 kJ/mol to be crossed for the formation of water. Again, the configuration with water adsorbed on the Lewis centre is 28 kJ/mol more stable than the Brønsted acid.

The third case involved the deprotonation of O9, whose proton forms a strong H-bond (1.694 Å) with the neighbour O12 (**Figure 3-7c**). We have used the H configuration A (see **Figure 3-3**) for this specific configuration to avoid the formation of the H-bond between the Al-silanol T9(Al)-O25 and silanol T10-O26 when O9 is binding the proton (see **Figure 3-6a**). Although the orientation of the O9-H bond is parallel to the surface, with the proton far from O25, we did not find an intermediate configuration which puts the proton in a more favourable position

to be transferred, as it was the case of the path in **Figure 3-7a**. Also, the energy barrier increases from around 10 kJ/mol in the previous two configurations to 20 kJ/mol (see **Figure 3-7c**). We related this outcome with the occurrence of the H-bond O9-H...O25, which makes the proton less prone to be transferred while stabilizing the Al-silanol. However, this effect does not invert the stability relation between the dehydrated arrangement and the Al-silanol, the latter continues being 12 kJ/mol less stable.

We have also studied the formation of two-membered T-O rings (2MR), which occurs when the tri-coordinated Al atom (Lewis centre) is in vicinal position with a silanol group, hereafter Lewis/silanol configuration. The silanol hydroxy group finishes being shared by the Al and the Si. Bučko *et al.* showed that the 2MR further stabilizes the Lewis centre by 9 kJ/mol, with an energy barrier from the Lewis/silanol configuration toward the 2MR of 26 kJ/mol. Also, these authors found that the most favourable position for the silanol H atom is to remain attached to the silanol O atom even after the 2MR formation [187]. In the present thesis, we used the slab with H configuration B (see **Figure 3-3**) turning the O-H bond of the vicinal silanol T10-O26 to favour the Al-OH(-Si) interaction. Our results show practically the same energy barrier (25 kJ/mol in **Figure 3-7d**) as in Ref. [187]. However, although the final 2MR continues being more stable, the energy difference with respect to the initial Lewis/silanol configuration (3 kJ/mol) is less pronounced in comparison with Ref. [187].

Overall, the dehydration products of Al-silanols are energetically favoured, though the presence of intra-framework H-bonds may affect the kinetic of the process. Vicinal silanols groups further promote the formation of Lewis centres since the formation of 2MR stabilizes the freshly formed Lewis acid. In the particular case of

the pentasil layer, which forms the MFI nanosheets, half of the silanols are grouped as vicinal silanols (see **Figure 3-3**).

3.7 Protonated Framework Oxygen Atoms

We studied the probability (P_i) of the proton to bind each of the O atoms of the Al-centred tetrahedron using Boltzmann statistics:

$$P_i = \frac{N e^{-E_i/kT}}{\sum_i e^{-E_i/kT}} \quad (3-1)$$

where N is the degeneracy of each structure (in our present case equal to 1), k is the Boltzmann constant, and T is the equilibrium temperature, chosen as 550 °C, which corresponds to the temperature used in catalytic fast pyrolysis process [65,68]. The index i of the partition sum goes from 0 to 3 in the case of Al-substituted silanols, or from 0 to 4 in any other framework substitution. We assumed that the thermal effects were identical within each set of three or four structures, where only the O atom binding the proton changes, with lesser modifications of the rest of the structure during the optimization. This allowed us to use the calculated lattice energies at 0 K, relative to the most stable configuration inside the set, instead of the free energies at 823 K (550 °C); the entropic effects, zero-point energy contributions and variation in the internal energies cancels out under the constant-volume condition of our calculations.

Table 3-3. Classification of the protons according to the framework oxygen binding them within the **BULK** and **SLAB**. The classification ranges from **Inaccessible protons** to **Accessible protons**. Also, **accessible protons** may be further divided into those with and without *intra-framework H-bonds*. Additionally, the oxygen-hydrogen bond distance (**O-H dist.**), its stretching frequency [**v(O-H)**] and the hydrogen distance to the nearest framework oxygen atom are provided (**OH...O**).

	BULK			SLAB ^a		
	O-H dist. (Å)	v(O-H) (cm ⁻¹)	OH...O (Å)	O-H dist. (Å)	v(O-H) (cm ⁻¹)	OH...O (Å)
Inaccessible protons						
<i>Intra-frame. H-bond^b</i>						
O4	0.982	3600	2.453	0.982	3599	2.459
O9	1.009	3034	1.684 (O12)	1.010	3022	1.673 (O12)
O10	0.986	3509	2.258	0.992	3364	1.926 (O4)
O12	1.008	3054	1.686 (O9)	1.005	3117	1.715 (O9)
O13	1.001	3173	1.750 (O16)	1.000	3212	1.777 (O16)
O16	1.013	2973	1.676 (O13)	1.014	2953	1.660 (O13)
Accessible protons						
<i>Intra-frame. H-bond^b</i>						
O3 (sinusoidal)	1.002	3172	1.788 (O6)	1.000	3217	1.817 (O6)
O6 (sinusoidal)	0.997	3273	1.855 (O3)	0.997	3279	1.870 (O3)
O7 (straight)	0.993	3366	1.970 (O7)	0.976	3708	2.578
O14 (straight)	0.997	3276	1.867 (O19)	1.000	3212	1.816 (O19)
O19 (straight)	1.002	3182	1.790 (O14)	1.004	3147	1.760 (O14)
<i>Isolated^c</i>						
O1	0.975	3730	2.618	0.975	3730	2.609
O2	0.977	3693	2.540	0.977	3701	2.603
O5	0.976	3710	2.534	0.976	3715	2.497
O8	0.976	3715	2.767	0.977	3687	2.506
O11	0.982	3608	2.488	0.979	3669	2.425
O15	0.977	3698	2.499	0.977	3698	2.502
O17	0.977	3699	2.529	0.978	3667	2.428
O18	0.979	3665	2.406	0.979	3653	2.447
O20	0.976	3711	2.584	0.977	3687	2.507
O21	0.977	3700	2.438	0.976	3708	2.474
O22	0.978	3680	2.478	0.977	3691	2.545
O23	0.977	3703	2.505		(silanol oxygen)	
O24	0.978	3679	2.455		(silanol oxygen)	
O25	0.977	3693	2.528		(silanol oxygen)	
O26	0.978	3676	2.709		(silanol oxygen)	

^a The oxygens corresponding to the 12 T-sites closer to the surface termination are listed in the table. The most notable variations were obtained for this set of oxygen atoms.

^b Oxygens binding protons that form intra-framework H-bond. The channel (sinusoidal or straight) where the proton is located is set within parenthesis. The column labelled as **OH...O** states within parenthesis with which oxygen the hydrogen is forming the H-bond.

^c Oxygens binding protons without intra-framework H-bond interactions.

Boltzmann distributions allowed us to analyse the proton tendency to bind each of the four O atoms around a single Al-centred tetrahedron for the 3D and 2D systems; **Figure A-6** shows the individual distributions at a temperature of 550 °C. These results indicate that Al substitutions occurring in the interior of the nanosheets are less prone to change the most probable O to bind the proton compared to the 3D system; just T3 and T6 varied. Meanwhile, the proton inclination to bind a different O atom in each Al-substituted T-site was more appreciable in sites exposed at the

external surface: six out of twelve distributions changed the relative order of the four O atoms from the bulk to the slab (see **Figure A-6**).

At the same time, the acid O-H stretching frequencies varied between 2953 and 3730 cm^{-1} (see **Table 3-3**). This broad range included the contributions of protons forming *intra-framework H-bonds* (i.e. H-bond O12-H \cdots O9 in **Figure 3-6e**) whose frequencies ranged from 2953 to 3364 cm^{-1} and *isolated* protons (without intra-framework H-bond interactions) between 3608 and 3730 cm^{-1} . **Figure A-7** shows a complete comparison of the 3D and 2D frequencies, where the main variations are derived from disruption/formation of intra-framework H-bonds (protons binding O7 and O10).

In addition, protons immersed in intra-framework H-bonds can be divided into *accessible* or *inaccessible* protons depending on whether they are able or not of interacting with molecules loaded in the main channels through any hindrance of the surrounding framework atoms. Meanwhile, all *isolated* protons are accessible from the pore system. **Table 3-3** lists a compilation of the above classification relating the type of proton with the O atom binding it.

First, *inaccessible* protons are bonded to O atoms O4, O9, O10, O12, O13 and O16 where H-bond formation can be established between the pairs (O9, O12) and (O13, O16) with O-H distances ranging from 1.000 to 1.014 Å and the O-H stretching frequency from 2953 to 3212 cm^{-1} (see **Table 3-3**). In the case of the slab, the protons bonded to O9 or O12 become exposed on the external surface and, due to the H-bond interaction O9(12)-H \cdots O12(9), the O-H bond is approximately parallel to this surface. Also, a new H-bond is established between O10 and O4 decreasing the O-H frequency from 3509 to 3364 cm^{-1} .

Accessible protons forming intra-framework H-bonds are bonded to O atoms O3, O6, O7, O14 and O19. H-bond interactions are formed for the pairs (O3, O6) in the sinusoidal channel, and (O7, O7) and (O14, O19) in the straight channel. The O-H distance varied between 0.976 and 1.004 Å and the O-H stretching frequencies ranged from 3147 to 3366 cm⁻¹. As a consequence of the formation of the 2D system, the H bound to O7 was no longer involved in an H-bond interaction and instead remained in the entry (or mouth) of the straight channel (its frequency increased from 3366 to 3708 cm⁻¹). Meanwhile, the H involved in the H-bond O3(6)–H···O6(3) along the sinusoidal channel became approximately parallel to the external surface in the 2D structure.

Finally, *isolated* protons (distances to their nearest neighbouring O atom remained above 2.41 Å, see **Table 3-3**) are bonded to O atoms O1, O2, O5, O8, O11, O15, O17, O18, O20, O21, O22, O23, O24, O25 and O26. For these H atoms the O-H distance changed between 0.975 and 0.982 Å and the stretching frequency from 3608 to 3730 cm⁻¹. Once the 2D structure is formed more than half of the O atoms available for *isolated* protons are at the mouth of the straight pores (see **Table 3-3**).

3.8 Projected Density of States

We have used the PDOS analysis to compare the differences in the electronic structure between the 3D and 2D systems. The 2p states of O atoms O24(-T12) and O12(-T8) were selected to measure the effects of the Al substitution in T sites exposed at the external surface of the slab. O24 is part of a silanol group and O12 remains part of the slab framework. **Figure 3-8** shows the zeolite segment where both O sites are located.

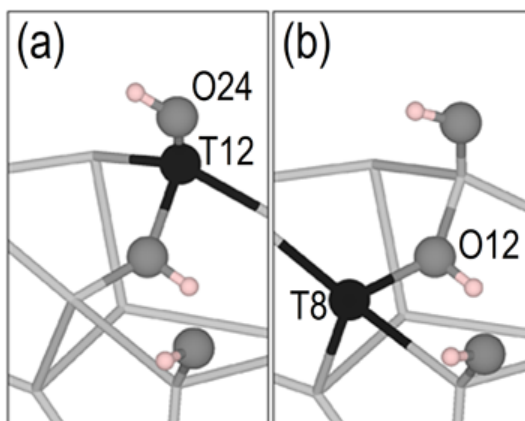


Figure 3-8. Local structure of the aluminium-substituted zeolite framework. (a) Aluminium substitution at the T12 site, the silanol oxygen atom O24 is labelled for reference within the text. (b) Aluminium substitution at the T8 site, the protonated oxygen atom O12 is labelled for reference within the text. Silanol oxygens and framework oxygens are represented with dark grey balls, the hydrogens with light pink balls and the aluminium with a black ball. The silicons are located at the interception of the light grey sticks.

Figure 3-9a shows the O(2p) PDOS for silanol O24 (bound to T12) within the pure-silica two-pentasil slab. Its most intense peak is located close to the Fermi energy (set at 0.0 eV), which overlaps with the occupied band edge of the total DOS (grey background). Also, the O24(2p) PDOS spreads over a wide range resembling each of the total DOS features. The Al substitution at site T12 (**Figure 3-9b**) shows the appearance of two narrow and intense peaks within 1.0 eV from the Fermi energy. In addition, the O(2p) PDOS for O24(-Al,T12) are much more localized (see **Figure 3-9b**), pointing to a weaker Al-OH_{surf} bond for the Al-substituted T12 silanol, which keeps the 2p states mainly confined in the O atom. This explains the much higher tendency of the Al-substituted silanol O atoms to form H-bonds with vicinal silanols (see **Figure 3-6** and related discussion).

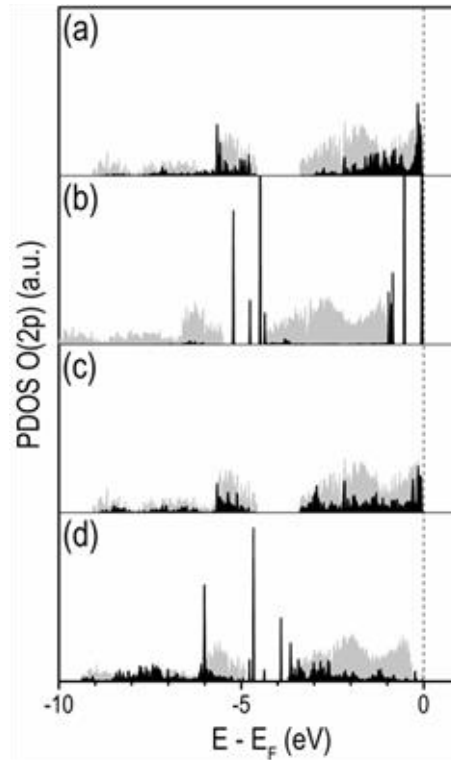


Figure 3-9. Projected density of states (PDOS) of the O(2p) states (black) and total DOS (grey, reduced 100 times with respect to O(2p) projections). (a) Silanol oxygen O24 in pure-silica slab. (b) Silanol oxygen O24 when the aluminium substitution takes place at the T12 site of the slab (see **Figure 3-8a**). (c) Framework oxygen O12 at the external surface of the pure-silica slab. (d) Protonated oxygen O12 when the aluminium substitution takes place at the T8 site of the slab (see **Figure 3-8b**). The Fermi energy (0.0 eV) is highlighted with a dotted line.

Meanwhile, the analysis of framework O atoms shows the opposite behaviour when one of its Si is replaced by Al. In the present case, O12 (bound to T8 and T12) was chosen to represent this feature. As for the pure-silica silanol O24, O12 has an intense peak just under the Fermi energy when there is no Al substitution (**Figure 3-9c**). However, once the Al is placed in T8 (**Figure 3-9d**) there is a depression in the PDOS close to the uppermost occupied edge as a result of the three-fold coordination (see **Figure 3-8b**). The O12 atom when protonated forms intra-framework H-bonds with O9 (see **Figure 3-6f**), although the results shown in **Figure 3-9c** and **Figure 3-9d** are applicable to O atoms without any possibility of H-bond interactions.

3.9 Chapter Conclusions

The catalytic performance of MFI depends on its composition and structure which may be as thin as a single unit cell length along the [010] direction. We have carried out a detailed analysis of the pristine and Al-doped two- and three- dimensional systems, using both IP and DFT calculations, where the Van der Waals correction was necessary for a precise reproduction of the experimental cell parameters and the bulk modulus of the zeolite. We have modelled two different slab thicknesses, and as shown before by other experimental and theoretical reports, the pure-silica MFI nanosheet structure does not change appreciably with respect to the 3D system. Once we have replaced the different T-sites by an Al atom, the same distortions were observed in the nanosheet framework as in the bulk structure.

The silanol groups are also affected by the Al substitution. When Al atoms were located at silanol positions, their tetrahedron distorted in such a way that allowed strong H-bond formations with vicinal silanol groups with a red shift of approximately 500 cm^{-1} of the O-H vibrational stretching frequency. The H-bond was always established between the silanol H atom and the Al-substituted silanol O atom; we never observed the inverse interaction. The O-H bond for Al-substituted silanol was slightly stronger than its Si counterpart, as shown by the vibrational analysis, which is a consequence of the weaker Al-OH interaction. Intra-framework H-bonds have an important role in the kinetic of the dehydration process of Al-substituted silanols; without them the energy barrier is around 10 kJ/mol, but when they are present it may increase to 20 kJ/mol. In all the studied configurations, the Al-substituted silanols were less stable than the system with one water molecule adsorbed on the Lewis centre, making the dehydration of Brønsted acids a natural

process at the external surface of the zeolite. The Lewis acid may be further stabilized by the formation of two-membered T-O rings with vicinal silanol groups.

The accessibility of protons as counter-ions for molecules loaded in the pore system can be classified according to the framework O atom binding them, (i) inaccessible protons, (ii) accessible protons forming H-bonds with vicinal framework O, and (iii) accessible protons without any kind of H-bond interaction. When the 3D structure is truncated, half of the O atoms binding accessible protons were located at the pore mouth; the rest were forming part of the silanol groups or intra-framework H-bonds. The only appreciable variations in the O-H stretching frequencies for protons as counter-ions, when the 3D-to-2D modification occurs, were associated with disruption/formation of intra-framework H-bonds.

Finally, the O(2p) PDOS analysis for framework O atoms revealed that the peak intensities close to the Fermi energy decrease when protonated due to the Al substitution. However, a different trend is obtained for the silanol hydroxy O when a silanol Si is substituted by Al. In this case, the density of states close to the Fermi energy shows narrower and more intense peaks, together with a shift to higher energies.

Chapter 4 Adsorption of Trimethylphosphine Oxide at the Internal and External Surfaces of Zeolite MFI

4.1. Introduction

Zeolites are well-known microporous materials whose frameworks are formed by corner-sharing SiO_4 tetrahedra. A negative charge is created when Al^{3+} substitutes Si^{4+} at the centre of a tetrahedron, which is compensated by extra-framework cations within the pore system of the zeolite. Brønsted acid (BA) sites are generated when the counterbalancing cation is a proton that covalently binds the O atom bridging the Al and the Si.[188] These BA sites, together with the size selectivity of the pore system, are the driving forces behind the wide range of catalytic applications of zeolites [29,189–191].

The characterization of the zeolite's acidity by number, density and strength may allow a direct correlation to its catalytic activity. However, in contrast with an acid in an aqueous medium, there is no unique way to rank the acidity of solid materials [192]. In zeolites, the proficiency of each BA as a proton donor will depend on its location within the pore system and its accessibility by the adsorbed reactant [192], which hinders the analysis of the zeolite's acidity.

The strength and number of the BA sites is usually measured through the adsorption of probe molecules, which act as bases and are protonated upon interaction with the BA sites. There are several analytical methods to evaluate the extent of the

protonation of the probe molecule [188,192], for example the nuclear magnetic resonance (NMR), which provides high accuracy and specificity to examine the consequences of the proton transfer [193]. The movement of the acid proton from the BA site to the probe molecule may be sensed directly when recording the ^1H NMR spectrum, as in the case of the pyridine/pyridinium system [194]. In addition, other nuclei different from ^1H may also be analysed if their magnetic response to the applied field is affected by the protonation of the probe molecule, e.g. ^{13}C in acetone [195] and ^{31}P in trimethylphosphine oxide [32]. In addition, these experimental results are complemented by computational calculations, which provide an interpretation of the NMR measurements at the atomic scale [196,197].

Trimethylphosphine oxide (TMPO, see **Figure 4-1** for a representation of the molecule's structure) has been shown to be a suitable molecule for sensing BA sites of different strength, owing to the high sensibility of the TMPO's ^{31}P nucleus to the intensity of the phosphine-BA interaction [193]. The ^{31}P chemical shift moves from 39 ppm (crystalline TMPO) towards a range of 50 - 105 ppm upon protonation of the TMPO's oxygen atom; the stronger the proton transfer the larger the chemical shift [193]. Therefore, the strength of BA sites in zeolites can be classified according to the value of the ^{31}P chemical shift as *very-strong* (90 – 80 ppm), *strong* (80 – 70 ppm) and *weak* (70 – 60 ppm), where 86 ppm is the calculated threshold of superacidity for TMPO [32,59,193,197].

The present thesis presents a Density Functional Theory (DFT) study of the adsorption of TMPO in zeolite MFI. Zeolite Socony Mobil-5 (ZSM-5) has the MFI framework type, which is a material with a wide array of industrial applications and high versatility [198–201]. We have described in detail the TMPO-BA interaction at the internal and external surfaces of zeolite MFI, providing atomic level information

to complement previous experimental reports. The MFI's internal and external surfaces behave differently: three types of BA sites of variable strength have been detected at the internal surface (*very-strong*, *strong* and *weak*), whereas the *strong* BA sites tend to disappear at the external surface [32,59]. Thus, to distinguish between these sites, alternative experimental methods must be used. For instance, silica chemical vapour deposition (Si-CVD) deactivates the external surface whilst keeping the internal sites undamaged [32], whereas the inclusion of tributylphosphine oxide (TBPO), which is too big to diffuse into the zeolite's pore system, allows the exclusive sensing of the external surface [32,59].

We have also explored how a variable number of TMPO molecules affects the acid response of the BA site. Zheng et al. have previously reported the enhancement of the Brønsted acidity in mordenite by the *intermolecular solvent effect* when several TMPO molecules are confined in the micropore [202]. The authors relate this effect to Van der Waals interactions among the TMPO molecules, which provoke a simultaneous increase and decrease of the O-H distances of the TMPO molecules, generating in consequence *superacidity* and *weak* acidity, respectively [192,193,202].

4.2 Computational Methods

The results presented in this thesis were obtained using the DFT approximation as implemented in the *Vienna Ab-initio Simulation Package* (VASP) [82–85]. The generalized gradient approximation (GGA) under the scheme proposed by Perdew, Burke and Ernzerhof (PBE) was used in all calculations [100]. Grimme's method of the sum of pairs was added to the GGA energy to account for the long range-

interactions (DFT-D2) [124]. The inclusion of dispersion corrections improves the predicted cell parameters and elastic properties of the zeolite MFI [203]. The valence electrons were treated explicitly using a basis set of plane waves, although their nodal features and interactions with the ion were included within the projected-augmented-wave method (PAW) [113,114]. The number of electronic states considered during the calculations was determined by a maximum kinetic energy for the plane waves of 500 eV. The electronic convergence was improved using the Gaussian smearing method with a band width of 0.1 eV for the zeolite and zeolite-TMPO systems and 0.01 eV for the isolated TMPO molecule [204,205]. Only the Gamma point was considered during the numerical integration over the Brillouin zone due to the large dimensions of the MFI unit cell. Finally, the electronic threshold was set to 10^{-5} eV.

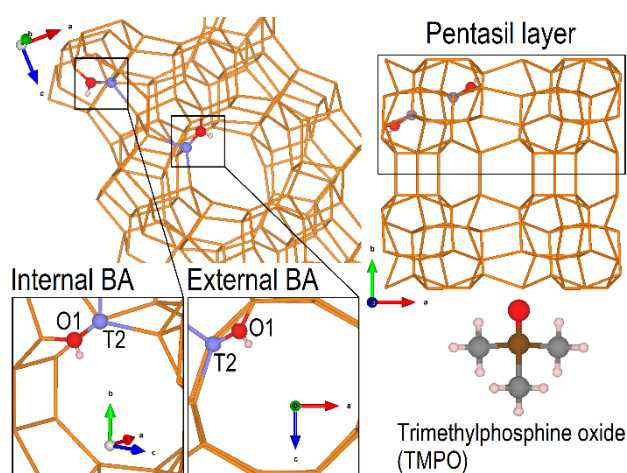


Figure 4-1. Representation of the BA sites at the internal (bottom, left panel) and at the external (bottom, right panel) surfaces. One of the two pentasil layers that form the slab is identified by a black-line rectangle (top, right panel). The Al-substituted T2-site (light blue ball) with the proton (white ball) at the O1 position (red ball) are shown. The rest of the O atoms and silanol OH groups were deleted for a better view; Si atoms are represented by orange sticks. A molecule of trimethylphosphine oxide is shown in the bottom-right corner; H is represented in white, C in grey, P in brown and O in red.

The orthorhombic unit cell of the MFI framework has twelve non-equivalent T-sites to be substituted by Al (the centre of each tetrahedron is referred as T-site and numbered according to the symmetry of the zeolite's unit cell). In conjunction, the acid proton can bind four O atoms for each T-site, which produces a high number of possible combinations, making it practically impossible to carry out a detailed analysis of each arrangement. We have therefore opted for Al substitution in the T2 site, binding the proton to O1 (see **Figure 4-1**), which allowed us to focus on the acid response of that BA site to the number and orientation of TMPO molecules, as well as any consequences of the BA site location at the internal or the external surface.

The T2 site was chosen for the Al substitution, and the charge-compensating proton was bound to the O1 atom, leading to the formation of the BA site (see **Figure 4-1**). This specific position was chosen because T2 is at the interception of straight and sinusoidal channels, and is easily accessible by the probe molecule, allowing a fair study of the TMPO agglomeration around the acid site. We have studied the proton transfer to TMPO, accommodating up to three molecules simultaneously. The optimized cell parameters of the zeolite MFI were 20.317, 19.979 and 13.413 Å along the *a*, *b* and *c* directions respectively [203], within 1% of the experimental measurements [171]. Using periodic boundary conditions, the external surface was described by a slab formed of two pentasil layers [147], as shown in **Figure 4-1**, with a surface area per unit cell of 272.512 Å² and a perpendicular vacuum gap of 20 Å between the slabs. In this termination, each dangling Si-O bond was properly saturated by hydroxyl, thus forming silanol groups at the bottom and top surfaces of the slab; in the case of pentasil layers, there is only one dangling Si-O bond per Si atom [203]. The isolated TMPO molecule was first optimized in a 20x21x22 Å³ cell,

before it was loaded in the zeolite, varying its numbers and orientations, ahead of a full geometry optimization.

The initial geometries set for optimization were constructed by loading the TMPO molecules in close proximity to the acid proton of the zeolite (at 2.0 to 3.0 Å). These geometries were locally optimized using a conjugate gradient algorithm until all forces acting on the ions were smaller than 0.03 eV/Å. The local relaxations were followed by short quantum molecular dynamics (MD) simulations over a simulation time of 10 ps, with a time step of 0.5 fs. A micro-canonical ensemble was used for each geometry during the first 2.5 ps of MD whilst keeping the temperature at 300 K. A canonical ensemble centred at 300 K was simulated during the next 7.5 ps of MD, controlling the temperature fluctuation with a Nosé thermostat [129,130,206]. We have used the last 2.5 ps to obtain the average structural parameters of interest.

All the images related to structural and charge density visualizations were obtained with the code *Visualization for Electronic and Structural Analysis* (VESTA 3) [168].

4.2.1 Classification of the Acid Strength

Brønsted acid sites of different strength are detected in zeolite MFI when probed with TMPO. According to Seo *et al.*, the acid strength can be classified as *very-strong* (86 ppm), *strong* (76 ppm) and *weak* (68 and 66 ppm), [59] in agreement with previous experimental reports [32]. Zheng *et al.* reproduced the range of ^{31}P chemical shifts by modelling the adsorption of TMPO on zeolite MFI, which was represented by a cluster of eight T-sites [197]. The authors tuned the acid strength by varying the terminal Si-H distances of the cluster, thus controlling the extent of the proton transfer from the BA site to the TMPO's oxygen atom, hereafter referred

to as $O_{(P)}$. Zheng *et al.* reported a wide spectrum of $O_{(P)}$ -H distances after optimization, calculating the ^{31}P chemical shift for each geometry; those distances ranged from 1.368 (45.5 ppm) to 1.014 Å (88.9 ppm) [197].

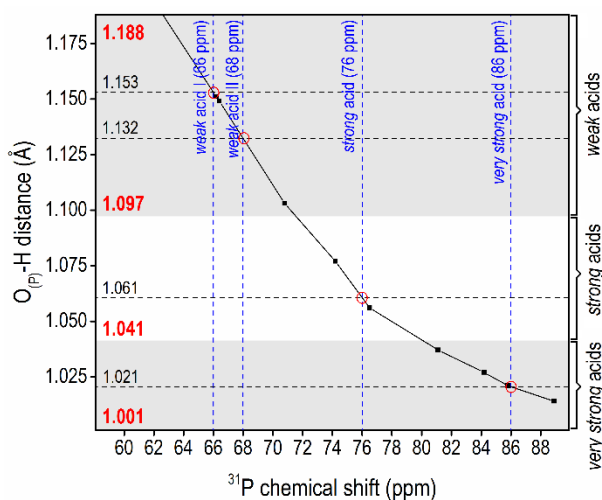


Figure 4-2. Correlation of the $O_{(P)}$ -H distances and the ^{31}P chemical shifts using Zheng *et al.* data (black squares linked with black lines) [197]. The experimental classification of the acid sites of the zeolite MFI according to the TMPO ^{31}P chemical shift is indicated by vertical dashed blue lines [32,59]. The experimental classification is used to extrapolate the expected $O_{(P)}$ -H distances from its interception with the theoretical curve (indicated by red circles); the corresponding distance values are written above the horizontal dashed black lines. The spectrum of $O_{(P)}$ -H distances is divided into three zones taking the middle points between the extrapolated $O_{(P)}$ -H distances. These zones are shaded alternately in light grey and white, corresponding to (top) *weak acids*, (centre) *strong acids*, and (bottom) *very-strong acids*; the limits of each range are indicated by the red numbers at the left-hand side of the graph.

We noted that our calculated $O_{(P)}$ -H distances changed within the limits proposed by Zheng *et al.*, and hence we assumed that the theoretical work in Ref [197] matches the expected ^{31}P chemical shift for our own data. **Figure 4-2** shows the correlation of the $O_{(P)}$ -H distance as a function of the ^{31}P chemical shift as calculated by Ref [197]. From that curve, we extrapolated the $O_{(P)}$ -H distances corresponding to the experimental measurement of the ^{31}P chemical shift that classifies the BA sites by strength (see **Figure 4-2**) [59]. Taking the middle points between the extrapolated

$O_{(P)}$ -H distances, we obtained approximate ranges of $O_{(P)}$ -H distances to classify the effective acid strength of our model (see **Figure 4-2**). The ranges are as follows: *very-strong* acid (from 1.001 to 1.041 Å), *strong* acid (from 1.041 to 1.097 Å) and *weak* acid (from 1.097 to 1.188 Å). In comparison, we calculated a $O_{(P)}$ -H distance of 0.978 Å for a fully-protonated TMPO molecule loaded in the zeolite, for which the position of the P atom was fixed at the centre of the pore interception of zeolite MFI to avoid any H-bonding with nearby framework O atoms. In addition, based on Car-Parrinello molecular dynamics of a hydronium ion in aqueous medium, Tuckerman *et al.* have reported an O-H distance of 1.3 Å for the shared proton between two H₂O molecules in the complex (H₃O₂)⁺ [207].

4.3 Adsorption of one TMPO Molecule

In this section, we have presented the adsorption of a single TMPO molecule in close proximity to the BA proton. The TMPO was adsorbed on the internal and external surfaces of the zeolite by placing the $O_{(P)}$ atom at 2.0 Å from the acidic proton. Two different orientations of the TMPO molecule with respect to the BA proton were tested, varying the values of the P- $O_{(P)}$ -H and $O_{(P)}$ -H- $O1_{(Al)}$ angles (the label $O1_{(Al)}$ refers to the framework O atom binding simultaneously the Al atom and the acidic proton; in the present case, position O1).

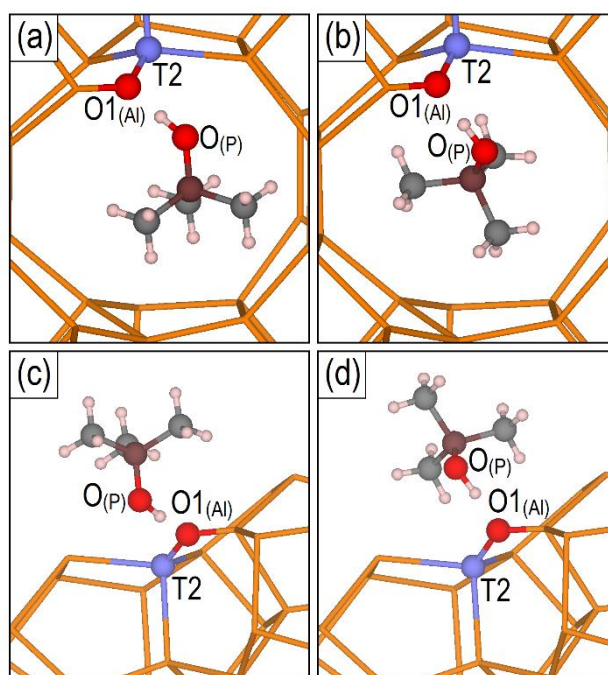


Figure 4-3. Representation of the interaction of a single TMPO molecule with (a, b) the internal, and (c, d) the external BA sites after local optimization; H in white, C in grey, P in brown, O in red, Al in light blue and Si represented by orange sticks. All the framework O atoms (except the protonated one), and silanol OH groups were deleted for an enhanced view. Related structural values are presented in **Table 4-1**.

Table 4-1. Relevant interatomic distances (Å) of the 1TMPO/1BA configurations shown in **Figure 4-3** (a to d) after local optimization.

	Internal BA		External BA	
	Figure 4-3a ^a	Figure 4-3b	Figure 4-3c	Figure 4-3d
O_(P)-H	1.060 (2.000)	1.045 (2.000)	1.066 (2.000)	1.060 (2.000)
O_(Al)-H	1.459 (0.975)	1.483 (0.975)	1.429 (0.975)	1.465 (0.975)
O_(P)-O_(Al)	2.518 (2.975)	2.526 (2.225)	2.492 (2.975)	2.522 (2.225)
P-O_(P) ^b	1.556	1.561	1.556	1.556

^a The values before the structural optimization are presented within parentheses.

^b The optimized P-O_(P) distance in gas phase is 1.494 Å.

During the local relaxations, the proton was transferred from the BA site to the TMPO molecule, at both the internal and external surfaces, regardless of the initial configuration. The Bader analysis of atomic charges [208–210] confirmed the movement of the proton; the total charge obtained for protonated phosphine oxides ranged from + 0.8 to 0.9 e⁻, and more than 80 % of corresponding negative charge left in the zeolite framework was associated with the AlO₄ tetrahedron. **Figure 4-3**

shows the final equilibrium structures with the corresponding structural parameters listed in **Table 4-1**. The O_(P)-H bond length ranged from 1.045 to 1.066 Å, i.e. larger than those of the MFI external silanols groups (< 0.970 Å), and MFI acidic protons with intra-framework H-bonds (< 1.014 Å) [203]. These longer bonds were due to strong H-bonds established between the protonated TMPO molecules and the O_(Al) atoms of the framework, with O_(P)-O_(Al) distances below 2.6 Å and H-O_(Al)-O_(P) angles smaller than 3° [211]. According to the division of the spectrum of possible O_(P)-H distances, shown in **Figure 4-2**, the acid strength of the BA site may be classified as *strong* for the four different configurations after local optimization. No evidence of *very-strong* or *weak* acidity was obtained at this stage. The variation of the adsorption energy could not be correlated with corresponding changes in the O_(P)-H distance. Nonetheless, the average TMPO interaction energy was larger for the internal BA when compared with the external BA: -190 and -167 kJ/mol, respectively. The contribution of dispersion forces to the total adsorption energy was 47% and 38%, for the internal and external BA site, respectively. However, these percentages should be viewed with reservation, because the DFT-D2 method tends to overestimate attractive interactions owing to the omission of terms above the two-body contribution; the error can increase beyond 10 % for supramolecular complexes [120].

Table 4-2. Relevant interatomic distances (Å) after 10 ps of MD simulation taking the 1TMPO/1BA configurations shown in **Figure 4-3 (a to d)** as input geometries.

	Internal BA		External BA	
	Figure 4-3a ^a	Figure 4-3b	Figure 4-3c	Figure 4-3d
O_(P)-H	1.06 ± 0.05	1.05 ± 0.05	1.08 ± 0.08	1.07 ± 0.06
O_(Al)-H	1.5 ± 0.1	1.6 ± 0.2	1.5 ± 0.1	1.5 ± 0.1
O_(P)-O_(Al)	2.51 ± 0.09	2.6 ± 0.1	2.53 ± 0.09	2.53 ± 0.09
P-O_(P)	1.56 ± 0.03	1.57 ± 0.03	1.57 ± 0.04	1.57 ± 0.03

^a Average and standard deviation over the last 2.5 ps of MD simulation.

The MD simulation did not result in significant changes when compared to the local optimization; **Table 4-2** shows the average values and the standard deviations of the last 2.5 ps. The average values of the $O_{(P)}-H$ bond length remained within the range 1.05 to 1.08 Å, with fluctuations between 0.05 and 0.08 Å, which confirms that the strength of the modelled BA site can only be classified as *strong* when a single TMPO is adsorbed. Furthermore, we observed the replacement of $O1_{(Al)}$ by $O2_{(Al)}$ as the acceptor of the H-bond for the configuration in **Figure 4-3b** (see **Figure 4-4** for a representation of the structure after 10 ps of MD). This movement occurred during the first 2.5 ps of MD simulation, although the acid response continued to be *strong*.

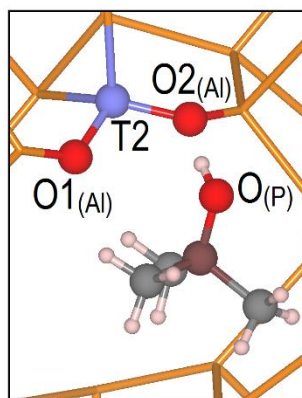


Figure 4-4. Configuration after 10 ps of MD simulation of the locally optimized structure in **Figure 4-3b**.

4.4 Adsorption of two TMPO Molecules

We next adsorbed two TMPO molecules at a short distance from the BA site to analyse their effect on the proton transfer. **Figure 4-5** shows the most stable structures after local optimization, out of several tested configurations at the internal and external BA sites; related structural parameters are compiled in **Table 4-3**. The $O_{(P)}-H$ bond length of the configurations in **Figure 4-5** decreased to 1.016 and 1.033

Å, for the internal and external surfaces, respectively, suggesting an apparent stronger acidity triggered by the presence of the second TMPO molecule. In consequence, the acid strength of the internal and external acid sites can be classified as *very-strong* according to the scheme in **Figure 4-2**.

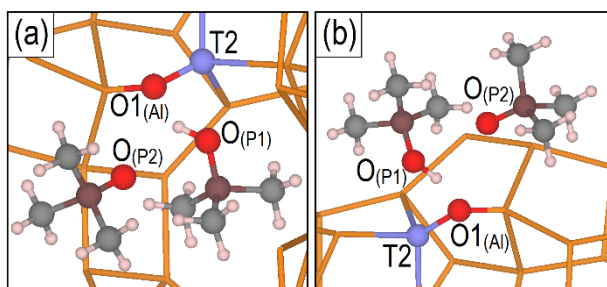


Figure 4-5. Representation of the adsorption of two TMPO molecules on (a) the internal and (b) the external BA sites after local optimization. H in white, C in grey, P in brown, O in red, Al in light blue and Si represented by orange sticks. All the framework O atoms (except the protonated one), and silanol OH groups were deleted for an enhanced view. Related structural values are presented in **Table 4-3**.

We have calculated average adsorption energies per TMPO of -125 kJ/mol for the internal surface and -112 kJ/mol for the external surface, with the dispersion forces representing 84% and 54% of the total adsorption energy, respectively, indicating that the role of van der Waals interactions increases with the number of probe molecules.

Table 4-3. Relevant interatomic distances (Å) of the 2TMPO/1BA configurations shown in **Figure 4-5 (a, b)** after local optimization.

	Internal BA Figure 4-5a ^a	External BA Figure 4-5b
O _(P1) -H	1.016 (2.000)	1.033 (2.000)
O _(P2) -H	2.406 (2.000)	2.746 (2.000)
O _(P1) -O _(P2)	2.868 (2.462)	2.908 (2.462)
O _(Al) -H	1.635 (0.975)	1.541 (0.975)
O _(P1) -O _(Al)	2.547 (2.372)	2.544 (2.372)
P-O _(P1)	1.561	1.555
P-O _(P2)	1.504	1.499

^a The values before the structural optimization are presented within parentheses.

The second TMPO is a source of steric hindrance that affects the interaction through H-bonding between the first TMPO and the BA site. Because the protonated TMPO cannot form an ideal orientation in front of the bridging O atom, the H-bond is not strong enough, which produces a further shift of the proton position towards $O_{(P1)}$. We did not observe any evidence that the second TMPO interfered through direct competition for the proton: the $O_{(P2)}$ -H distance increased above 2.5 \AA during local optimization, which diminishes the possibility of H-bonding.

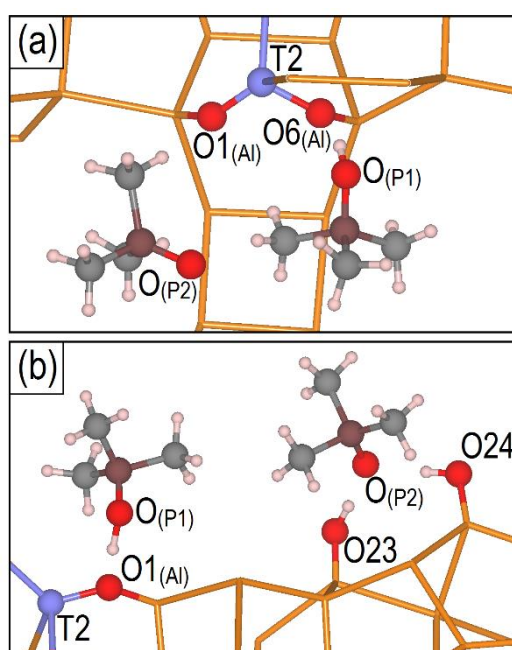


Figure 4-6. Representation of two TMPO molecules on (a) the internal BA site and (b) the external BA site after 10 ps of MD simulation of the locally optimized structure in **Figure 4-5**.

In contrast to the adsorption of a single TMPO molecule, where only *strong* acids are observed after both local optimization and MD, the systems composed of two TMPO molecules continued evolving during the MD simulation, modifying the acid strength classification given by the local optimization. At the internal surface, the movement of the TMPO molecules is capped owing to the reduced space inside the pore system. Therefore, we noticed a small shift of the protonated TMPO from $O1_{(AI)}$

to $O_{6(AI)}$, which was still enough to increase the separation from the second TMPO and establish a strong H-bond with $O_{6(AI)}$ (see **Figure 4-6a** and **Table 4-4**). As a consequence, the average $O_{(P1)}$ -H bond length increased to 1.05 Å after 10 ps of MD, from an initial value of 1.016 Å. The absence of confinement effects at the external surface allowed greater movement of the second TMPO, moving away from the first TMPO, to finally establish two strong H-bonds with nearby silanol groups (see **Figure 4-6b**). The withdrawal of the second TMPO from the vicinity of the protonated phosphine reduced the steric effects, and hence enabled the reorientation of the first TMPO. Without steric interference, the acid proton could be better shared between the bridging $O_{1(AI)}$ and $O_{(P1)}$, which increased the $O_{(P1)}$ -H bond length from 1.033 Å after local optimization to an average value of 1.07 Å after 10 ps of MD. Therefore, the *very-strong* acidity predicted by the local relaxation was not conserved during the MD simulation; the BA site behaved as a *strong* acid instead.

Table 4-4. Relevant interatomic distances (Å) after 10 ps of MD simulation taking the 2TMPO/1BA configurations shown in **Figure 4-5 (a, b)** as input geometries.

	Internal BA Figure 4-5a ^a	External BA Figure 4-5b
$O_{(P1)}$ -H	1.05 ± 0.04	1.07 ± 0.06
$O_{(P2)}$ -H	5.0 ± 0.3	8.7 ± 0.2
$O_{(P1)}$ - $O_{(P2)}$	4.7 ± 0.4	8.7 ± 0.2
$O_{(AI)}$ -H	1.5 ± 0.1	1.5 ± 0.1
$O_{(P1)}$ - $O_{(AI)}$	2.52 ± 0.09	2.5 ± 0.1
P- $O_{(P1)}$	1.57 ± 0.03	1.56 ± 0.02
P- $O_{(P2)}$	1.51 ± 0.02	1.52 ± 0.01

^a Average and standard deviation over the last 2.5 ps of simulation.

4.5 Adsorption of three TMPO Molecules

Proton transfer can be classified as *weak* for $O_{(P)}$ -H distances that range from 1.097 to 1.188 Å (see **Figure 4-2**). We observed this *weak* acidity when a direct $O_{(P)}$ -Al

interaction was induced after adding a third phosphine oxide into the 2TMPO/1BA systems shown in **Figure 4-5**.

Figure 4-7 shows two equivalent structures after local optimization, out of several tested during our work, where $O_{(P1)}-H$ bond lengths of 1.131 and 1.154 Å were obtained after adsorption on the internal and external surfaces, respectively; structural parameters of interest are compiled in **Table 4-5**. The proton was almost evenly shared between $O_{(Al)}$ and $O_{(P1)}$, rendering the acid response of the BA site as *weak*. On this occasion, the average interaction energies for the internal and external BA sites differed by only 2 kJ/mol, -99 (internal) versus -97 (external) kJ/mol. The adsorption at the internal surface, without considering the correction for dispersion forces, was repulsive, by 12 kJ/mol on average. Once the Van der Waals interactions were taken into consideration the overall adsorption energy became attractive, with a value of -99 kJ/mol. At the external surface, the dispersion contribution represented 77% of an average adsorption energy of -97 kJ/mol.

Our interpretation of the weakening of the acid as proton donor after the adsorption of three TMPO molecules was based on the strengthening of the $O_{(Al)}-H$ bond. The $O_{(Al)}-Al$ bond is weakened by the interaction between the Al atom and one of the non-protonated TMPO molecules, which is reflected in $O_{(P)}-Al$ distances that remained around 2.0 Å for both surfaces, as shown in **Figure 4-7** and **Table 4-5**. There was also a large displacement of the Al atom during the optimization toward the non-protonated phosphine. Under conditions of significant agglomeration of TMPO molecules around the BA site, the Al center may show residual Lewis acidity, with subsequent repercussions on the acid strength of the BA site. We did not observe direct competition for the acid proton by the non-protonated phosphines, emphasized by $O_{(P2)}-H$ and $O_{(P3)}-H$ distances above 2.8 Å after local optimization.

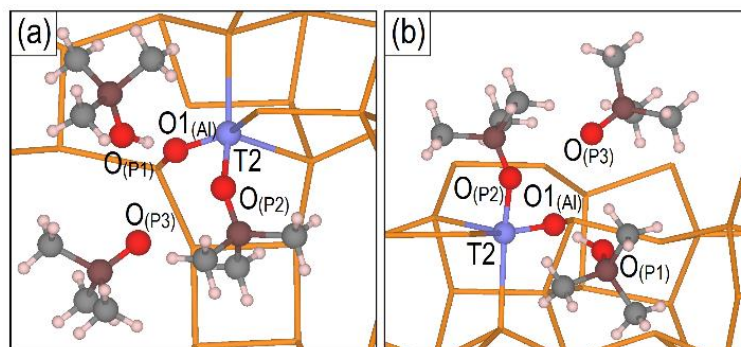


Figure 4-7. Representation of the adsorption of three TMPO molecules on (a) the internal and (b) the external BA sites after local optimization. H in white, C in grey, P in brown, O in red, Al in light blue and Si represented by orange sticks. All the framework O atoms (except the protonated one), and silanol OH groups were deleted for an enhanced view. The interaction between one of the non-protonated TMPO and the Al atom is represented by a stick connecting O_(P2) to the Al atom. Related structural values are presented in **Table 4-5**.

Table 4-5. Relevant interatomic distances (Å) of the 3TMPO/1BA configurations shown in **Figure 4-7 (a, b)** after local optimization.

	Internal BA Figure 4-7a ^a	External BA Figure 4-7b
O _(P1) -H	1.131 (2.000)	1.154 (2.000)
O _(P2) -H	2.878 (2.000)	3.134 (2.000)
O _(P3) -H	3.125 (2.000)	3.599 (2.000)
O _(P1) - O _(P2)	3.548 (3.570)	4.034 (3.572)
O _(P1) - O _(P3)	3.473 (3.230)	4.144 (3.227)
O _(P2) -Al	1.993 (3.080)	2.033 (3.073)
O _(Al) -H	1.250 (0.975)	1.232 (0.975)
O _(P1) -O _(Al)	2.381 (2.627)	2.379 (2.627)
P-O _(P1)	1.533	1.531
P-O _(P2)	1.511	1.511
P-O _(P3)	1.501	1.496

^a The values before the structural optimization are presented within parentheses.

In order to observe the perturbation and reordering of the electronic charge density derived from the TMPO-Al interaction, we have calculated the charge density difference for the configurations shown in **Figure 4-7** according to the equation:

$$\Delta\rho = \rho_{zeolite+3TMPO} - \rho_{zeolite+2TMPO} - \rho_{1TMPO} \quad (4-1)$$

The $\rho_{zeolite+3TMPO}$ term corresponds to the electronic density of the whole system with three TMPO molecules, while the density of the zeolite without the TMPO molecule closest to the Al atom is represented by the $\rho_{zeolite+2TMPO}$ term. The electronic density of the isolated phosphine oxide with exactly the same structure as when it is interacting with Al atom, is denoted by the ρ_{1TMPO} term. We have used the same grid of points to represent the charge density, and the same box size for the three calculations. The resulting distribution shows an increase of the charge density between O_(P2) and Al atoms (see **Figure 4-8**), which highlights the formation of bonding interactions between both centres.

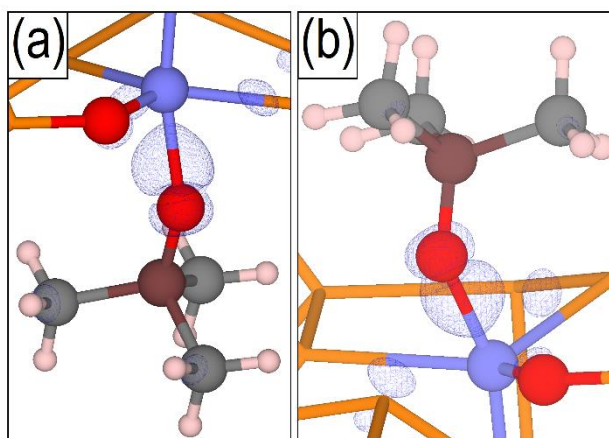


Figure 4-8. Charge difference isosurfaces with values of 0.005 bohr^{-3} calculated from (4-1). (a) Internal BA site, (b) external BA site. The structures correspond to those shown in **Figure 4-7**. H in white, C in grey, P in brown, O in red, Al in light blue and Si represented by orange sticks. All the framework O atoms (except the protonated one), and silanol OH groups were deleted for an enhanced view.

Figure 4-9 shows the projected density of states (PDOS) onto O_(P2)(2p) of the TMPO interacting with the Al atom, as represented in **Figure 4-7a**, corresponding to the interior of the zeolite. The O_(P2)(2p) PDOS presents intense peaks at the upper occupied edge of the energy spectra, between -2 and 0.0 eV (see **Figure 4-9a**). These O_(P)(2p) states are complemented by small peaks in the Al(3s,3p) PDOS (**Figure 4-9b** and **9c**) which disappear once the TMPO-Al interaction is deleted by removing

the phosphine molecule (**Figure 4-9d** and **9e**). In addition, the Al(3s,3p) PDOS reports the appearance of empty states above the Fermi energy as a result of the phosphine removal (**Figure 4-9d** and **9e**). These transformations emphasize electron donation from the TMPO into empty electronic states associated with the Al atom.

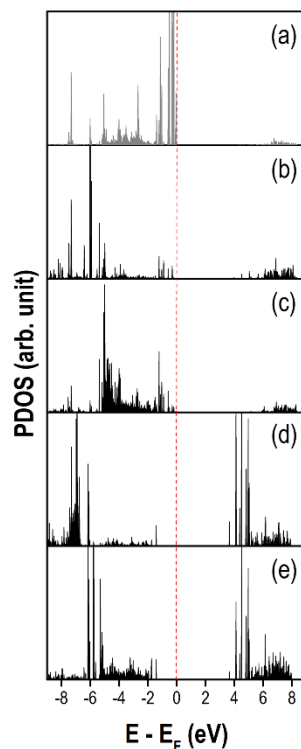


Figure 4-9. Projected density of states (PDOS) of (a) $O_{(P2)}(2p)$, (b) Al(3s) and (c) Al(3p) for the 3TMPO/1BA configuration observed in the cavity according to **Figure 4-7a**. PDOS of (d) Al(3s) and (e) Al(3p) for the structure without the non-protonated TMPO that interacts with the Al centre.

After local optimization, there were differences in the behaviour of the internal and external BA sites in the presence of three TMPO molecules. The internal ones always performed as *weak* acids, whereas the external BA sites varied in strength between *strong* and *weak*, depending on the configuration; **Table 4-6** summarizes these tendencies. When the $O_{(P2)}$ atom remained at less than 2.15 Å from the Al, the proton transfer was *weak*. Once this distance increased and the non-protonated TMPO moved away from the Al atom, which was the case in four out of six

configurations considered for the external BA site, the acidity was classified as *strong*. These findings underline the importance of the TMPO-Al interaction for the presence of the *weak* acidity.

Table 4-6. Relevant interatomic distances (Å) for six different configurations 3TMPO/1BA after local optimization.

Internal BA configurations^a				
	O_(P2)-Al	O_(Al)-Al	O_(P1)-H	Acid class.^c
a	2.099	1.853	1.146	<i>weak</i>
b^b	1.993	1.846	1.131	<i>weak</i>
c	2.149	1.839	1.107	<i>weak</i>
d	1.988	1.852	1.137	<i>weak</i>
e	2.245	1.822	1.093	<i>strong</i>
f	2.002	1.844	1.116	<i>weak</i>
External BA configurations^a				
	O_(P2)-Al	O_(Al)-Al	O_(P1)-H	Acid class.^c
a	3.050	1.793	1.050	<i>strong</i>
b^b	2.033	1.842	1.154	<i>weak</i>
c	5.554	1.812	1.053	<i>strong</i>
d	3.637	1.785	1.059	<i>strong</i>
e	3.059	1.789	1.047	<i>strong</i>
f	2.059	1.829	1.100	<i>weak</i>

^a Second column: distance between O_(P2) and Al in **Figure 4-7**. Third column: distance between O_(Al) and Al. Fourth column: O_(P1)-H distance for the protonated TMPO in **Figure 4-7**.

^b Configurations shown in **Figure 4-7**

^c Acid classification according to **Figure 4-2**.

The locally optimized arrangements of three TMPO molecules evolved differently during the MD simulation, depending on whether the adsorption took place at the internal or external surface. The MD calculations were performed on the configurations shown in **Figure 4-7**, with the average of the main structural parameters compiled in **Table 4-7**. The internal BA site continued to behave as a *weak* acid after 10 ps of dynamics, mostly due to the conservation of the initial configuration given as an input, with O_(P2) atom binding the Al centre. However, at the external surface the agglomeration of three TMPO molecules at the acid site was not preserved; both non-protonated TMPO molecules moved away towards nearby silanol groups to establish H-bonds. Once the O_(P2)-Al link was broken, the acid

strength of the external BA was once more *strong*, illustrated by an average $O_{(P1)}-H$ bond length of 1.05 Å. This exemplifies how equivalent BA sites are driven to behave differently as a consequence of the confinement produced by the pore system. The same confinement may be mimicked at the external surface if a large enough number of TMPO molecules is adsorbed in the vicinity of the BA site, limiting the movement of those phosphines that are in direct contact with the acid.

Table 4-7. Relevant interatomic distances (Å) after 10 ps of MD simulation taking the 3TMPO/1BA configurations shown in **Figure 4-7 (a, b)** as input geometries.

	Internal BA	External BA
	Figure 4-7a^a	Figure 4-7b
$O_{(P1)}-H$	1.2 ± 0.1	1.05 ± 0.05
$O_{(P2)}-H$	3.7 ± 0.2	6.5 ± 0.3
$O_{(P3)}-H$	5.6 ± 0.5	8.8 ± 0.5
$O_{(P1)}-O_{(P2)}$	4.9 ± 0.2	6.6 ± 0.3
$O_{(P1)}-O_{(P3)}$	6.3 ± 0.5	9.5 ± 0.5
$O_{(P2)}-Al$	2.0 ± 0.1	6.3 ± 0.2
$O_{(Al)}-H$	1.3 ± 0.2	1.5 ± 0.1
$O_{(P1)}-O_{(Al)}$	2.46 ± 0.09	2.52 ± 0.09
$P-O_{(P1)}$	1.55 ± 0.03	1.56 ± 0.02
$P-O_{(P2)}$	1.52 ± 0.02	1.53 ± 0.02
$P-O_{(P3)}$	1.50 ± 0.02	1.51 ± 0.03

^a Average and standard deviation over the last 2.5 ps of simulation.

4.6 Full Deprotonation of the Brønsted Acid Site

We have considered the migration of a protonated TMPO from the vicinity of the BA site by moving the phosphine to the second pore interception that is present within the MFI unit cell. The distance between the acid proton and any of the four O atoms binding the Al centre was larger than 5 Å before relaxation, rendering the acid site fully deprotonated. After local optimization, the $O_{(P)}-H$ bond length decreased to 0.979 and 1.005 Å for adsorption at the internal and the external surfaces, respectively; **Figure 4-10** shows the optimized geometries, with the O-H

distances compiled in **Table 4-8**. Those bond lengths correspond to ^{31}P chemical shifts of around 86 ppm, which translates into an acid classification of *very-strong* (see **Figure 4-2**). The framework O atoms that do not bind the Al centre are not basic enough to lengthen the $\text{O}_{(\text{P})}\text{-H}$ bond length, even if a H-bond is established. The MD simulation did not result in further modifications, with average $\text{O}_{(\text{P})}\text{-H}$ bond lengths remaining around 1.00 Å (see **Table 4-8**).

We also placed a second TMPO molecule in close proximity to the protonated phosphine in order to form the species $(\text{TMPO})_2\text{H}^+$, and thus to induce the sharing of the acid proton between both molecules. After local optimization, the $\text{O}_{(\text{P}1)}\text{-H}$ bond length at the interior of the zeolite remained 0.996 Å, corresponding to a *very-strong* protonation. The equivalent value at the external surface increased to 1.072 Å, but still within the range of $\text{O}_{(\text{P})}\text{-H}$ distances sensed as a *strong* protonation by ^{31}P NMR. The second TMPO molecule had $\text{O}_{(\text{P}2)}\text{-H}$ distances of 2.167 and 1.431 Å for the internal and external surfaces, respectively.

During the MD simulation, the proton became more evenly shared between both TMPO molecules, increasing the average $\text{O}_{(\text{P}1)}\text{-H}$ bond length to 1.1 or 1.2 Å, and decreasing the $\text{O}_{(\text{P}2)}\text{-H}$ distance to 1.4 or 1.3 Å depending on the surface (see **Table 4-8**); those values correspond to ^{31}P chemical shifts that classify the acid strength as *weak*. Therefore, full proton transfer may be probed experimentally as either *very-strong* or *weak*, depending on whether the proton is binding a single TMPO or is shared between two phosphine molecules, respectively. During the adsorption of TMPO on Keggin-type 12-tungstophosphoric acid (HPW) [212], TMPOH^+ species appear within the region 95 – 85 ppm, whilst the formation of $(\text{TMPO})_2\text{H}^+$ moves the ^{31}P chemical shift into the range 75 – 53 ppm, in agreement with our calculated $\text{O}_{(\text{P})}\text{-H}$ distances. However, the signals associated with $(\text{TMPO})_2\text{H}^+$ disappear after

thermal pre-treatment of the sample, to emerge again when the sample is oversaturated with TMPO molecules [212]. Extrapolating to the zeolite MFI, it is more probable that the formation of $(\text{TMPO})_2\text{H}^+$ occurs at the external surface, where the acid sites are exposed to higher loads of TMPO molecules than at the internal surface.

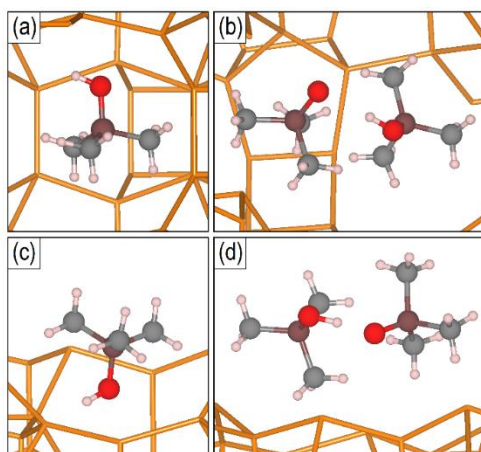


Figure 4-10. Representation of (a, c) TMPOH^+ and (b, d) $(\text{TMPO})_2\text{H}^+$ at more than 5 Å away from the BA site after local optimization. (a, b) Internal surface, (c, d) external surface. H in white, C in grey, P in brown, O in red and Si represented by orange sticks. All the framework O atoms (except the protonated one), and silanol OH groups were deleted for an enhanced view. Related structural values are presented in **Table 4-8**.

Table 4-8. Relevant interatomic distances (Å) of the full protonated TMPO molecules at more than 5 Å from the BA site.

	Internal BA		External BA	
	TMPOH^+ Figure 4-10a	$(\text{TMPO})_2\text{H}^+$ Figure 4-10b	TMPOH^+ Figure 4-10c	$(\text{TMPO})_2\text{H}^+$ Figure 4-10d
	Local optimization^a			
$\text{O}_{(\text{P1})}\text{-H}$	0.979	0.996	1.005	1.072
$\text{O}_{(\text{P2})}\text{-H}$	-	2.167	-	1.431
$\text{P-O}_{(\text{P1})}$	1.594	1.600	1.576	1.570
$\text{P-O}_{(\text{P2})}$	-	1.515	-	1.522
$\text{O}_{(\text{Si})}\text{-H}$	2.802	-	1.708	-
	MD simulation^b			
$\text{O}_{(\text{P1})}\text{-H}$	1.00 ± 0.04	1.11 ± 0.08	1.00 ± 0.02	1.2 ± 0.1
$\text{O}_{(\text{P2})}\text{-H}$	-	1.4 ± 0.1	-	1.3 ± 0.1
$\text{P-O}_{(\text{P1})}$	1.59 ± 0.04	1.57 ± 0.03	1.60 ± 0.05	1.55 ± 0.03
$\text{P-O}_{(\text{P2})}$	-	1.53 ± 0.02	-	1.54 ± 0.03
$\text{O}_{(\text{Si})}\text{-H}$	1.9 ± 0.4	-	2.3 ± 0.5	-

^a Values after local optimization. The optimized structures are shown in **Figure 4-10 (a to d)**.

^b Average values over the last 2.5 ps out of 10 ps of MD simulation. The configurations shown in **Figure 4-10 (a to d)** were used as input geometries.

The implications of the $(\text{TMPO})_2\text{H}^+$ formation depend on its coexistence with the other arrangements analysed above. The acid proton may be shared between $\text{O}_{(\text{P})}$ and $\text{O}_{(\text{Al})}$, or between $\text{O}_{(\text{P}1)}$ and $\text{O}_{(\text{P}2)}$; the former alternative produces a *strong* proton transfer, as was observed above after the MD simulation, whilst the latter corresponds to $(\text{TMPO})_2\text{H}^+$, interpreted as *weak* acidity in the ^{31}P NMR spectrum. The relative occurrence of the first or the second alternative should depend on the number and mobility of TMPO molecules throughout the framework. For instance, a second TMPO can get close to the acid site where a protonated phosphine is already interacting through an H-bond with one of the $\text{O}_{(\text{Al})}$ atoms. The second $\text{O}_{(\text{P}2)}$ may replace $\text{O}_{(\text{Al})}$ within the H-bond to form $(\text{TMPO})_2\text{H}^+$ (our MD simulation was too short to observe this transformation when more than one TMPO were adsorbed). Although $\text{O}_{(\text{P}2)}$ is more basic than $\text{O}_{(\text{Al})}$, both TMPO molecules must have a specific orientation to properly share the proton. Owing to the presence of the $(\text{CH}_3)_3\text{P}$ segment, steric effects may play against the formation of $(\text{TMPO})_2\text{H}^+$, which are accentuated by the confinement along the pore system. At the external surface, the TMPO's mobility and number increases, as well as the access to the acid sites. This favours the formation of $(\text{TMPO})_2\text{H}^+$ over the adsorption of a single TMPO at the acid site, and may be the reason behind the disappearance of the ^{31}P signal for *strong* acids at the external surface of zeolite MFI [32,59]. Once the $(\text{TMPO})_2\text{H}^+$ is formed, an additional equilibrium between $(\text{TMPO})_2\text{H}^+$ and $(\text{TMPOH}^+ + \text{TMPO})$ can be established. This suggestion may explain the presence of *very-strong* proton transfer, considering that we only observed an average $\text{O}_{(\text{P})}\text{-H}$ bond length below 1.01 Å after MD simulation for the TMPOH^+ species in **Table 4-8**. A similar process is proposed for the solvation of H^+ ions in an aqueous medium, where a interconversion between H_5O_2^+ and $(\text{H}_3\text{O}^+ + \text{H}_2\text{O})$ is observed using Car-Parrinello MD [207].

4.7 Chapter Conclusions

We have used DFT with dispersion corrections to study the adsorption of TMPO at the internal and external surfaces of zeolite MFI, with the T2-site substituted by Al. We initiated relaxation of the structures using local geometry optimization, followed by 10 ps of MD centred at 300 K; we considered the MD results as the final criterion to characterize the acid site. The acid should perform as *strong*, according to the ^{31}P chemical shift, when the proton is shared between the TMPO's oxygen atom and one of the framework O atoms that bind the Al. This trend holds when the number of TMPO molecules around the BA site increases, with the only exception the adsorption of three molecules at the internal surface. In that case, one of the non-protonated TMPO molecules directly interacts with the Al centre through direct contact between $\text{O}_{(\text{P})}$ and Al. This interaction weakens the $\text{O}_{(\text{Al})}$ -Al bond, making the $\text{O}_{(\text{Al})}$ -H bond stronger and less prone to be broken; in consequence an $\text{O}_{(\text{P})}$ -H bond length of around 1.1 Å is calculated, which translates into an acid strength classified as *weak* by ^{31}P NMR. The TMPO-Al interaction is more likely at the internal surface, where confinement effects keep the TMPO within close proximity of the Al atom. At the external surface, the non-protonated TMPO molecules tend to migrate from the acid site, and establish H-bonds with nearby silanol groups.

We only observed $\text{O}_{(\text{P})}$ -H bond lengths smaller than 1.01 Å (acid classified as *very-strong* by ^{31}P NMR) when a protonated TMPO was assumed to migrate from the acid site. In the absence of H-bonding between $\text{O}_{(\text{P})}$ and $\text{O}_{(\text{Al})}$, the $\text{O}_{(\text{P})}$ -H bond becomes shorter. Furthermore, if the acid proton is shared between two TMPO molecules, forming $(\text{TMPO})_2\text{H}^+$, the $\text{O}_{(\text{P})}$ -H bond length increases to an average value of 1.1 Å, producing ^{31}P chemical shifts that classify the acid as *weak*. Therefore, the three main regions in the ^{31}P spectrum that are used to classify the

acid sites as *very-strong* (90 – 80 ppm), *strong* (80 – 70 ppm) and *weak* (70 – 60 ppm), may be derived from the coexistence of the species $\text{TMPOH}^+\cdots\text{O}_{(\text{Si})}$ (*very-strong*), $\text{TMPOH}^+\cdots\text{O}_{(\text{Al})}$ (*strong*) and $(\text{TMPO})_2\text{H}^+$ (*weak*).

Chapter 5 Zeolite-mediated Tautomerization of Phenol and Catechol

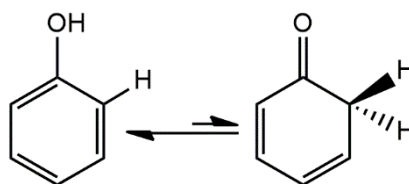
5.1 Introduction

Lignin is one of the most abundant components of biomass, representing 10 to 35% in mass and 40% in energy [62,63]. However, lignin is a three-dimensional polymer with a high number of C-C and C-O linkages between the phenolic building blocks, which limits its use as a source of more valuable chemicals and fuels [63,213,214]. Various processes have been reported to depolymerize lignin to smaller and soluble components, which are then chemically transformed depending on their future applications. Relevant examples include the mechano-catalytic depolymerisation of lignocellulose [215], the catalytic fast pyrolysis [68] or the metal-catalysed hydroprocessing of organosolv lignin [216]. Lignin-derived compounds have significant potential to replace fossil fuels as a source of heat and power [63], but first their energy content has to be enhanced by increasing the C:O and H:C ratios [62,217].

The modification of the C:O and H:C ratios is primarily restricted by the aromatic moieties that constitute the lignin: the C-O bond in phenolic species is approximately 84 kJ/mol stronger than the same type of bond in aliphatic compounds [218]. In this regard, mono- and bi-metallic nanoparticles supported on zeolites show promising results towards the hydrodeoxygenation (HDO) of lignin [70,73,74,216,219]. These methods effectively increase the C:O and H:C ratios whilst using milder conditions than pyrolytic processes [65–68], leading to higher yields and selectivity with

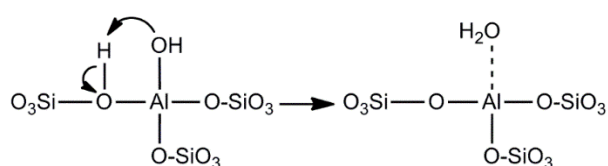
practically no solid residues. The role of the zeolite in the HDO treatment is assumed to be related to the removal/addition of aliphatic side chains and the dehydration of aliphatic alcohols, which is carried out by Brønsted and Lewis acid sites. The hydrogenation/hydrogenolysis of the aromatic ring is essentially considered to be due to the metal acting as catalyst, although an enhancement of its function is noted in the presence of the zeolite [219].

In the present thesis, we have analysed the activation of phenolic monomers on the external Lewis acid sites of zeolite MFI. The proposed transformation is the keto-enol tautomerization shown in **Scheme 1**, which involves the transfer of the hydroxyl hydrogen of phenol to one of the carbon atoms at the *ortho* position, thereby changing the hybridization of the carbon atom from sp_2 to sp_3 . This loss of molecular aromaticity promotes the hydrogenation of the molecule [76,220]. For instance, the initial tautomerization of m-cresol to an unstable cyclo-hexadienone has been reported to be the preferred pathway towards HDO over the Pt/SiO₂ catalyst [78]. Likewise, the tautomerization of phenol is considered a possible intermediate process during the hydroprocessing on Pd/SiO₂, Pd/Al₂O₃, and Pd/ZrO₂ [81]. Similar bifunctional catalysts use zeolite as a support during the HDO of lignin and phenols [73,219], which has prompted us to use computational tools to understand the potential role of the zeolite's active sites in the tautomerization process.



Scheme 1. Representation of the keto-enol tautomerization of phenol.

Previous reports have underlined the synergy arising at the metal-support interface for hydrogenation processes, derived from the combined action of support and nanoparticles; this cooperation rules the pathway and selectivity of the reaction during the hydroprocessing [81,221]. Metal nanoparticles should be found at the external surface of the zeolite because their sizes are larger than 2 nm [73,219], which is bigger than the pore dimension of zeolite frameworks. As such, the external active sites of zeolites will be relevant in the synergistic effect of the metal-support interface. Accordingly, we have focused our attention in this study on the adsorption and reaction of representative molecules, phenol and catechol, on the external surface of the zeolite MFI, modelled here as a periodic slab model. This model is not far from reality; MFI nanosheets have been successfully synthesized as thin as a single unit cell along the [010] direction, whilst extending two-dimensionally over its (010) plane [54]. We have chosen the three-coordinated aluminium centre within the zeolite framework as the active site to adsorb the molecules. This site presents Lewis acidity owing to the under-coordination of the aluminium atom, as shown in **Scheme 2**, which has been shown by computer simulations to be thermodynamically and kinetically favoured [187,203].



Scheme 2. Representation of the dehydration of an Al-substituted silanol with the subsequent formation of a tri-coordinated Al centre.

The first part of the result section is dedicated to the determination of the most stable aluminium-substituted silanol to adsorb the molecules. In the second part, we have presented a detailed mechanistic analysis of the adsorption and reaction of phenol,

including the energy barriers along the pathway, to achieve its isomerization. We have examined the catechol adsorption in the final section, and analysed the consequences of the second hydroxyl group in the tautomerization process.

5.2 Computational Methods

We have performed all calculations within the framework of the Density Functional Theory, using the plane wave code *Vienna Ab-initio Simulation Package* (VASP) [82–85]. We used the generalized gradient approximation (GGA), as derived by Perdew, Burke and Ernzerhof (PBE) [100], in combination with Grimme’s correction for the dispersion forces to account for the exchange-correlation energy at short- and long-range. In a previous report, we have shown that the inclusion of Grimme’s atomic pairwise dispersion correction (PBE-D2) [124] decreases the error of the computed volume of the MFI unit cell, and also gives a better prediction of the bulk modulus [203]. In the present thesis, we have considered a more recent approach to the dispersion interactions, which incorporates geometry information into the *ab-initio* parametrization of the dispersion coefficients (PBE-D3) [125,222]. The PBE-D3 method closely agreed with PBE-D2, but the best outcome was achieved considering the Becke-Johnson damping (PBE-D3_BJ) protocol, reducing the volume error of the unit cell to only 0.5 % (see **Table 5-1**). This result prompted us to choose the PBE-D3_BJ approach to perform all calculations.

Table 5-1. Structural parameters after optimization of the bulk unit cell of the zeolite MFI with the PBE functional in combination with the Grimme's methods (D2 and D3) that account for the Van der Waals interactions.

	a (Å)	b (Å)	c (Å)	V (Å ³)	K (GPa) ^d
PBE ^a	20.476	20.243	13.595	5635	24.3
PBE+D2 ^a	20.317	19.979	13.413	5445	18.0
PBE+D3_Zero ^b	20.320	20.022	13.453	5473	18.0
PBE+D3_BJ ^b	20.272	19.942	13.400	5417	18.4
Exp. ^c	20.140	19.930	13.426	5389	18.2

^a From Ref [203].

^b Using the **Zero** or Becke-Johnson (**BJ**) damping function.

^c From Ref [171].

^d Calculated bulk modulus using the Birch–Murnaghan equation of state [170].

We have optimized the orthorhombic unit cell of the MFI framework, available from the Structure Database of the International Zeolite Association (IZA). A representation of the optimized MFI framework is shown in **Figure 5-1**. A set of fixed-volume calculations were performed, allowing the relaxation of the lattice shape and atomic positions. Thereafter, the correlation of the optimised lattice energy versus the cell volume was fitted to the Birch-Murnaghan equation of state [170]. This methodology eliminates the problems related to the Pulay stress [169] whilst giving the equilibrium volume and the bulk modulus as adjustable parameters (see **Table 5-1**).

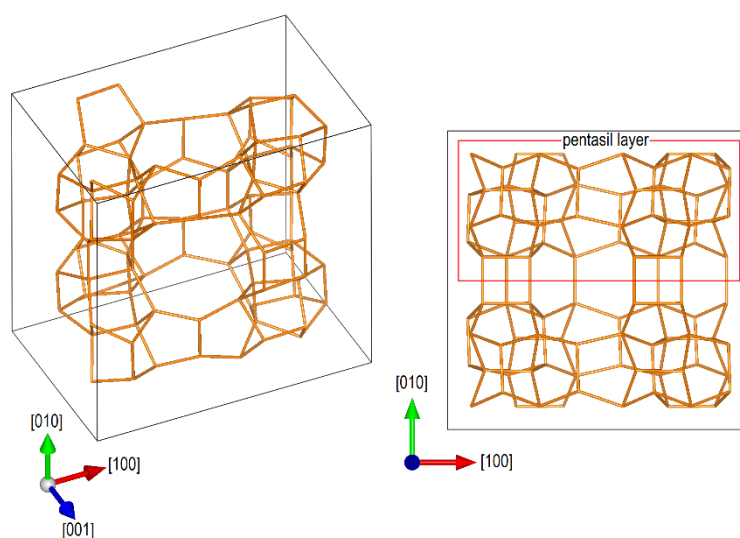


Figure 5-1. Top and lateral views of the optimized unit cell of the zeolite MFI. One of the two pentasil layers is highlighted within red lines. The O atoms are deleted for an enhanced view. Vicinal Si atoms are linked by orange sticks.

The valence electrons were explicitly treated by means of a plane wave basis set with energy cutoff of 550 eV; their nodal features and interaction with the inner core were described by the projected-augmented-wave method (PAW) [113,114]. The Gaussian smearing method was included to improve the electronic convergence, setting band widths of 0.1 eV (zeolite and molecule/zeolite) or 0.01 eV (isolated molecules) [204,205]. Owing to the large dimension of the MFI unit cell, with lattice vectors of over 13 Å, only the Gamma point was used to perform the numerical integration within the Brillouin zone. The convergence criteria for the electronic and ionic forces were set at 10^{-5} eV and 0.03 eV/Å, respectively.

The binding free energies of the molecules to the acid sites were calculated according to the following equation:

$$F_{Bind.} = F_{molecule/zeolite} - (F_{zeolite} + F_{molecule}^{gas}) \quad (5-1)$$

where $F_{molecule/zeolite}$ is the free energy of a system constituted by the zeolite and a molecule of phenol/catechol adsorbed on the Lewis acid site, $F_{zeolite}$ is the free energy of the bare zeolite, and $F_{molecule}^{gas}$ is the energy of a molecule of phenol/catechol in the gas phase. The term *gas phase* is used for a single molecule optimized within a $30 \times 31 \times 32$ Å³ supercell. The values of the free energies were calculated after including the zero-point energy correction and the entropic effects at 473 K, which is a fair representation of the range of temperatures commonly used [70,73,74,223]. Only the vibrational contribution to the entropy was considered for the zeolite/adsorbate systems. In that case, the harmonic vibrational partition function was calculated using the normal modes derived from the movement of the Al atom, the first sphere of SiO₄ tetrahedra binding the Al and the adsorbed molecule of phenol or catechol, whilst the rest of the atoms were kept frozen. In the case of

molecules in the gas phase, the rotational and translational contributions to the entropy were also considered, assuming them to be ideal gases.

We applied the Nudged Elastic Band (NEB) method to each reaction step to determine the initial guess of the transition state (TS) [134,135]. This technique starts the exploration of the minimum energy pathway (MEP) between reactants and products by linking both states with evenly spaced images connected by harmonic springs. The perpendicular component of the spring force, which tends to make the images collinear, is zeroed. The same treatment is given to the parallel component of the potential energy gradient, which tends to move the images towards the closest minimum. In this thesis, we have used between one and four images to create the elastic bands, depending on the particular configuration, and a value of 0.1 eV/\AA was used as convergence criterion for the adjusted force on each image. The position of the TS was refined using the improved dimer method (IDM) [137], which increases the robustness and efficiency of the original dimer method (DM) proposed by Henkelman and Jónnson [136]. The DM is an algorithm to search for local saddle-points using the potential energy gradients, thus avoiding expensive evaluations of the Hessian matrix during the search. Two configurations in the multi-dimensional space, separated by a small vector (dimer axis), are used to follow the mode with the lowest negative curvature in the potential energy. The starting path to align the dimer is the hardest imaginary mode of the TS guess derived from the NEB calculation. In this way a faster convergence is achieved. The IDM is considered converged when a gradient criterion is reached along the lowest negative curvature. In the present thesis, we have used a threshold of 0.03 eV/\AA . During the geometry optimization of the TS, using the NEB method and IDM, only the Al atom, the first sphere of the SiO_4 tetrahedra binding the Al, including any H binding the framework O atoms,

and the molecule were allowed to relax, whereas the rest of the atoms were kept frozen in their positions. The systems containing the reactant and product of each step were fully relaxed without any geometry constraints.

The images of the structural geometries were obtained with the code *Visualization for Electronic and Structural Analysis* (VESTA 3) [168].

5.3 Slab Model and Aluminium Distribution

We used the optimized MFI unit cell to construct the zeolite slabs by keeping the periodicity along the [100] and [001] directions, and cutting along the [010] direction, which coincides with the straight pore orientation. Silanol groups were formed after saturation of the dangling Si-O bonds at the external surface. A vacuum layer of 20 Å was inserted to avoid interactions between periodic images. Thereafter, we performed the Al substitution at the twelve non-equivalent T-sites exposed at the external surface. Two slabs were tested: the first one was constructed with two pentasil layers, which reproduced the thinnest experimental thickness of an MFI nanosheet (**Figure 5-2a**) [58], whilst the second model was formed by a single pentasil layer in order to reduce the computational cost of the calculations (**Figure 5-2b**). Both thicknesses were compared during the analysis of the Al substitution to validate the use of the one-pentasil slab model.

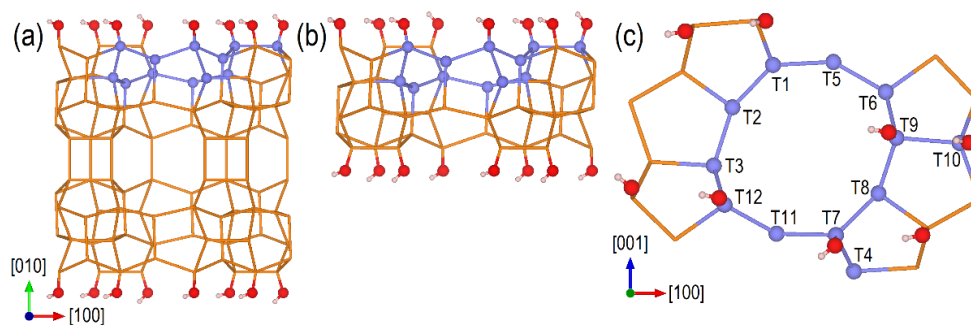


Figure 5-2. Lateral view of MFI slabs formed by (a) two and (b) one pentasil layer. (c) Top view of the slab with the numeration of the twelve non-equivalent T sites (balls in light blue). The framework O atoms are deleted for an enhanced view, silanol O atoms are shown in red, H in white. Vicinal Si atoms are linked by orange sticks.

The Al substitution creates a negative charge within the framework, owing to the replacement of Si atoms with formal charge 4+ by Al with 3+. This negative charge is balanced by tetraalkylammonium cations, which also act as structure directing agents (SDA) during the synthesis of Al-doped zeolite [148]. We considered the explicit presence of the SDA by placing a tetramethylammonium (TMA) cation in the centre of the intersection between the sinusoidal and straight channels, as shown in **Figure 5-3**, where we have disregarded the fact that in experiment the alkyl chain is much longer than one carbon atom [148]. However, we decided to use the tetramethylammonium to simplify the explicit consideration of the counter-ion.

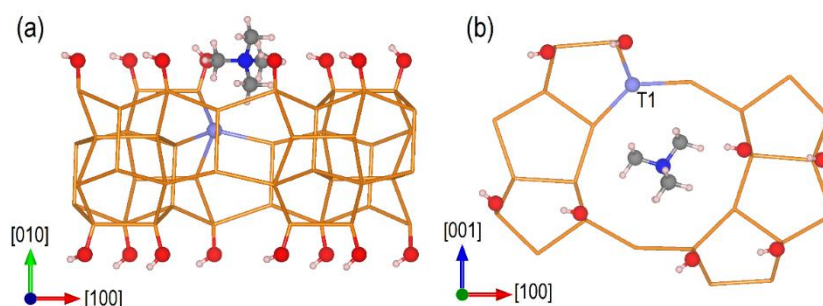


Figure 5-3. (a) Lateral and (b) top views of the slab formed by one pentasil layer loaded with one molecule of tetramethyl ammonium. The Al substitution at T1 site is included as an example. The framework O atoms are deleted for an enhanced view, silanol O atoms are shown in red, H in white, C in grey, N in dark blue and Al in light blue. Vicinal Si atoms are linked by orange sticks.

Despite the difference in thickness, the two slabs shown in **Figure 5-2** led to practically the same order of stability among the Al-substituted T-sites, as shown in **Figure 5-4a**. Furthermore, the distortion of the straight pore followed a similar pattern of expansions and contractions for the twelve different Al substitutions, regardless of the size of the slab (see **Figure 5-4b** and **Figure 5-4c**). Having ascertained that the one-pentasil slab adequately reproduced the results of the two-pentasil slab, we have used the former to analyse the adsorption and tautomerization of phenol and catechol.

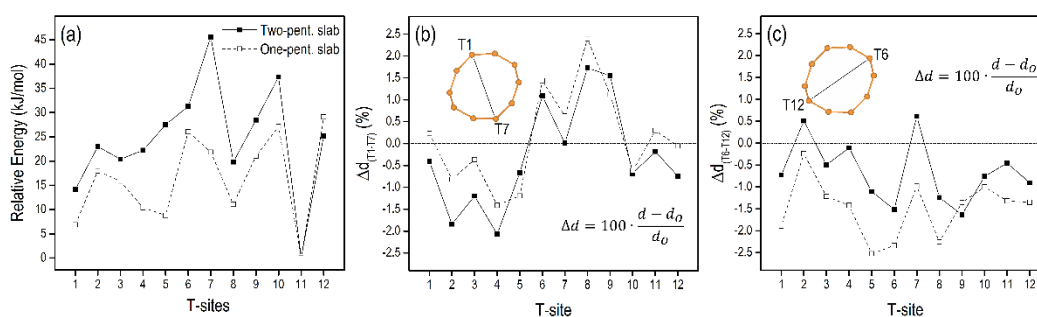


Figure 5-4. (a) Relative energy of the Al substitution at each non-equivalent T-site within the slabs formed by one and two pentasil layers. (b, c) Variation of the diameter of the straight pore considering the distances $d_{(T1-T7)}$ and $d_{(T6-T12)}$, and comparing against the values $d_{0(T1-T7)}$ and $d_{0(T6-T12)}$ of the pure silica zeolite.

The determination of the Al distribution is a challenging task, both experimentally and theoretically, due to the large number of factors influencing the synthesis process of the final zeolite [178,180,224]. However, the more stable structures will occur more frequently within the zeolite framework [178]. According to the results of the Al distribution in the one-pentasil slab (see **Figure 5-4a**), the T9 site was the most stable Al-substituted silanol out of four available positions: T7, T9, T10 and T12 (see **Figure 5-2c**). The dehydration of Al-substituted silanols has an energy barrier of between 10 and 20 kJ/mol, leading to a water molecule adsorbed on a three-coordinated Al centre, which is more stable than the initial Al-substituted silanol by

12 to 45 kJ/mol [187,203]. The water that is formed during dehydration may be removed after thermal pre-treatment, leaving a naked three-coordinated Lewis site (see **Figure 5-5**) [225]. We have therefore used the dehydrated form of the T9 site to analyse the adsorption of phenol and catechol on a Lewis site at the external surface of zeolite MFI. Because the Al-substituted T9 site is three-coordinated after assuming its dehydration, we did not have to consider any longer the presence of the counter-ion (TMA) within the system.

5.4 Adsorption of Phenol

We have considered two different configurations for the adsorption of phenol on the Al-substituted T9 site, referred to as non-planar (**Figure 5-5a**) and co-planar (**Figure 5-5b**) configurations. We have also examined the binding through the C atoms at *ortho* and *para* positions (C2 and C4 in **Figure 5-5**).

Figure 5-5 shows the most stable geometries, after optimization, for the adsorption of phenol through its O atom with non- and co-planar configurations (hereafter we use O_{ph} and H_{ph} to refer to the hydroxyl group of phenol). The co-planar adsorption of phenol on the Lewis site T9 was stronger than the non-planar configuration, with binding free energies of -42 and -13 kJ/mol, respectively. The binding free energy of phenol through the C2 and C4 atoms on T9 was +4 and -7 kJ/mol, respectively. Hence, the adsorption of phenol takes place preferentially through the O_{ph} atom, and adopting a co-planar configuration.

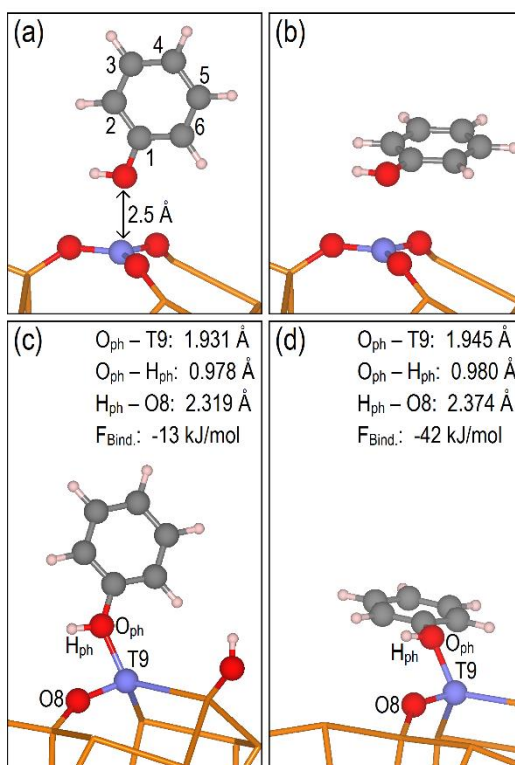


Figure 5-5. (a) Non-planar and (b) co-planar adsorption configurations of phenol on the T9 site before optimization, setting an initial O_{ph}-Al distance of 2.5 Å. The numeration of the C atoms is included in configuration (a). (c) Non-planar and (d) co-planar adsorptions with the strongest binding free energies after geometry optimization. Selected interatomic distances are included together with the binding free energy ($F_{Bind.}$). Most of the framework O atoms are deleted for an enhanced view, relevant O atoms are shown in red, H in white, C in dark grey and Al in light blue. Vicinal Si atoms are linked by orange sticks.

The elongation of the O_{ph}-C bond was the main deformation of phenol upon adsorption, becoming longer for stronger O_{ph}-Al interactions. For instance, the average O_{ph}-C bond length reached values of 1.407 and 1.431 Å for the non- and co-planar configurations, respectively, compared with a gas phase value of 1.376 Å.

5.4.1 Dissociation of Phenol

We have considered the dissociation of phenol and the formation of phenoxide as the first elemental step towards the tautomerization (see **Scheme 1**). In this process,

the $O_{\text{ph}}-H_{\text{ph}}$ bond was broken and H_{ph} transferred to the closest framework O atom binding the Al. We have used the geometries with the strongest binding free energies on T9 to investigate the formation of phenoxide. The Bader analysis of atomic charges [208–210] confirmed that H_{ph} was transferred as a positive proton, leaving a counterbalancing negative charge above $-0.8 e^-$ within the phenoxide.

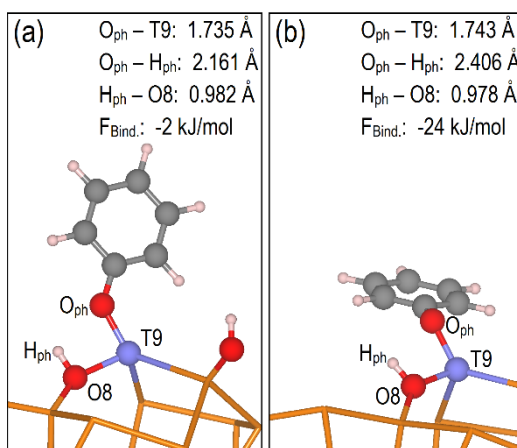


Figure 5-6. Optimized geometries after the transfer of H_{ph} to the closest framework O atom binding the Al. (a) Non-planar adsorption, (b) co-planar adsorption. Selected interatomic distances are included together with binding free energies ($F_{\text{Bind.}}$). Most of the framework O atoms are deleted for an enhanced view, relevant O atoms are shown in red, H in white, C in dark grey and Al in light blue. Vicinal Si atoms are linked by orange sticks.

Figure 5-6. shows the optimized structures with non- and co-planar configurations after the dissociation of the $O_{\text{ph}}-H_{\text{ph}}$ bond at the T9 Lewis acid site. The relative energy of the system increased by 11 and 18 kJ/mol, with the $O_{\text{ph}}-C$ bond length decreasing to 1.354 and 1.369 Å upon deprotonation, for the non- and co-planar configurations, respectively (see **Figure 5-6.**).

The energy barrier for the formation of phenoxide on T9 is practically independent of the phenol configuration. We obtained values of 41 and 49 kJ/mol, respectively, depending on whether the molecule had a non-planar or a co-planar configuration (see **Figure 5-7.**). These barriers are at least 20 kJ/mol higher than the dehydration

process of an Al-substituted silanol, which involves the deprotonation of the framework O atom binding the Al (Brønsted acid) and the transfer of the proton to the hydroxyl group attached to the Al, with the subsequent formation of water (see **Scheme 2**, section 5.1) [187,203]. In comparison, an activation energy of 19 kJ/mol has been reported for the dissociation of phenol on Pd(111), increasing to 46 kJ/mol when the adsorption takes place on Pt(111) [226]. In addition, the dissociation of the O-H bond of m-cresol on Pt(111) and Ru(0001) reveals barriers of 39 and 45 kJ/mol, respectively [80]. Therefore, our calculated activation energies show that the dissociation of phenol on the Lewis acid sites of zeolites is as probable as on metallic surfaces, and thus can take place at relatively low temperatures.

The reverse reaction, which regenerates phenol from phenoxide, had barriers of approximately 30 kJ/mol. However, the phenoxide is free to rotate, and change its orientation, whilst H_{ph} remains bound to the framework O atom. This alternative route is energetically less expensive than the regeneration of phenol, and has the additional advantage of favouring the transfer of H_{ph} to C2.

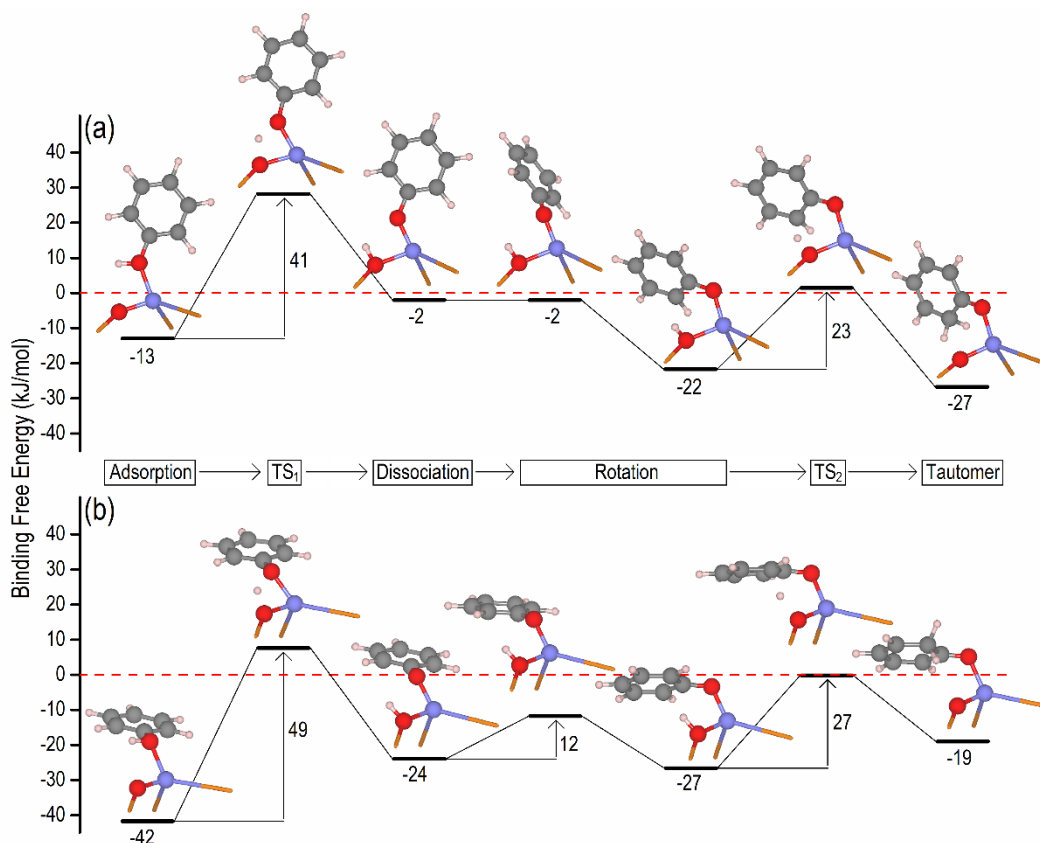


Figure 5-7. Tautomerization pathways for the adsorption of phenol with (a) non-planar and (b) co-planar configurations of adsorbed phenol. The horizontal dashed line marks the reference energy (shifted to zero), constituted by the bare zeolite and a molecule of phenol in the gas phase.

5.4.2 Rotation of Dissociated Phenol

The isomerization of phenol to form cyclohexa-2,4-dien-1-one (see **Scheme 1**, section 5.1) requires the H_{ph} transfer to one of the C atoms at the *ortho* position. In the initial relaxed orientation of phenoxide adsorbed on the Lewis acid T9 site (**Figure 5-6**), the direct transfer of the proton from O8 to C2, forming cyclohexa-2,4-dien-1-one, was less probable than the regeneration of phenol. However, after a change in the phenoxide orientation through the rotation of the dihedral angle C2-O_{ph}-Al-O, shown in **Figure 5-8**, the transfer of H_{ph} became feasible.

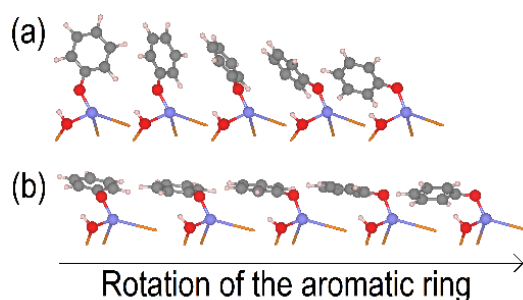


Figure 5-8. Representations of successive geometries along the rotation pathways that places the C2 atom at favourable distance from H_{ph}. (a) Non-planar and (b) co-planar configurations.

Figure 5-9 shows the optimized configurations after the phenoxide rotation. The non-planar adsorption had a binding free energy of -22 kJ/mol, whilst the co-planar adsorption was -27 kJ/mol (see **Figure 5-9**). The new orientations led to a decrease in the H_{ph}-C2 distances to approximately 2.0 Å and a small increase in the H_{ph}-O8 bond length from 0.99 Å to approximately 1.01 Å. The elongation of the H_{ph}-O8 bond indicates the interaction between H_{ph} and the aromatic π states of phenol, which favours the proton transfer to form cyclohexa-2,4-dien-1-one (see **Figure 5-9**).

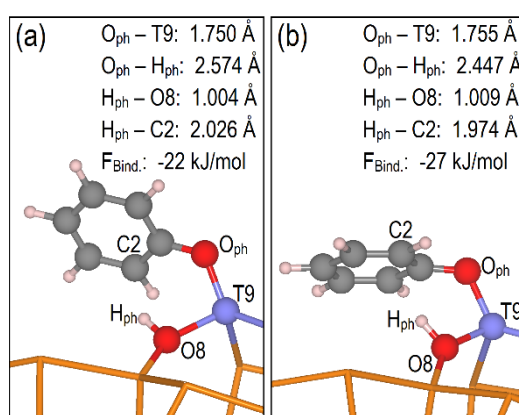


Figure 5-9. Optimized geometries after the rotation of the aromatic ring of the phenoxide adsorbed on the T9 site. (a) Non-planar and (b) co-planar configurations. Selected interatomic distances are included together with the binding free energies ($F_{Bind.}$). Most of the framework O atoms are deleted for an enhanced view, relevant O atoms are shown in red, H in white, C in dark grey and Al in light blue. Vicinal Si atoms are linked by orange sticks.

The calculated energy barrier of the rotation pathway was smaller than 12 kJ/mol for the co-planar configuration. In the case of the non-planar configuration, the reorientation of the phenoxide occurred smoothly, without measurable barrier, as shown in **Figure 5-7**. The newly adopted orientations of the aromatic ring hinder the regeneration of phenol, for which a reverse rotation is needed, but our observations indicate that phenoxide is likely to rotate constantly around the axis O_{ph}-Al.

5.4.3 Formation of Cyclohexa-2,4-dien-1-one

The final step of the phenol tautomerization involves the transfer of H_{ph} to C2 with the subsequent formation of cyclohexa-2,4-dien-1-one. The optimized structures after the proton transfer are shown in **Figure 5-10**. The non-planar configuration of the newly formed cyclo-hexadienone was more stable than the co-planar orientation by 8 kJ/mol. The non-planar configuration had a binding free energy of -27 kJ/mol, with reference to a molecule of phenol in the gas phase together with the bare zeolite. The cyclo-hexadienone in the gas phase is less stable than phenol by 70 kJ/mol, which means that once the tautomerization has occurred, regeneration of phenol is still more likely than desorption of cyclo-hexadienone from the Lewis acid site, although solvent effects may encourage the desorption process. However, the surface-bound cyclohexa-2,4-dien-1-one may undergo further hydrogenation without regenerating phenoxide or phenol [81,221].

After the formation of cyclohexa-2,4-dien-1-one, the O_{ph}-Al bond length increased from approximately 1.75 Å in the phenoxide to 1.85 Å, which was accompanied by

a decrease of the $O_{\text{ph}}\text{-C}$ bond length to an average of 1.29 Å in both the non- and co-planar configurations.

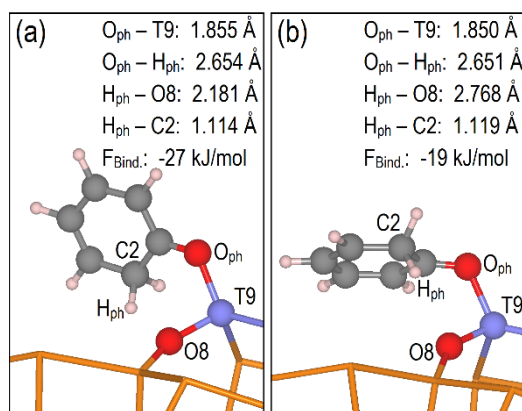


Figure 5-10. Optimized geometries of (a) non-planar and (b) co-planar configurations after the transfer of H_{ph} to the C2 of the phenoxide adsorbed on the T9 site. Selected interatomic distances are included together with the binding free energies ($F_{\text{Bind.}}$). Most of the framework O atoms are deleted for an enhanced view, relevant O atoms are shown in red, H in white, C in dark grey and Al in light blue. Vicinal Si atoms are linked by orange sticks.

We have calculated an energy barrier for the transfer of H_{ph} to C2 of 23 and 27 kJ/mol for the two configurations (see **Figure 5-7.**), which is almost half the barrier for the phenoxide formation. This barrier is significantly lower than the equivalent process for phenol and m-cresol on Pt(111), Pd(111) and Ru(0001), where values between 63 and 93 kJ/mol have been reported [80,226]. At the same time, an activation energy of 37 kJ/mol has been calculated for the water-assisted tautomerization of phenol at the Ru-TiO₂(110) interphase [221], which is within our proposed range of activation energies. We also evaluated an energy barrier of 242 kJ/mol for the direct tautomerization of phenol in the gas phase, which was more than four-fold larger than the barriers along the pathways depicted in **Figure 5-7.** The magnitude of the activation energy in the gas phase agreed with previous theoretical works that portray the energetics of this process as highly demanding [227,228]. Our results show that the tautomerization of phenol is effectively

catalysed on the external Lewis acid sites of zeolite MFI, becoming kinetically viable under relative low temperature conditions.

5.5 Adsorption of Catechol

In the gas phase, catechol had two orientations for the OH groups, as shown in **Figure 5-11**. The most stable geometry (by 67 kJ/mol), where one OH group is oriented towards the second (shown in **Figure 5-11a**), was adsorbed on the T9 site following the same protocol as for phenol, *i.e.*, placing one of the two O_{ph} close to the Al atom; this arrangement is referred along the text as the monodentate adsorption (MOA). We used the nominative *second* O_{2ph} to refer to the O_{ph} not binding the Al centre, and not going through dissociation during the first step of tautomerization. We have also utilized the less stable configuration of catechol, with the two $O_{ph}-H_{ph}$ bonds oriented in opposite directions (see **Figure 5-11b**), to simultaneously bind both O_{ph} atoms to the Al centre; this arrangement is referred to as the bidentate adsorption (BIA). In addition, both non- and co-planar configurations were considered for each adsorption.

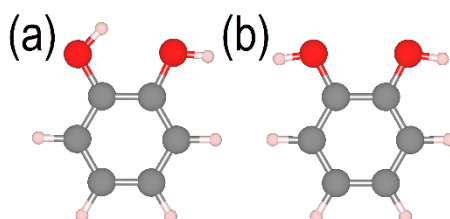


Figure 5-11. Orientations of the catechol molecule. Orientation (a) is more stable than (b) by 67 kJ/mol (including zero-point energy and entropy corrections at 437 K).

The structures with the strongest binding free energies within each configuration are shown in **Figure 5-12**, (the energy of the most stable structure of catechol was used

as a reference for both the MOA and the BIA). In the case of the MOA, binding free energies of -17 and -40 kJ/mol were calculated for the non- and co-planar configurations, respectively (see **Figure 5-12a** and **Figure 5-12b**). The $O_{1\text{ph}}\text{-Al}$ distance decreased to ~ 2.0 Å during relaxation, whilst the second $O_{2\text{ph}}$ formed an H-bond with a nearby framework O atom acting as a donor, with $O_{2\text{ph}}\text{-H}_{2\text{ph}}\cdots\text{O}$ distance of ~ 1.7 Å. At the same time, the BIA with non-planar configuration maintained both O_{ph} atoms bound to the Al centre during relaxation at the expense of an energy penalty that weakened the adsorption, rendering a binding free energy of +6 kJ/mol (see **Figure 5-12c**). However, the BIA with co-planar configuration relaxed to an MOA configuration (see **Figure 5-12d**), with a binding free energy of -39 kJ/mol (for consistency, we labelled this structure as BIA with co-planar configuration, although knowing that it relaxed to a MOA after optimization). Therefore, the adsorption strength and orientation of catechol seems to follow the same trends of phenol, *i.e.*, through a monodentate adsorption with co-planar configuration, whilst the second $O_{2\text{ph}}$ forms stabilizing H-bonds with nearby framework O atoms. However, the relative relevance of the BIA of catechol along the tautomerization process increases by kinetic and thermodynamic factors, as discussed below.

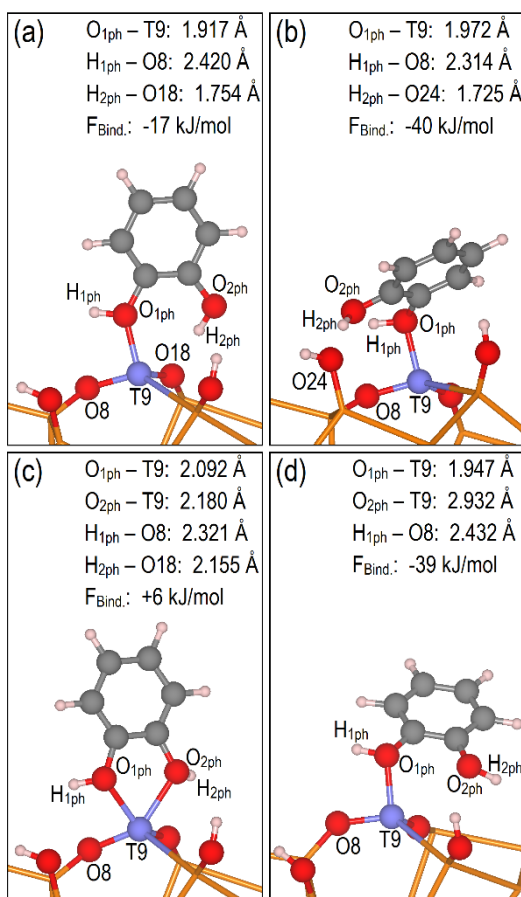


Figure 5-12. Optimized geometries with the strongest binding free energies of catechol on Lewis acid site T9: monodentate adsorption (MOA) with (a) non-planar configuration and (b) co-planar configuration; bidentate adsorption (BIA) with (c) non-planar configuration and (d) co-planar configuration; the co-planar BIA relaxed to co-planar MOA. Selected interatomic distances are included together with the binding free energy ($F_{Bind.}$). Most of the framework O atoms are deleted for an enhanced view, relevant O atoms are shown in red, H in white, C in dark grey and Al in light blue. Vicinal Si atoms are linked by orange sticks.

5.5.1 Dissociation of Catechol

Table 5-2 shows the binding free energy of the species involved in the tautomerization process, starting from the most stable geometries shown in **Figure 5-12**. In contrast with phenol, the energy of the catechol/T9 systems decreased by 4 to 29 kJ/mol after the dissociation of the $O_{1ph}-H_{1ph}$ bond, which was expressed by

binding free energies that ranged from -26 to -45 kJ/mol (see fourth column of **Table 5-2** and **Figure 5-13**).

Table 5-2. Binding free energies (in kJ/mol) of each of the species involved in the tautomerization of catechol starting from the structures in **Figure 5-12** (the barrier for the ring rotation is not included).

Labelling ^a	Ads. ^b	TS ₁ ^c	Diss. ^d	Rot. ^e	TS ₂ ^f	Taut. ^g
MOA-NP-CH	-17	+17 (34)	-26	-26	-2 (24)	-21
MOA-NP-CO	-17	+17 (34)	-26	-20	+36 (56)	+21
MOA-CP-CH	-40	+15 (55)	-45	-27	-1 (26)	-12
MOA-CP-CO	-40	+15 (55)	-45	-28	+59 (87)	+47
BIA-NP-CH	+6	+18 (12)	-23	-25	-1 (24)	-23
BIA-NP-CO	+6	+18 (12)	-23	-20	+39 (59)	+22
BIA-CP-CH ^h	-39	-3 (36)	-43	-29	-7 (22)	-23
BIA-CP-CO ^h	-39	-3 (36)	-43	-19	+39 (58)	+27

^a Labelling for the adsorbed geometries. The first three letters specify if the catechol had a pre-optimized geometry that followed a MOA or a BIA, the fourth and fifth letters specify if the molecule was adsorbed with non-planar (NP) or co-planar (CP) configuration. The sixth and seventh letters specify which C atom bound the proton after the tautomerization: the one binding an H atom (CH) or the one binding the second O_{2ph} (CO).

^b System after catechol adsorption with the strongest binding free energy.

^c Transition state for the dissociation of the O_{1ph}-H_{1ph} bond. The activation energy is given within parenthesis in kJ/mol.

^d System after the dissociation of the O_{1ph}-H_{1ph} bond

^e System after the rotation of the dissociated catechol molecule

^f Transition state for the formation of the C-H_{1ph} bond. The activation energy is given within parenthesis in kJ/mol.

^g Catechol tautomer.

^h The structure relaxed as a co-planar MOA during the optimization of the non-dissociated phenol (see **Figure 5-12d**).

The BIA took precedence over the MOA after the dissociation of the O_{1ph}-H_{1ph} bond in response to the elongation of the Al-O8 bond, as shown in **Figure 5-13**. The tetrahedron was transformed into a trigonal bipyramid, with the base formed by the dissociated O_{1ph} and the two non-protonated framework O atoms binding the Al, whilst the second O_{2ph} and the framework O atom binding H_{1ph} were placed at the top of the pyramids (see **Figure 5-13**). The MOA with co-planar configuration was the only structure that did not adopt a BIA after dissociation, owing to an unfavourable orientation that hindered the interaction between the second O_{2ph} and the Al (see **Figure 5-13b**). Therefore, although the BIA was not energetically

favourable before the $O_{1ph}-H_{1ph}$ bond dissociation, it became likely after the H_{1ph} transfer, allowing the simultaneous interaction of the two O_{ph} of catechol with the Al centre.

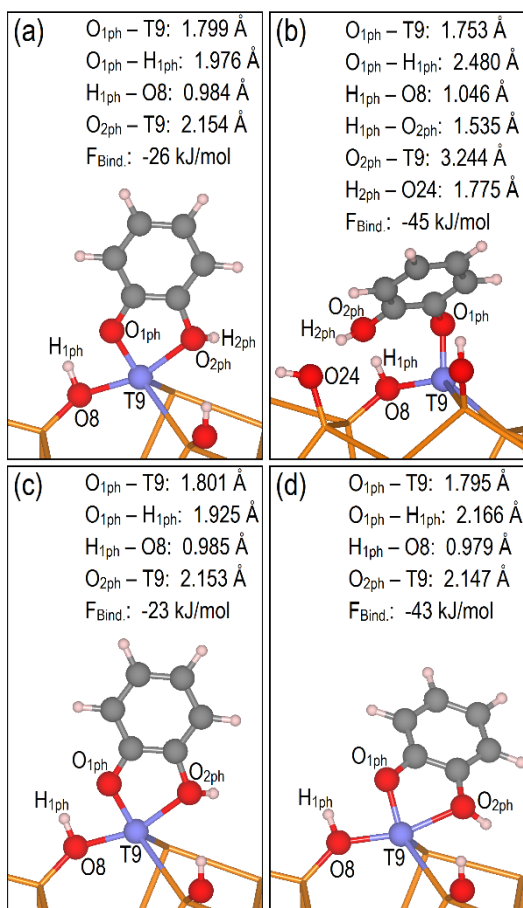


Figure 5-13. Optimized geometries after the H_{1ph} transfer of catechol to the closest framework O atom binding the Al. Representation of the MOA with (a) non-planar configuration and (b) co-planar configuration, and the BIA with (c) non-planar configuration and (d) co-planar configuration. Selected interatomic distances are included together with the binding free energy ($F_{Bind.}$). Most of the framework O atoms are deleted for an enhanced view, relevant O atoms are shown in red, H in white, C in dark grey and Al in light blue. Vicinal Si atoms are linked by orange sticks.

The dissociation of the $O_{1ph}-H_{1ph}$ bond in catechol tended to have smaller activation energies than phenol, by at least 5 kJ/mol, when the values in the third column of **Table 5-2** are compared with those in **Figure 5-7**. The lower energy barriers were due to the stabilising effect of the second O_{2ph} atom. During the dissociation, the Al-

centred tetrahedron was distorted as a consequence of the shortening of the distance between the O_{1ph} atom and the framework O8 atom, reaching a minimum in TS_1 (see **Figure 5-14**) and thus decreasing the distance that H_{1ph} needed to span to move from catechol to the zeolite. The second O_{2ph} stabilised the structure by getting closer to the Al atom during the $O_{1ph}-H_{1ph}$ dissociation in order to compensate for the distortion of the Al-centred tetrahedron, and eventually finished with the adoption of a BIA structure (see **Figure 5-13**). For example, in the TS_1 of the MOA with non-planar configuration (see **Figure 5-14a**), the H-bond $O_{2ph}-H_{2ph}\cdots O18$ was broken, and the $O_{2ph}-H_{2ph}$ bond reoriented to allow the interaction between O_{2ph} and Al, decreasing the $O_{2ph}-Al$ distance from 3.255 Å to 2.261 Å. This reorientation lowered the energy of the TS_1 , with both O_{ph} remaining bound to the Al, leading to a dissociation barrier for catechol of 34 kJ/mol. An exceptionally low activation energy of 12 kJ/mol was calculated for the BIA with non-planar configuration (BIA-NP-CH/CO entries in third column of **Table 5-2**), as a consequence of the similarity between the structures of the pre-dissociated catechol (**Figure 5-12c**) and the TS_1 (**Figure 5-14c**), with both configurations having the two O_{ph} bound to the Al centre. The MOA system with co-planar configuration (shown in **Figure 5-14b**) was the only structure where the stabilising effect of the second O_{2ph} could not take place, owing to an unfavourable molecular orientation that hampered the interaction between the second O_{2ph} and the Al centre (see **Figure 5-13c**); as a consequence, the energy barrier increased to 55 kJ/mol, which is at least 6 kJ/mol higher than in phenol.

After analysing the importance of the BIA in the TS_1 and product of the $O_{1ph}-H_{1ph}$ dissociation, the preferred configuration for the catechol adsorption should be reconsidered. We stated above that the MOA of catechol from the gas phase is more

stable than BIA by at least 23 kJ/mol (see **Figure 5-12** and second column of **Table 5-2**). However, catechol may adsorb from the gas phase through a less thermodynamically favourable BIA with non-planar configuration, to rapidly dissociate by overcoming a low energy barrier (see BIA-NP-CH/CO entries in **Table 5-2**), and conserving the bidentate adsorption at the end of the dissociation.

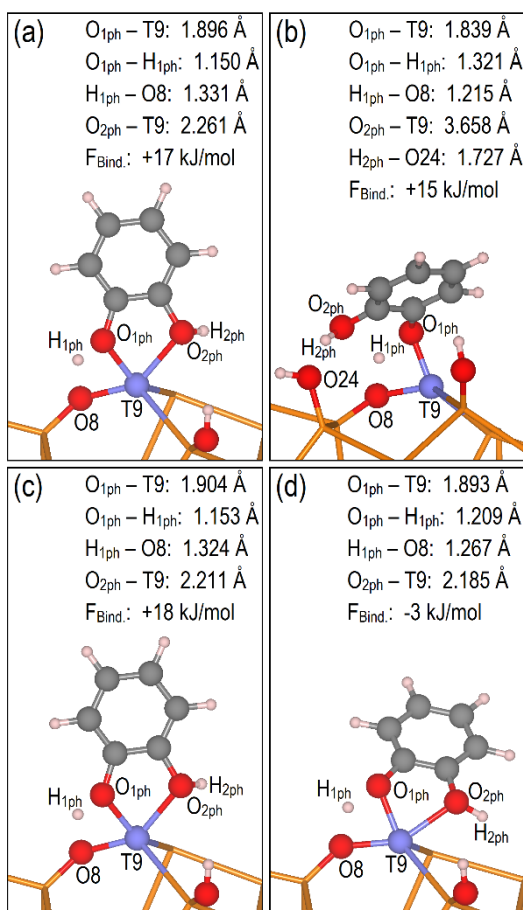


Figure 5-14. Optimized TS_1 geometries for the transfer of catechol H_{1ph} to the closest framework O atom binding the Al. Representation of the MOA with (a) non-planar configuration and (b) co-planar configuration, and the BIA with (c) non-planar configuration and (d) co-planar configuration. Selected interatomic distances are included together with the binding free energy ($F_{Bind.}$). Most of the framework O atoms are deleted for an enhanced view, relevant O atoms are shown in red, H in white, C in dark grey and Al in light blue. Vicinal Si atoms are linked by orange sticks.

5.5.2 Formation of Catechol-derived Cyclo-hexadienones

In contrast with phenol, the C atoms at ortho positions in catechol are not equivalent: one binds the second O_{2ph} (referred as C2) and the other binds an H atom (referred as C6). The transfer of H_{1ph} to C2 generated cyclohexa-3,5-dien-2-hydroxy-1-one (shown in **Figure 5-15a**), which had unfavourable binding free energies that ranged between +21 and +47 kJ/mol (see seventh column of **Table 5-2**). On the other hand, when H_{1ph} was transferred to C6, with the subsequent formation of cyclohexa-2,4-dien-2-hydroxy-1-one (shown in **Figure 5-15b**), a more thermodynamically stable product was obtained, with binding free energies between -23 and -12 kJ/mol (see seventh column of **Table 5-2**), ruling in this way the selectivity of catechol tautomerization.

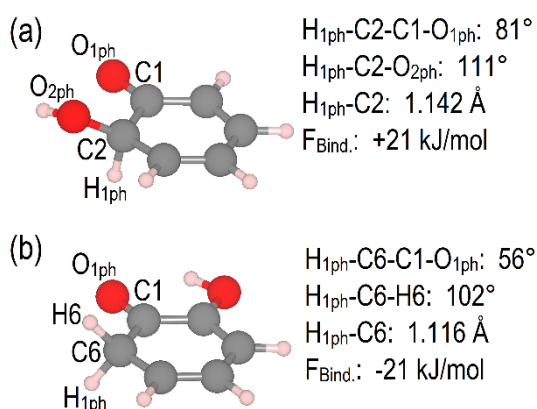
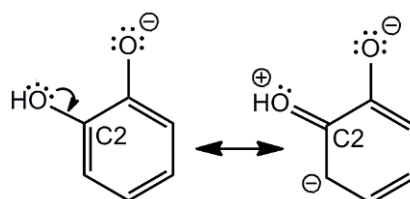


Figure 5-15. Catechol-derived cyclo-hexadienones from the MOA with non-planar configuration. (a) cyclohexa-3,5-dien-2-hydroxy-1-one, derived from the H_{1ph} transfer to C2 that binds the second O_{2ph}; (b) cyclohexa-2,4-dien-2-hydroxy-1-one, derived from the H_{1ph} transfer to C6. Hydrogen atoms are shown in white, C in dark grey and O in red. Relevant dihedral and bond angles, together with interatomic distances are shown.

The thermodynamic preference for the formation of cyclohexa-2,4-dien-2-hydroxy-1-one (**Figure 5-15b**) over cyclohexa-3,5-dien-2-hydroxy-1-one (**Figure 5-15a**) is explained by considering the π conjugation between the electronic lone pair of the second O_{2ph} and the conjugated double bonds that remain in the carbon ring, as

shown in **Scheme 3**. When H_{1ph} is transferred to C2, the π conjugation, which increases the stability of the molecule, is disrupted. In contrast, the H_{1ph} transfer to C6 leaves the π conjugation untouched together with its stabilizing effect. Furthermore, as a consequence of the formation of the cyclo-hexadienone, the C atom at the ortho position changes its hybridization from sp^2 to sp^3 , which moves the group (an aromatic H or the second O_{2ph}) connected to the C atom out of the ring plane. However, in the case of the H_{ph} transfer to C2, the second O_{2ph} tended to preserve its position on the ring plane, causing structural distortions. The reluctance of the second O_{2ph} to abandon its initial orientation forced the C2- H_{1ph} bond to be almost perpendicular to the ring plane, with a dihedral angle H_{1ph} -C2-C1- O_{1ph} of 81° , as shown in **Figure 5-15a**. In comparison, the angle H_{1ph} -C6-C1- O_{1ph} maintained a favourable value of 56° (see **Figure 5-15b**), which contributed to the higher stability of cyclohexa-2,4-dien-2-hydroxy-1-one against cyclohexa-3,5-dien-2-hydroxy-1-one. The same trend was followed by the TS_2 of each alternative pathway: the energy barriers towards cyclohexa-3,5-dien-2-hydroxy-1-one were at least 30 kJ/mol larger than the equivalent values for the formation of cyclohexa-2,4-dien-2-hydroxy-1-one (see sixth column of **Table 5-2**). A similar explanation is provided for this outcome: H_{1ph} started to disrupt the π conjugation of O_{2ph} at the TS_2 .



Scheme 3. Representation of resonance structures related with the π conjugation of the electronic lone pair of the second O_{2ph} atom with the conjugated double bonds.

We have shown that the tautomerization of phenol and catechol is effectively catalysed by the three-coordinated Lewis acid site T9 at the external surface of zeolite MFI. This process is easily attainable energetically and involves only proton transfers and the rotation of the aromatic ring. The Lewis acidity is essential for this transformation, facilitating the adsorption of the molecule, the dissociation of the $O_{\text{ph}}-H_{\text{ph}}$ bond and the formation of the C-H bond that culminates in the tautomerization. This suggests that metal substitutions conferring Lewis acidity to the zeolite should play an important role in the HDO of lignin-derived compounds by catalysing the tautomerization. There is a large collection of potential dopants with Lewis acid character to be tested in the HDO of lignin, ranging from the dehydrated, three-coordinated M^{3+} species, such as Al^{3+} , to M^{4+} substitutions that do not need dehydration to behave as Lewis acids [229,230]. For instance, it has been reported that Sn-substituted zeolite BEA is an efficient catalyst for the conversion of glucose [25,231].

Several zeolites are known to have layered forms, e.g. MFI, FER and MWW [60,61], and thus have an external surface with relatively enhanced area, which can support metal nanoparticles. This two-dimensional morphology contributes to the formation of three-coordinated Lewis acids [203], and thus to the occurrence of tautomerization during the hydroprocessing. Layered zeolites have the additional advantage of making accessible a higher number of active sites to bulkier molecules that cannot enter the micropore system [232].

Finally, we cannot guarantee that the tautomerization will occur during the HDO of lignin under a comprehensive range of conditions. The effect on the tautomerization of solvents and the presence of competing transformations, as well as the effect of

the tautomerization on the overall turnover of the hydroprocessing, should be further investigated, using both computational and experimental techniques.

5.6 Chapter Conclusions

We have analysed the tautomerization of phenol and catechol mediated by the Lewis acid sites at the external surface of Al-substituted zeolite MFI by means of Density Functional Theory including dispersion corrections. Our results show that phenol and catechol adsorb with similar strengths and preferentially in a co-planar configuration. However, in the case of catechol, the adsorption can also take place through a bidentate non-planar configuration that promptly dissociates, leading to a thermodynamically stable bidentate product.

The dissociation and transfer of the phenolic H_{ph} to one of the framework O atoms connected to the Al is considered to be the first step of the tautomerization mechanism. The activation energy of this process ranges between 41 and 49 kJ/mol for phenol and between 12 and 55 kJ/mol for catechol, considering non- and co-planar adsorptions. The molecules tend to keep the co-planar configuration after the dissociation of the $O_{ph}-H_{ph}$ bond, which is followed by a rotation of the molecule over the Al centre. The rotation of the phenoxide intermediate requires between 0 and 12 kJ/mol, avoiding the regeneration of phenol and favouring the transfer of H_{ph} to the C atoms in ortho position. The energy barrier of the H_{ph} transfer to the C atom is only 22 to 27 kJ/mol for either phenol or catechol, considering both non- and co-planar adsorptions. In the case of catechol, the transfer is kinetically and thermodynamically more likely to involve the C atom that is not binding the second O_{2ph} . Thus, we have shown that the zeolite-mediated tautomerization of phenolic

monomers is a viable process under mild temperatures, which changes the hybridization of the C atom from sp^2 to sp^3 , effectively disabling the aromatic conjugation. Finally, this thesis may help to understand better the role of the Lewis acid sites of zeolite when this material is used as a support during the hydroprocessing of lignin-derived compounds, and may contribute to better designed processes.

Chapter 6 Periodic Modelling of zeolite Ti-LTA

6.1 Introduction

Although zeolite LTA is mainly recognized by its high aluminium content (known as zeolite A), driving its applications as molecular sieve and sorbent [233], pure-silica LTA has been obtained by hydrothermal dealumination of zeolite A [234]. Recently, high silica zeolite LTA, with Si/Al ratios of 11 and 16, has shown exceptional durability in the selective catalytic reduction of NO_x with NH₃ (NH₃-SCR) under hydrothermal conditions at temperatures as high as 750 °C [235]. Furthermore, aluminosilicate LTA with Si/Al ratios between 12 and 42 has shown promising results related to the selectivity of C₅ and C₆ products in the methanol-to-olefins (MTO) reaction [53]. Boal *et al.* have also proposed the synthesis of titanosilicate, suggesting that this material may be applied to the oxidation of small molecules, taking advantage of the 8MR pore openings, the relatively large cavities and the presence of intra-framework sites with Lewis acidity [53]. Titanium-substituted zeolites have been used previously as catalysts for the epoxidation and oxidation of different organic molecules, such as phenol, ethylene and bulkier olefins [236–239].

A number of theoretical reports have analysed Ti substitution in different zeolites, such as silicalite, using cluster models and periodic boundary conditions (PBC) [230,240–243]. However, a systematic study of Ti substitution in zeolite LTA is still missing. The recent synthesis of high silica, Ti-substituted zeolite LTA [53] provides the rationale for theoretical research to elucidate the local structure, electronic

properties and distribution of Ti(IV) within the LTA framework, which fundamental information may be of use in the design of future improved catalysts.

In the present thesis, we have examined single and double substitutions of Si by Ti in the T-sites of zeolite LTA. The combination of density functional theory calculations with atomistic simulations allowed us to explore in detail the electronic structure of these systems, whilst validating the use of low Si/Ti ratios against more realistic, lower Ti concentrations. We also considered the interaction of water with the Lewis acid site, and its possible dissociation. In addition, the infrared spectrum of each structure of interest was simulated, which allowed us to propose a theoretical benchmark that may help to interpret the experimental analysis of the zeolite structure.

6.2 Computational Methods

We have performed the structural and electronic analysis of the pure-silica and Ti-substituted zeolite LTA using density functional theory (DFT) calculations as implemented in the *Vienna Ab-initio Simulation Package* (VASP) [82–85]. In addition, we have included atomistic simulations that employ the Born model of ionic solids [138], to investigate a more realistic Si/Ti ratio to complement the DFT results.

6.2.1 DFT Calculations

The DFT calculations were carried out under periodic boundary conditions, employing a basis set of plane waves to explicitly treat the valence electrons, whilst the interaction with the inner core of the atom and nodal features were described by

the projector-augmented-wave method (PAW) [113,114]. The accuracy of the basis set was guaranteed by a kinetic energy cutoff of 550 eV. We have used the generalized gradient approximation (GGA), as proposed by Perdew, Burke and Ernzerhof (PBE), to account for the exchange and correlation contributions to the electronic energy [100]. The effect of the long range dispersion forces was considered by using Grimme's atomic pairwise method, which includes three-body terms to avoid the overbinding of two-body only methods [120,124,125]. Furthermore, we have chosen the Becke-Johnson damping function to avoid the double counting of the correlation effects at short distances [222]. The Brillouin zone was sampled with a k-point mesh of $3 \times 3 \times 3$, generated with the Monkhorst–Pack scheme [108]. We have used the linear tetrahedron method, with Blöchl's correction, to account for the occupation of the electronic bands and the integration over the k-points mesh during the structural optimizations [116]. This method was employed because the systems analysed here are insulators, with all bands fully occupied or fully empty, thus avoiding the method's drawback of not being variational with respect to partial occupancies. The thresholds for the electronic and ionic iterations were set at 10^{-6} eV and 0.01 eV/Å, respectively, ensuring proper convergence.

The GGA vibrational frequencies of the zeolite framework were obtained by the diagonalization of the Hessian matrix computed by density functional perturbation theory [131]. The signal intensity of each normal mode was estimated using the following equation:

$$I_{IR}(\alpha) = \left(\sum_i^N \tau_i \nu_i(\alpha) \right)^2 \quad (6-1)$$

where $\boldsymbol{\tau}_i$ is the Born effective charge tensor of the i th atom, calculated by density functional perturbation theory and $\mathbf{v}_i(\alpha)$ is the atomic displacement in the α th eigenvector divided by the square root of its mass. The IR spectra were simulated by widening each signal with a Gaussian function.

6.2.2 Interatomic Potential Calculations

The interatomic potential (IP) calculations were performed using the *General Utility Lattice Program* (GULP), where the energy of the system comprises Coulombic contributions, calculated according to the Ewald summation method [139], and short range repulsions and dispersion forces described by Buckingham potentials [142]. For the potential model of the SiO₂ units that form the zeolite framework, we have used the parametrization proposed by Sanders *et al.* [159], which was initially developed for α -quartz, but has shown satisfactory transferability to zeolites [161–163,203]. The presence of Ti within the zeolite framework was described by the potentials reported by Jentys and Catlow [240]. The IP vibrational frequencies were computed after the diagonalization of the Hessian matrix, which was obtained by the finite difference method that keeps the system within the harmonic approximation. The signal intensity of each normal mode was evaluated by the equation:

$$I_{IR}(\alpha) = \left(\sum_i^N q_i \mathbf{v}_i(\alpha) \right)^2 \quad (6-2)$$

where q_i is the charge of the i th atom and $\mathbf{v}_i(\alpha)$ is the atomic displacement in the α th eigenvector divided by the square root of its mass.

6.2.3 Simulation Model

Within the GGA, we optimized the LTA unit cell by using a set of fixed-volume calculations, where only the atomic positions were allowed to relax. The equilibrium volume was then evaluated by fitting the Birch-Murnaghan equation of state to the correlation between the lattice energy versus the lattice volume [170]. This procedure also gave the isotropic bulk modulus as an adjustable parameter. The optimization of the cell and the atomic positions with the IP method took place at constant pressure, thus permitting the simultaneous relaxation of the cell volume and the atomic coordinates in a single calculation.

Two different cells were used for the calculations. The first one, with $Pm\bar{3}m$ symmetry and containing 24 TO_2 sites, was used for the GGA study of the pure-silica and Ti-substituted zeolite LTA. For this cell size, the single Ti substitution gave a Si/Ti ratio of 23 whilst the double Ti substitution decreased it to 11. These values are at least 4 to 5 times larger than reported experimentally [53]. However, a bigger cell would have been computationally extremely demanding, and we have therefore complemented the GGA study with IP simulations, which allow the examination of larger systems using much less computational resource. Both the GGA and the IP methods have been shown to be suitably accurate to analyse the thermodynamic and physical properties of zeolites [177,203,244,245].

The second type of cell was formed by the $2 \times 2 \times 2$ expansion of the 24- SiO_2 cell used for the GGA calculations. As such, the number of SiO_2 units increased to 192, with a Si/Ti ratio of 191 and 95 for the single and double substitutions, respectively; much closer to the experimental value of 100 [53]. All non-equivalent double substitutions of Ti in the zeolite framework were generated using the *Site Occupancy Disorder* (SOD) program, obtaining 12 structures for the $1 \times 1 \times 1$ cell and 91 structures for the

2×2×2 supercell [246]. In order to simplify the calculations, the presence of the structure-directing agent (SDA) and its effect on the Ti substitution was not considered.

The structural visualizations presented in this thesis were generated by the *Visualization for Electronic and Structural Analysis* (VESTA 3) [168].

6.2.4 Elastic Properties

The GGA elastic constants were obtained following the protocol of deformations proposed by Ravindran *et al.*, where the volume is held constant during the orthorhombic and monoclinic shear distortions [247]. Owing to the cubic symmetry of zeolite LTA, the elastic constants that we needed to evaluate reduced to C_{11} , C_{12} and C_{44} only. The elastic constants were obtained by fitting a second order polynomial equation to the correlation between the lattice energy and the applied strain:

$$E_{D_1} = E_0 + V_0\tau_1\delta + V_0\frac{C_{11}}{2}\delta^2 \quad (6-3a)$$

$$E_{D_7} = E_0 + V_0(\tau_1 - \tau_2)\delta + V_0(C_{11} - C_{12})\delta^2 \quad (6-3a)$$

$$E_{D_4} = E_0 + 2V_0\tau_4\delta + 2V_0C_{44}\delta^2 \quad (6-3a)$$

where E_{D_n} is the set of lattice energies obtained after applying the deformation D_n suggested by Ravindran and collaborators [247], E_0 is the energy at the equilibrium volume V_0 , τ_i is an element in the stress tensor and δ is the applied strain (between

-3% and 3% to minimize the contribution of higher order terms in the Taylor expansion).

The bulk modulus (B) and shear modulus (G) were obtained following the Voigt approximation, where the external strain is equated to the uniform strain in a polycrystalline ensemble [248]. The values of B and G correspond to the resistance of the material to plastic deformation and fracture, respectively. The Voigt equations use the elastic constants for the calculation of B and G :

$$B = \frac{C_{11} + 2C_{12}}{3} \quad (6-4a)$$

$$G = \frac{C_{11} - C_{12} + 3C_{44}}{5} \quad (6-4a)$$

In addition, the shear anisotropic factor (A), which measures the level of anisotropy of the material, and Young's modulus (Y) and Poisson's ratio (σ), which give information regarding the rigidity of the crystal, were calculated from equations:

$$A = \frac{2C_{44}}{C_{11} - C_{12}} \quad (6-5a)$$

$$Y = \frac{9BG}{3B + G} \quad (6-5a)$$

$$\sigma = \frac{3B - 2G}{6B + 2G} \quad (6-5a)$$

In the case of the IP method, the elastic parameters were directly provided by GULP following Voigt's approximation.

6.3 Pure-silica Zeolite LTA

After structural relaxation within the GGA of the pure-silica LTA, we obtained a cubic unit cell parameter of 11.950 Å, which was only 0.8% longer than the reported value by Boal *et al.* (see **Table 6-1**) [53]. The IP method decreased the difference even further, finishing with a value after optimization of 11.847 Å, slightly shorter than the experimental parameter. The small discrepancy between the cell parameters evaluated by the GGA and IP was owing to longer Si-O distances in the case of the GGA compared to the IP method, on average 0.022 Å. A similar outcome has been reported for the optimization of the unit cell of zeolite MFI, where the GGA average value was 0.112 Å longer than the IP prediction [203].

Table 6-1. Optimized cell parameter a (Å), average and standard deviation of the Si-O bond distance (Å), O-Si-O and Si-O-Si angles (°). Elastic constants C_{11} , C_{12} and C_{44} (GPa), bulk modulus B (GPa), shear modulus G (GPa), B/G ratio, Young's modulus Y (GPa), Poisson's ratio σ and shear anisotropic factor A , obtained with the GGA and the IP method.

	GGA	IP	Exp.
a	11.950	11.847	11.857 ^c
Si-O	1.621 ± 0.007	1.599 ± 0.007	1.602 ± 0.006 ^c
O-Si-O	109.5 ± 0.9	109.5 ± 0.7	109.5 ± 0.4 ^c
Si-O-Si	148 ± 4	150 ± 4	150 ± 4 ^c
C_{11}	51	103	
C_{12}	27	60	
C_{44}	19	25	
B_{BM} ^a	42	–	22.1 ^d
B ^b	35	75	22.1 ^d
G	16	23	
B/G	2.2	3.3	
Y	42	58	
σ	0.30	0.37	
A	1.6	1.2	

^a Value obtained by fitting to the Birch-Murnaghan equation of state [170].

^b Value obtained using the Voigt's approximation [248].

^c Value from Ref [53]

^d Value for zeolite A, formula $[\text{Na}_{12}(\text{Al}_{12}\text{Si}_{12}\text{O}_{48})27\text{H}_2\text{O}]$, from Ref [249]

We calculated a bulk modulus B of 42 GPa by fitting the GGA-calculated energies of a set of fixed volume calculations to the Birch-Murnaghan equation [170],

decreasing to 35 GPa when employing the GGA-calculated elastic constants within the Voight equation (see **Table 6-1**) [248]. The IP method led to a value for B of 75 GPa. These results followed the same trend of the zeolite MFI, where a B of 18 GPa was evaluated by GGA, rising to 54 GPa with IP [203], with the GGA value being much closer to the experimental value of 18.2 GPa [171]. The validation of our results is more difficult in the case of pure-silica zeolite LTA because most of the experimental measurements provided in the literature come from zeolite-A, which has the same LTA framework but with a Si/Al ratio of 1 and loaded with 6 to 12 extra-framework cations per unit cell to compensate the negative charge of the framework. For instance, Arletti *et al.* have reported a value of 22.1 GPa for zeolite-A [249], whilst Niwa *et al.* have measured values between 25.3 and 34.4 GPa depending on the pressure transmitting medium [250]. Our calculated B is larger than the experimentally measured values, but this may be attributed to the modifications in bonding strengths when the Si/Al ratio changes from 1 to infinity, which makes the structure more resistant to deformations; an experimental benchmark using pure-silica LTA is necessary to validate our results.

The values of the calculated shear moduli (G), presented in **Table 6-1**, of 16 and 23 GPa for GGA and IP, respectively, mean that zeolite LTA has a relatively low resistance to plastic deformation [251,252]. Huang and Havenga have actually reported the reversibility of the pressure-induced amorphization of zeolite-A in the range of 15 to 25 kbar, although they showed that the presence of extra-framework cations is essential for recovering the crystalline structure after the deformation [253]. The G calculated in this study considered a pure-silica LTA without extra-framework cations, which should therefore make its G value larger than the one for zeolite-A.

At the same time, the ratio B/G measures the level of ductility (if high) or brittleness (if low) of a material, with the turning point between ductility and brittleness at approximately 1.75 [251]. We obtained values of 2.2 and 3.3 for B/G , using the GGA and IP method, respectively. Both types of calculations depict zeolite LTA as ductile, but considering that the larger value of IP should be due to its overestimation of B , we suggest that the result of the GGA should be more realistic.

The Poisson ratio σ is a measure of the ionic or covalent character of the bonds within the material. Values smaller than 0.1 are attributed to covalent bonding, whilst a ratio above 0.25 suggests ionic interactions [254]. The GGA and IP led to similar σ values of 0.30 and 0.37, respectively, with both methods well above 0.25. This result also validates the use of the Born model of ionic solids to describe the largely ionic zeolite structure [138].

We have also calculated the shear anisotropic factor A , which evaluates the level of anisotropy of the crystal for values smaller or larger than unity. In the present study, GGA had an A of 1.6, reducing to 1.2 in the case of IP. Accordingly, pure-silica LTA should show a significant degree of anisotropy according to the GGA. However, a previous report has shown that A may be overestimated by the GGA methodology, where a theoretical value of 1.34 is predicted for magnetite (Fe_3O_4) against an experimental measurement of 1.13 [255].

6.4 Ti-substituted Zeolite LTA

All T-sites are equivalent in zeolite LTA, which renders the single Ti substitution meaningless in terms of comparative analysis. Hence, we have examined the double substitution of Si by Ti using Boltzmann statistics. The unit cell with 24 TO_2 groups

was used for the GGA calculations, whilst an expanded supercell of $2 \times 2 \times 2$ was used with the IP method in order to complement the GGA results. **Figure 6-1** shows the Boltzmann distributions at 125 °C, which is the synthesis temperature used by Boal *et al.* to obtain the titanosilicate [53].

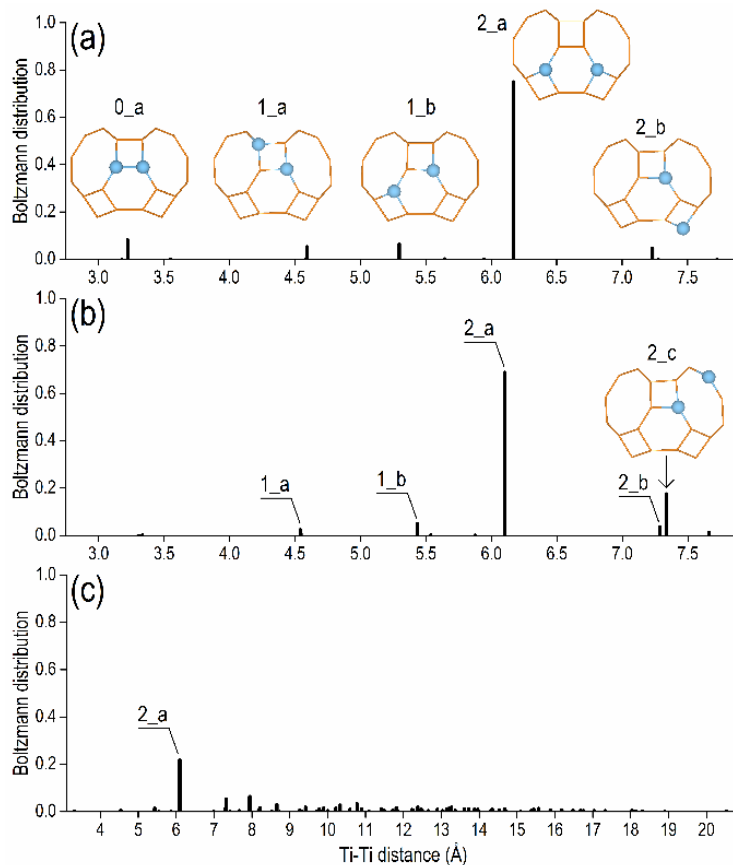


Figure 6-1. Boltzmann distributions at 125 °C for the double Ti-substituted zeolite LTA as a function of the separation between the two Ti atoms within the framework. Segments of the optimized structures are shown for the peaks with significant probability. (a) The GGA using a 72-atom unit cell, (b) the IP method using a 576-atom supercell and considering only double substitutions within the same unit cell out of eight available and (c) IP using a 576-atom supercell and considering the full set of double substitution along the supercell. The number within the label of each peak specifies the number of Si atoms that bridge the two Ti atoms, the letter is only to specify the order of appearance.

The GGA calculations identified five double Ti-substituted structures with significant probabilities out of twelve non-equivalent substitutions in the $1 \times 1 \times 1$ unit cell. Owing to its small size, only the arrangements Ti-Ti, Ti-Si-Ti and Ti-Si-Si-Ti

were obtained for this cell, where the **2_a** structure in **Figure 6-1a** was the one with the highest prevalence (the number in the label specifies the number of bridging Si atoms placed between the two Ti atoms). In **2_a** the two Ti atoms were evenly placed at opposite sides of the six-membered ring (6MR) of zeolite LTA (see **Figure 6-1a**), being separated by a distance of 6.2 Å. This ordering is similar to the one reported by Bare *et al.*, who used EXAFS to study the substitution of Sn in β -zeolite, and highlighted the non-random substitution of Sn in the zeolite framework [256]. We did not consider the presence of the structure-directing agent (SDA) in this thesis and therefore, the stability of the 6MR substitution may not only be related to the employed SDA, but also to the capacity of this configuration to minimize the framework deformations. Other important structures placed both Ti atoms in the same D4R, labelled as **0_a** and **1_a** in **Figure 6-1a**, with Ti-Ti distances of 3.2 and 4.6 Å, respectively, and in two different D4Rs, labelled as **1_b** and **2_b** in **Figure 6-1a**, with Ti-Ti distances of 5.3 and 7.2 Å, respectively.

We generated two different Boltzmann distributions for the IP method. The first one, shown in **Figure 6-1b**, only considered the substitutions within the same unit cell, despite using a $2 \times 2 \times 2$ supercell, to allow a direct comparison with the GGA results. The second distribution used the full spectrum of double substitutions (91 in total) and is shown in **Figure 6-1c**. A close agreement between the IP and GGA profiles can be noted from the comparison of **Figure 6-1a** and **6-1b**, regardless of the difference in level of theory and cell size. Again, **2_a** was by far the most stable structure, although the intensity of **0_a** decreased to almost zero and an additional configuration labelled as **2_c** arose (see **Figure 6-1b**). The full spectrum of double substitution shown in **Figure 6-1c** confirmed once more that **2_a** is the most stable arrangement when two Ti are placed in the zeolite framework. In **Figure 6-1c**, **2_a**

was compared against structures with Ti-Ti separations of more than 15 Å, which can be considered as two fully isolated species.

In the present thesis, we are not primarily concerned about the absolute stability of each type of substitution, but instead we have compared the relative stability between single and double substitutions by using the following equation:

$$\Delta_n = E(Ti_nLTA) + (n - 1)E(LTA) - nE(Ti_1LTA) \quad (6-6)$$

where $E(Ti_nLTA)$ is the energy of the n Ti-substituted zeolite, $E(LTA)$ is the energy of the pure-silica zeolite and $E(Ti_1LTA)$ is the energy of the single Ti-substituted zeolite. This equation can be interpreted as the energetics of a process that moves n Ti atoms from n single substituted unit cells to a sole unit cell, leaving the other $(n - 1)$ as pure-silica frameworks. By using (6-6) with the GGA energies and $n = 2$, the calculated values of Δ_2 were -11, -9, -8, -18 and -7 kJ/mol for the substitutions **0_a**, **1_a**, **1_b**, **2_a** and **2_b**, respectively. The other seven substitutions yielded positive values. This means that the double Ti substitutions represented in **Figure 6-1a** are more favourable than the single substitution per $1 \times 1 \times 1$ unit cell. The IP method showed equivalent outcomes. These results are different from a similar analysis by Yang *et al.*, who studied Ti substitution in β -zeolite by DFT and found that the single substitution is more stable than the double substitution of Ti in the 6MR [257]. Nevertheless, this apparent discrepancy may be the result of the topology of the 6MR: the ring is planar in LTA whilst it is bent in β -zeolite, which translates into different capacities to support framework distortions.

Table 6-2. Summary of average values and standard deviations of the T-O bond distances (Å), O-T-O and T-O-T angles (°) in the LTA structure (T=Si and Ti) obtained with the GGA and the IP method. The energy difference between the conduction and the valence bands Δ_{LUMO} (eV) obtained with the GGA is also listed for the electronic calculations.

	Si-O	O-Si-O	Si-O-Si	Ti-O	O-Ti-O	Si-O-Ti	Ti-O-Ti
GGA							
1Ti	1.622 ± 0.008	109.0 ± 1.0	148 ± 7	1.80 ± 0.01	109 ± 2	140 ± 10	
0_a	1.623 ± 0.009	109.0 ± 1.0	146 ± 9	1.81 ± 0.01	109 ± 2	150 ± 10	126
2_a	1.622 ± 0.009	109.0 ± 1.0	147 ± 9	1.81 ± 0.01	109 ± 2	144 ± 10	
IP							
1Ti	1.599 ± 0.008	109.5 ± 0.8	150 ± 4	1.76 ± 0.02	109 ± 2	150 ± 4	
0_a	1.599 ± 0.008	109.5 ± 0.9	150 ± 4	1.76 ± 0.02	109 ± 2	150 ± 2	146
2_a	1.599 ± 0.008	109.5 ± 0.9	150 ± 4	1.76 ± 0.02	109 ± 2	149 ± 5	

We considered the pure-silica LTA, the single Ti-substituted LTA and configurations **0_a** and **2_a**, as a fair representation of the structural diversity, and hence, we have only used these structures to continue the analysis in this thesis.

Table 6-2 shows the structural parameters of the Ti-substituted zeolites. The Si-O bond length and the O-Si-O and Si-O-Si angles of the Ti-substituted zeolite LTA did not manifest significant modifications when compared to the pure-silica structure. At the same time, the GGA tended to give longer Ti-O bonds when compared to the IP method, by an average of 0.04 to 0.05 Å, which were also longer than the GGA-calculated Si-O bond length by approximately 0.2 Å. The average Si-O-Ti angles of the single Ti-substituted structure and **2_a**, tended to be less opened than the equivalent Si-O-Si values when calculated with GGA, by 3 to 8°, whilst the opposite outcome was observed for **0_a**, where both Ti atoms were located in the same D4R. The GGA **0_a** structure also had an additional feature, i.e. the Ti-O-Ti angle was 18° smaller than the equivalent angle in the pure-silica LTA. This reduction was due to the simultaneous increase of the two Ti-O bonds, which forced the bridging O atom away from the imaginary line that connects both Ti atoms, in consequence reducing

the Ti-O-Ti angle. In contrast, the IP method did not show marked differences among the angles Si-O-Si, Si-O-Ti and Ti-O-Ti (see **Table 6-2**).

6.5 Electronic Structure

The unoccupied electronic band of lowest energy (or LUMO for the sake of consistency with the term used in the literature) provides a measure of the character of the active site as a Lewis acid, where the lower the LUMO energy is the more active the acid site [230]. The electronic charge density associated with the LUMO of the pure-silica LTA is mainly concentrated inside the D4R, as shown in **Figure 6-2a**. Once the Ti substitution takes place, the electron density is projected outside the D4R, towards the α - and β -cages, and hence more accessible to incoming reactants. The difference between the energy of the LUMO, averaged over the set of k-points, and the Fermi energy (Δ_{LUMO} in **Table 6-3**) was 5.86 eV for the pure-silica LTA, 4.47 eV for the single-substituted LTA, 4.23 eV for **0_a** and 4.30 eV for **2_a**. These values show that the single Ti substitution reduces the energy of the LUMO by more than 1 eV. The double Ti substitution may further decrease this energy, but we did not observe a monotonic behaviour in the correlation between Δ_{LUMO} and the Ti-Ti distance. For Ti-Ti distances below 5.0 to 6.0 Å we observed fluctuation in Δ_{LUMO} , and this parameter should thus be treated with some reservation.

Table 6-3. The energy difference between the conduction and the valence bands Δ_{LUMO} (eV) obtained with the GGA.

	Δ_{LUMO}
pure-silica LTA	5.86
single Ti subst.	4.47
0_a	4.23
2_a	4.30

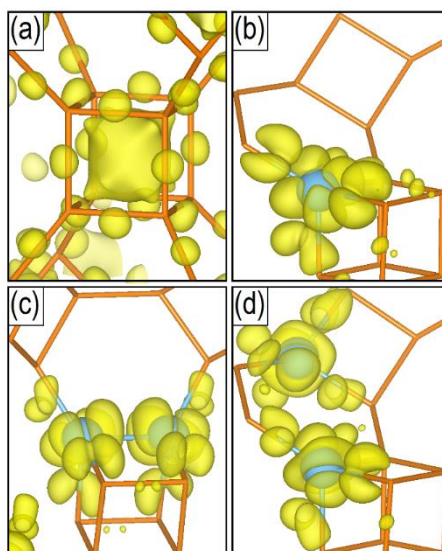


Figure 6-2. Representation of the isosurfaces of the electronic charge density associated with the unoccupied electronic band of lowest energy of relevant structures (0.0007 bohr^{-3}). (a) pure-silica LTA, (b) single Ti substitution, (c) 0_a and (d) 2_a. The framework O atoms are deleted for clarity, Ti atoms are represented by light blue balls and Si atoms by orange sticks.

6.6 Vibrational Analysis

Infrared (IR) spectroscopy is a powerful experimental technique that provides structural information specific to each material. The theoretical simulation of the IR spectrum enables the correlation of variations in the spectrum profile with explicit modifications in the material structure without undesired interferences, which then may complement and help to understand the experimental measurements.

Table 6-4. Vibrational frequencies (cm^{-1}) of the simulated IR spectra of **Figure 6-3.**^a

IP	GGA		Exp. ^b	GGA		
	pure-Si			1Ti	0_a	2_a
						1168 w
						1143 w
928 s	1073 s	1096 s		1067 s	1063 s	1062 s
				978 w	972 m	973 m
						905 w
						755 w
627 w	597 w	621 w		593 w	591 w	585 w
464 w	449 w	477 m		450 w	452 w	446 w
384 w	376 w	407 m		375 w	375 w	374 w

^a Weak (w), medium (m) and strong (s) intensity

^b From Ref [258]

We have simulated the theoretical IR spectrum of the pure-silica LTA and validated it against the equivalent experimental report by Huang and Jiang [258]. **Figure 6-3** shows the simulated IR spectra using the GGA and the IP methods, with the vibrational frequencies of the main bands listed in **Table 6-4**. The theoretical IR spectra of pure-silica LTA present four main bands for both the IP method and the GGA, resembling the experimental spectrum within the limits of the theoretical approximations [258]. The most intense signal, located at 928 cm^{-1} for IP and 1073 cm^{-1} for GGA, corresponds to the asymmetric Si-O stretching, which has an experimental value of 1096 cm^{-1} [258], i.e. very close to the GGA value. The other three bands are located within the range 650 to 400 cm^{-1} , reproducing the experimental signals with deviations of -31 to $+6\text{ cm}^{-1}$ for both the IP method and the GGA. Within this range, the experimental bands at 621 and 477 cm^{-1} are related to the D4R, whilst the signal at 407 cm^{-1} is associated with the 6MR [258]. A close inspection of the calculated vibrations in **Table 6-4** for the pure-silica LTA indicates to a regular underestimation of the frequencies compared to experiment, a trend that has been noted previously by Huang and Jiang [258].

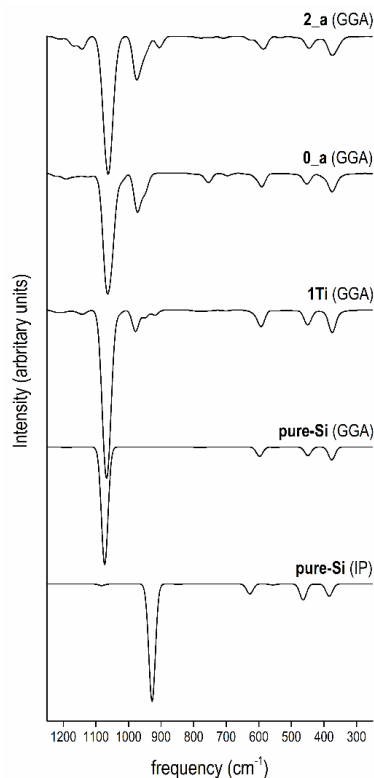


Figure 6-3. Simulated infrared spectra of relevant structures (from bottom to top): pure-silica LTA (pure-Si), LTA with a single Ti substitution (1Ti), configuration 0_a and configuration 2_a. The labelling of each spectrum contains within parenthesis the level of theory with which it was simulated: the GGA or the IP method.

The GGA was shown to be better than the IP method in reproducing the experimental spectrum of pure-silica LTA, and therefore we have only analysed single and double Ti substitutions by GGA-simulated IR spectra. In addition, the IP method manifested a lack of sensibility towards the Ti substitution, showing practically no variations when one or two Ti atoms were included within the zeolite framework.

The single Ti substitution causes a red-shift in the band of the asymmetric Si-O stretching by 6 cm^{-1} , which coincides with the softening of this band observed in experiment when Si atoms are replaced by Al, shifting by almost 90 cm^{-1} from pure-silica LTA to zeolite A [258]. The stretching for Ti-O appears at 978 cm^{-1} with lesser shoulders at 951 and 920 cm^{-1} . This signal is shifted with respect to the asymmetric Si-O stretch by 91 cm^{-1} , corresponding to the weaker and longer bond length of Ti-

O when compared to Si-O. The rest of the spectrum does not show significant variations after the single substitution.

The double substitution represented by structure **0_a** in **Figure 6-1**, enhances the intensity of the asymmetric Ti-O stretching as expected, and produces an additional weak band at 755 cm^{-1} . The signal at 755 cm^{-1} is related to the stretching of the Ti-O bond associated with the O atom bridging the two Ti atoms. As described above, the angle Ti-O-Ti in **0_a** decreases when compared with the pure-silica value, moving the bridging O atom further away from the axis linking the two Ti atoms, which, combined with longer Ti-O bonds, makes the Ti-O(-Ti) stretching 217 cm^{-1} weaker than Ti-O(-Si). The band at 755 cm^{-1} disappears again in the spectrum of structure **2_a**, where the two Ti atoms are separated by two Si atoms, in agreement with our interpretation.

The spectrum of **2_a** presents weak peaks above the asymmetric Si-O band, at 1168 and 1143 cm^{-1} . These signals are related to Si-O(-Si) stretching modes associated with the D4R where the Ti atoms are substituted. Equivalent signals tend to appear in the spectrum of the single Ti-substituted LTA, but their intensities are very weak, almost negligible (see **Figure 6-3**). However, the spectrum of structure **0_a** lacks those bands, which may help to differentiate structures Ti-(Si)₀-Ti from those with a configuration Ti-(Si)_{n>0}-Ti. Additionally, narrower Ti-O-Si angles cause softening of the Ti-O(-Si) stretching by 68 cm^{-1} , producing a very weak band at 905 cm^{-1} in the spectrum of **2_a**. For instance, while the Ti-O-Si angle is approximately 165° for the band at 973 cm^{-1} , it is reduced to 138° for the signal at 905 cm^{-1} .

6.7 Hydration of Ti-substituted Zeolite LTA

The Lewis acidity can be probed by studying the adsorption strength of small molecules at the active sites [230,257,259]. We have chosen water as a probe molecule owing to its presence during the synthesis of the zeolite [53], which may also influence the distribution of Ti atoms along the framework positions. The pure-silica LTA, the single Ti-substituted LTA, and the **0_a** and **2_a** structures were used to analyse the adsorption of water.

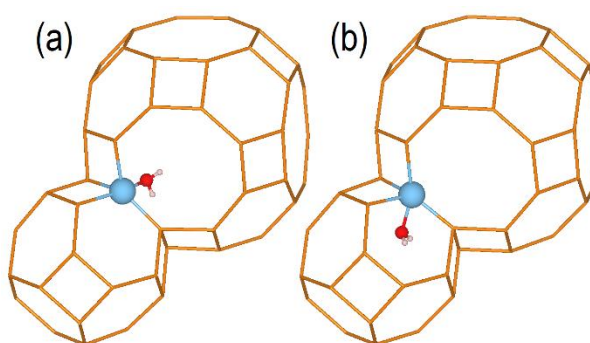


Figure 6-4. Representation of the adsorption of water in (a) the α -cage and (b) the β -cage, taking as an example the optimized structures of single Ti-substituted LTA. The framework O atoms are deleted for clarity, the water O atom is represented by a red ball, H atoms by white balls, Ti atoms by light blue balls and the silicon atoms by orange sticks.

The adsorption of water in the pure-silica LTA released average adsorption energies of 20 and 31 kJ/mol, depending whether the loading took place in the α -cage or in the β -cage, respectively (see **Figure 6-4**). The contribution of dispersion corrections accounted for 66% and 69% of the adsorption energies, respectively. The water molecule did not have a preferred adsorption site, as expected from its interaction with a completely siliceous framework [257]. The Ti substitution increased the strength of the interaction of water with the zeolite. In the case of the single substitution, the average adsorption energies were evaluated at -37 and -50 kJ/mol, with Van der Waals (VdW) contributions of 46% and 47%, for adsorption in the α -

cage and β -cage, respectively. The effect of dispersion forces has decreased from the pure-silica to the Ti-substituted framework due to the direct interaction between water and Ti, which has more of a chemisorption character. The addition of a second Ti atom, in the form of structures **0_a** and **2_a**, did not lead to major variations from what was observed for the single substitution. The adsorption energy in the α -cage remained between -34 and -36 kJ/mol, again increasing to -47 kJ/mol when the loading occurred in the β -cage. In the particular case of **0_a**, the water interaction with one of the Ti atoms opposite to the bridging O atom showed an adsorption energy of -43 kJ/mol, as shown in **Figure 6-5**, even though it was loaded in the α -cage, where the energies tended to be at least 5 kJ/mol lower. This increase was due to the higher capacity of the Ti-O-Ti segment to accommodate structural distortion than the Si-O-Ti segment. The average distance between the water O atom and the Ti remained within a narrow range of 2.3 to 2.5 Å for every analysed structure.

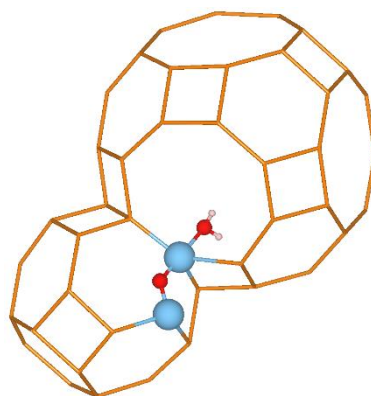


Figure 6-5. Representation of the optimized structure for the adsorption of water on **0_a** opposite to the bridging O between the two Ti atoms. This adsorption takes place from loading in the α -cage. The framework O atoms are deleted for clarity (the only exception is the bridging O atom between the two Ti atoms), water O atoms are represented by red balls, H atoms by white balls, Ti atoms by light blue balls and the Si atoms by orange sticks.

We have also analysed the possibility of water dissociation on the Lewis site by breaking one of the O-H bonds of water and transferring the proton to the TiO_4

tetrahedron. However, in all cases, either the proton returned to the OH group binding the Ti atom, re-forming a water molecule, or the structure was more than 60 kJ/mol less stable than the non-dissociated system. Water dissociation was more likely when a two-membered ring (2MR) was formed, where both OH groups bound simultaneously to the Ti atom and its nearest-neighbour Si atom from a different D4R, as shown in **Figure 6-6b**. We did not observe the formation of 2MRs when the Ti and the Si atoms belonged to the same D4R. We attribute this outcome to the inability of a single D4R to accommodate the distortions provoked by the formation of the 2MR. After observing the importance of the 2MR formation, we also optimized the pure-silica 2MR (**Figure 6-6a**) and the double Ti-substituted 2MR (**Figure 6-6c**) in order to analyse the dependence of the 2MR stability on the extent of the Ti substitution (for relative energies of the process, see **Table 6-5**).

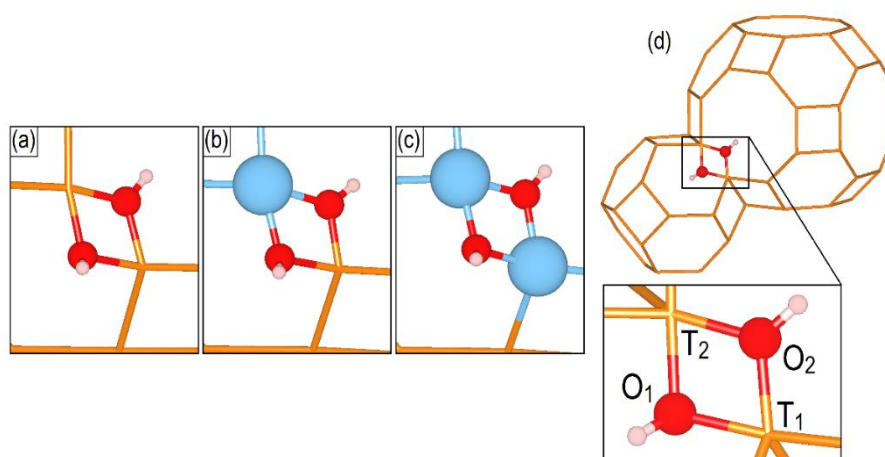


Figure 6-6. Close-ups of the optimized structures of the two-membered rings (2MR) with different degree of Ti substitution. (a) 2MR for pure-silica zeolite, (b) 2MR for single Ti-substituted zeolite, and (c) 2MR for double Ti-substituted zeolite. (d) Location of the 2MR within the framework using the optimized structure of pure-silica zeolite as an example, the close-up specifies the labels used to distinguish the different atoms of the 2MR. The framework O atoms are deleted for clarity, the O atoms of the 2MR are represented by red balls, H atoms by white balls, Ti atoms by light blue balls and the Si atoms by orange sticks.

The pure-silica 2MR (labelled as 2Si-2MR) has been experimentally detected by Hunger *et al.* using magic-angle spinning nuclear magnetic resonance (MAS-NMR) [260]. The authors observed that when tetrapropylammonium (TPA), acting as SDA, was used to synthesize zeolite ZSM-5, internal silanols were formed as defects in a concentration of up to 8%. Sokol *et al.*, employing DFT under periodic boundary conditions, found a relatively low energy requirement for the hydrolysis of a siloxane bridge with the subsequent formation of 2Si-2MR [261]. They suggested that the 2MR may undergo dehydrogenation, creating triplet peroxide species, which transform into a singlet peroxy bridge with an O-O distance of approximately 1.58 Å. The authors further proposed that the migration of these peroxy bridges could be the reason for the increase of the Brønsted and Lewis acidity, which makes the redox chemistry of these materials even more complex [261].

Table 6-5. T-O distance (Å) (T = Si and Ti), O-O distance (Å), O-H distance (Å) and relative energy against the non-dissociated water (kJ/mol) of different 2MRs.

	2Si-2MR	Si,Ti-2MR	2Ti-2MR
Si-O ₁ ^a	1.861, 1.866	1.859	–
Si-O ₂ ^a	1.799, 1.795	1.736	–
Ti-O ₁	–	2.010	1.991, 2.036
Ti-O ₂	–	2.043	2.007, 1.950
O ₁ -O ₂	2.147	2.254	2.422
H ₁ -O ₁	0.971	0.971	0.971
H ₂ -O ₂	0.973	0.971	0.970
Rel. E. ^a	+108 (-31)	+50 (-52)	+15 (-71)

^a When two values are given for the same entry of the T-O distance, the first number refers to the distance T₁-O and the second to T₂-O, following the labelling in **Figure 6-6**

^b The adsorption energy of non-dissociated water is stated within parenthesis.

In this study, the dissociation of the adsorbed water that led to the formation of 2Si-2MR increased the energy of the system by +108 kJ/mol (see **Table 6-5**). The Si-O bond lengths of 2Si-2MR remained between 1.799 and 1.866 Å, with an O₁-O₂ distance of 2.147 Å, in agreement with previous calculations [261]. The inclusion of

one Ti atom within the 2MR (labelled as Si,Ti-2MR) increased the stability of the structure, which was apparent from the reduction of the energy versus the system with non-dissociated water. In this case, the Si,Ti-2MR was +50 kJ/mol less stable than the system with non-dissociated water, representing a marked decrease in energy difference when compared to the value of +108 kJ/mol found for 2Si-2MR (see **Table 6-5**). Nevertheless, Si,Ti-2MR was still hardly stable, with a mere relative energy of -2 kJ/mol against the standard of water in the gas phase plus the bare zeolite without adsorbate. In this regard, it has been reported that Si,Ti-2MR is the less stable configuration when compared to models that reflect different levels of hydration and inversion of the tetrahedra SiO₄ and TiO₄ such as tripodal, tetrapodal and bipodal configurations [262].

When we considered the 2MR formed by two Ti atoms (labelled as 2Ti-2MR), the stability of 2Ti-2MR increased significantly. As shown in **Table 6-5**, 2Ti-2MR was only 15 kJ/mol less stable than the system with non-dissociated water, in contrast to the values of +108 and +50 kJ/mol for 2Si-2MR and Si,Ti-2MR, respectively. In addition, the adsorption energy of dissociated water forming the 2Ti-2MR structure was -56 kJ/mol compared to the unhydrated system plus gaseous water separately, i.e. more energetically favourable than the adsorption of non-dissociated water in the structures **0_a** and **2_a**. At the same time, the adsorption of non-dissociated water, which served as a precursor for the formation of 2Ti-2MR, had a value of -71 kJ/mol, denoting a significant increase in adsorption strength when compared to equivalent double Ti-substituted structures in the form of **0_a** and **2_a**. This increase in binding was due to the simultaneous interaction of water with the two Ti atoms, at a position where the electronic charge density associated with the LUMO completely surrounded the molecule (see **Figure 6-7**). The calculated distances between the

water O atom and the two Ti atoms were 2.454 and 2.446 Å, showing that the molecule was evenly shared between the two Lewis centres. The Ti configuration that allowed the formation of the 2Ti-2MR (labelled as **0_b** in order to follow the same scheme of **Figure 6-1**) had a probability of 0.01% using the Boltzmann distribution. However, considering the stabilizing effect that water may exert on this configuration during the synthesis process, the probability of finding the **0_b** configuration should increase. As such, the presence of the **0_b** configuration in zeolite LTA could have important consequences for the performance of this material as a catalyst for redox reactions: two Ti atoms, at close distance from each other, and with the capacity to interact simultaneously with the same molecule, may adsorb and stabilize more effectively peroxide species than single Ti-substituted frameworks [243].

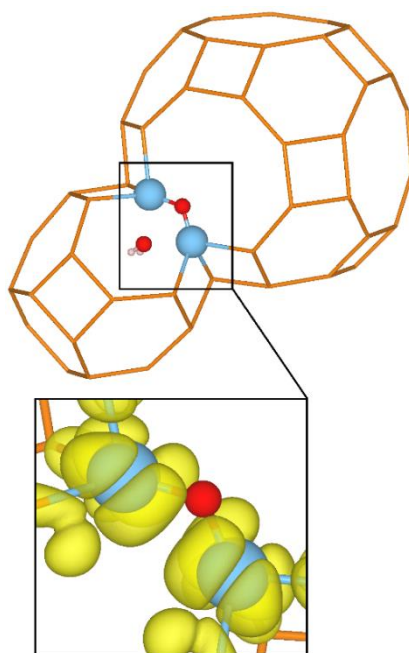


Figure 6-7. Optimized structure for the adsorption of water forming 2Ti-2MR after the O-H bond dissociation. The close-up shows the LUMO of the material. The framework O atoms are deleted for clarity (except the bridging O between the two Ti atoms), the water O atom is represented by red balls, the H by white balls, the Ti atoms by light blue balls and the Si atoms by orange sticks.

We have simulated the IR spectra of the 2MRs with the GGA methodology and compared them with the profiles belonging to the equivalent structures without adsorbates, as shown in **Figure 6-8**. The main feature related to the formation of the 2MRs, which may serve to identify this structure in any experiment, is the splitting of one of the bands associated with the pure-silica D4R. For instance, the signal at 598 cm^{-1} in the pure-silica spectrum evolves into two weak bands at 604 and 569 cm^{-1} after the 2Si-2MR formation (indicated by small vertical arrows in the spectra). The same tendency is followed by the single Ti-substituted structure, where two weak bands at 604 and 571 cm^{-1} are observed for Si,Ti-2MR. The spectrum of 2Ti-2MR shows a similar splitting but it tends to be slightly larger than in the previous two cases. The separation between the two weak bands is 35 and 33 cm^{-1} for 2Si-2MR and Si,Ti-2MR, respectively, increasing to 54 cm^{-1} for 2Ti-2MR.

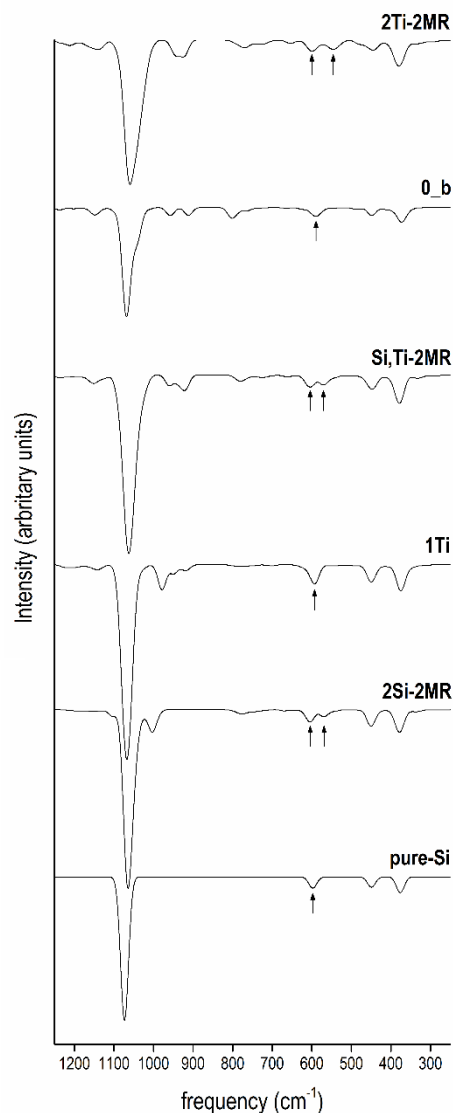


Figure 6-8. Simulated IR spectra of the different 2MRs and their comparison with their equivalent structures without adsorbate. (From bottom to top) Pure-silica LTA (**pure-Si**), and **2Si-2MR**; single Ti-substituted LTA (**1Ti**) and **Si,Ti-2MR**; double Ti-substituted, with the Ti configuration shown in **Figure 6-7** and labelled as **0_b**, and **2Ti-2MR**. The splitting of one of the bands associated with D4R is marked with vertical arrows.

6.8 Chapter Conclusions

We have performed density functional theory and interatomic potential-based calculations to study the pure-silica zeolite LTA and its Ti-substituted forms. The calculated mechanical properties of the pure-silica LTA predict that this material is

more rigid than zeolite-A, which has the same framework type but with a Si/Al ratio of 1. The IP method tends to overestimate the value of the elastic moduli compared to the GGA, which trend agrees with previous calculations on zeolite MFI.

The energetics of the Ti-substituted LTA suggests that the addition of a second Ti atom within the framework, at close distance from the first Ti, is a favourable process. In fact, both the GGA and the IP method predict that the global minimum corresponds to a double Ti substitution in a six-membered ring, with the two Ti atoms symmetrically opposing each other with a configuration Ti-(Si)₂-Ti.

The interaction of a water molecule with Ti has a calculated adsorption energy of -32 to -52 kJ/mol, where the adsorption in the β -cage is slightly stronger than in the α -cage, by 2 to 6 kJ/mol. The direct dissociation of water is only favoured when it leads to the formation of a two-membered ring (2MR) between T-sites of different D4Rs. The stability is especially high for the 2MR Ti-(OH)₂-Ti, with an energy that is comparable to non-dissociated water adsorbed at the Ti sites.

The GGA-simulated infrared spectrum of the pure-silica LTA shows good agreement with experimental measurements, and it is capable of reproducing the four main bands within an error of -30 to -20 cm⁻¹. The Ti substitution causes the occurrence of new weak signals between 1200 and 700 cm⁻¹, depending on the configuration of the Ti atoms. The main feature related to the formation of the 2MRs is the splitting of the weak band at approximately 600 cm⁻¹, which is associated with the D4R building unit, into two weak bands that are separated by 33 to 54 cm⁻¹.

Chapter 7 Conclusions and Future Work

7.1 Summary and Conclusions

This thesis has pursued the study of layered zeolite MFI and titanium-substituted zeolite LTA using computational methods.

Regarding the analysis of layered MFI, in Chapter 3, we examined the structural features of this morphology and comparing it to the conventional, three-dimensional zeolite MFI. The crystalline structure of the MFI nanosheet is not affected by the thickness of the slab, which can be as thin as a single unit cell along the *b* direction. The average values and spanning ranges of the Si-O distances and the O-Si-O and Si-O-Si angles retained the same trends in both the MFI slab and bulk. The structural distortions of the framework caused by the aluminium substitution were also practically undistinguishable between the slab and the bulk. These results prompted us to confirm that MFI nanosheets are very stable materials as observed in the experiment.

The MFI slabs were capped with silanols groups due to the saturation of the cleaved Si-O bonds with hydroxy groups. The silicon atom of a silanol group can be replaced by an aluminium and this substitution provokes the destabilization of the group, which dehydrates overcoming a low energy barrier (< 20 kJ/mol) producing a three-coordinated Lewis acid site with a water molecule adsorbed on it. The Lewis site is more thermodynamically stable than the aluminium-substituted silanol, by 12 to 25 kJ/mol. This knowledge was used after in Chapter 5 to investigate the tautomerization of phenol and catechol catalysed by Lewis acid sites.

The behaviour of Brønsted acid (BA) sites, located at the internal and external surfaces of zeolite MFI was also another interesting topic that we treated in Chapter 4. Trimethylphosphine oxide (TMPO) is usually used to probe the strength of the BA sites in zeolites. The molecules are adsorbed on the material and the extent of the proton transfer from the zeolite to the phosphine is measured by the ^{31}P NMR: the larger the ^{31}P chemical shift the stronger the acid. Nevertheless, the distribution of BA site within the zeolite framework is not homogeneous since the experiment finds three different types of strength, which are classified as *very strong*, *strong* and *weak*. In addition, the distribution of acid strengths at the internal surface differs from the distribution observed at the exterior of the zeolite, where only *very strong* and *weak* acidities are sensed.

We were able to propose a reasonable explanation to the experimental observation by using geometrical relaxation followed by molecular dynamics simulations. We based our analysis on the different types of basic centres that can compete for the proton: (i) oxygen atoms of the TMPO molecules $\text{O}_{(\text{P})}$, (ii) framework oxygen atoms that bind the aluminium $\text{O}_{(\text{Al})}$ and (iii) framework oxygen atoms that do not bind the aluminium $\text{O}_{(\text{Si})}$. The order of basic strength is the following: $\text{O}_{(\text{P})} > \text{O}_{(\text{Al})} > \text{O}_{(\text{Si})}$. Assuming that the proton is shared by a pair formed by these centres, we can name three pairs: $\text{O}_{(\text{P})}\text{-H}\text{-O}_{(\text{P})}$, $\text{O}_{(\text{P})}\text{-H}\text{-O}_{(\text{Al})}$ and $\text{O}_{(\text{P})}\text{-H}\text{-O}_{(\text{Si})}$. Given the difference in basic strength that exists between the centres of each pair, and the criterion that shorter $\text{O}_{(\text{P})}\text{-H}$ distances correspond to stronger acidity as sensed by ^{31}P NMR, the *very strong*, *strong* and *weak* acids are directly associated to the pairs: $\text{O}_{(\text{P})}\text{-H}\text{-O}_{(\text{Si})}$ (*very strong*), $\text{O}_{(\text{P})}\text{-H}\text{-O}_{(\text{Al})}$ (*strong*) and $\text{O}_{(\text{P})}\text{-H}\text{-O}_{(\text{P})}$ (*weak*). This is an important result that may help to understand molecular diffusion and aggregation within the pore system of zeolites based on ^{31}P NMR data. The pair $\text{O}_{(\text{P})}\text{-H}\text{-O}_{(\text{Al})}$ is the standard interaction,

expected from the simple adsorption of a TMPO molecule on the BA site, and the pairs $O_{(P)}-H-O_{(P)}$ and $O_{(P)}-H-O_{(Si)}$ are only obtained if a TMPO is able to migrate from the acid site carrying the acid proton with it and establish interactions with nearby TMPO molecules or other framework oxygens not binding the aluminium atom. We conclude that this migration can only take place if the $O_{(P)}-H-O_{(Si)}$ interaction is perturbed strongly enough by the agglomeration of other TMPO molecules or by an increase of temperature. This idea is also supported by the experimental observation that *strong* acids (the pairs $O_{(P)}-H-O_{(Al)}$) are not detected at the external surface of the zeolite, leaving only *very strong* and *weak* ones. The interaction $O_{(P)}-H-O_{(Al)}$ should be much more easily perturbed at the external surface, where the pair is directly exposed to high amounts of incoming TMPO molecules, and its movement is not restricted by the pore system.

As it was mentioned above, Lewis acid sites should be more abundant at the external surface of zeolites due to the dehydration of aluminium-substituted silanols. We used this feature to investigate in Chapter 5 the possible tautomerization of phenol and catechol catalysed by the zeolite. This analysis was based on the fact that zeolites are usually used as supports of metal nanoparticles during the hydrodeoxygenation of organosolv lignin or lignin-derived compounds. The nanoparticle sizes normally exceed the diameter of the micropore apertures, and therefore they should be deposited at the external surface of the support and close to Lewis active sites. In addition, there are experimental reports stating that the tautomerization may be an intermediate step during the hydroprocessing of phenolic monomers. Hence, if the Lewis sites of zeolites can easily catalyse the tautomerization, the role of this material could not only be limited to the dehydration of hydrogenation products.

We observed that phenol and catechol tend to adsorb with a co-planar configuration through the phenolic oxygen atom. The energy barrier of the $O_{\text{ph}}\text{-H}_{\text{ph}}$ bond dissociation is not bigger than 55 kJ/mol, which makes this step perfectly attainable under mild-temperature conditions. The product of the dissociation is thermodynamically less stable, although it can freely rotate around the $O_{\text{ph}}\text{-Al}$ axis producing a more stable configuration that decreases the probability of phenol regeneration by re-forming the $O_{\text{ph}}\text{-H}_{\text{ph}}$ bond. This rotation is not energetically demanding, with an energy barrier that ranges from 0 to 12 kJ/mol. The rotation also allows a more favourable orientation for the transfer of the H_{ph} atom to one of the carbon atoms at *ortho* position from the phenol group. This last step, the formation of the C-H_{ph} bond, requires an activation energy smaller than 30 kJ/mol, which is lower than the initial dissociation of the $O_{\text{ph}}\text{-H}_{\text{ph}}$ bond. Following these three steps – $O_{\text{ph}}\text{-H}_{\text{ph}}$ bond dissociation, rotation and C-H_{ph} bond formation – the tautomerization is reached, and encourages us to conclude that the Lewis acid sites of zeolite are able to effectively catalyse the tautomerization.

The tautomerization of phenol and catechol does not exactly follow the same trends. Catechol has two OH groups attached to the benzene ring at ortho positions from each other, and the presence of the second OH group favours a non-planar adsorption if it is followed by a fast dissociation of one of the $O_{\text{ph}}\text{-H}_{\text{ph}}$ bonds, finishing with a bidentate binding to the aluminium atom. Furthermore, the tautomerization in catechol selectively involves the carbon atom at ortho position from the first OH group but not binding the second OH. This happens because the second OH group always tends to stay on the plane of the benzene ring, even if the hybridization of its carbon atom changes from sp^2 to sp^3 , which destabilizes the structure.

Finally, Chapter 6 deals with the titanium-substitution of zeolite LTA. We initially analysed the mechanical properties of pure-silica LTA, concluding that this material is less flexible than zeolite A, which has the same framework type but with a Si/Al ratio of 1. Moreover, we observed once more that interatomic potential-based calculations overestimate the elastic parameters compared to density functional theory results. In addition, we observed that it is more energetically favourable the double substitution of titanium over the single substitution, with the two Ti atoms separated by less than 7 Å. In fact, the global minimum consisted in the double substitution of a single 6MR of the LTA structure with a configuration Ti-(Si)₂-Ti.

As expected, a water molecule adsorbs preferentially on Ti, and its direct dissociation on this site is not favoured except when a 2MR is formed, in which case the two T-sites that form the ring must belong to different 4DRs. The stability of the 2MR increases with the titanium content as: Si-(OH)₂-Si < Si-(OH)₂-Ti < Ti-(OH)₂-Ti. The 2MR Ti-(OH)₂-Ti can be as stable as the simple adsorption of a non-dissociated water molecule on the Ti site, which points out the high stability of this structure.

7.2 Future Work

Here, we examine the additional work that could be developed from the results and methodologies discussed in Chapters 3, 4, 5 and 6.

In Chapter 3, we have only studied the (010) surface of zeolite MFI using the slab model, where the defects were limited to aluminium substitutions. This could be further expanded by analysing the stability and properties of double or higher aluminium substitutions in T-sites exposed at the external surface. In addition, other

elements different from aluminium could be utilized for the intra-framework substitutions, such as Sc, Fe and Ga to mention few examples. Another essential point is the counter-ion. We have restricted our research to H^+ , although transition metal cations can be also introduced. Extra-framework cations at the interior of the zeolite structure have been extensively studied in the literature. Nevertheless, the presence of these cations at the external surface could provide attractive applications that are worth to investigate.

Silanol nests are defects that should have a high prevalence at the external surface due to its exposure to degrading agents. Silanols nests originate from T-sites vacancies that leave three silanol groups at short distance from each other that establish H-bonds. There are 12 non-equivalent T-sites per unit cell exposed at the external (010) surface of zeolite MFI (assuming a complete pentasil layer). A silanol nest could be formed at each of these 12 T-sites by removing the silicon atom and saturating the broken Si-O bonds with H atoms. Thereafter, the analysis of the relative stability of these 12 silanol nests and their interaction with probe molecules could be performed.

Finally, zeolite MFI is not the only framework with a layered morphology. The MWW framework also provides two-dimensional structures and thus everything said here for MFI can be applied to MWW, generating a considerable amount of work to be done.

In Chapter 4, we proposed a methodology based on geometry relaxations followed by short molecular dynamics of a system formed by trimethylphosphine oxide adsorbed on the Brønsted site to analyse the acid strength of zeolites. In contrast to previous models that use adsorption energies or proton affinities, this scheme is

centred on following the proton transfer from the zeolite to the probe molecule, and judging the acid strength according to the extent of this transfer. Nevertheless, we have only investigated a Brønsted acid site formed by the aluminium substitution in the T2 site and binding the counter H^+ ion to the O1 atom. Hence, it would be important to extend this study to the 12 possible Brønsted acids that can be formed in zeolite MFI considering only non-equivalent single aluminium substitutions. The results derived from these simulations would provide additional information regarding the mechanisms behind the variation of the acid strength depending on the framework location of the acid site. Furthermore, double aluminium substitutions can also be included in the study. We have proposed the migration of the protonated TMPO molecule away from the acid site to explain the existence of *very strong* and *weak* acidity. Therefore, this hypothesis can be verified by examining the energy barrier required to displace the protonated TMPO away from the acid site.

The tautomerization of phenol and catechol was studied in Chapter 5 prompted by the utilization of zeolite MFI as a support of metal nanoparticles during the hydrodeoxygenation of lignin-derived compounds. Nevertheless, the explicit presence of the metal nanoparticles was not considered, and thus this could be a future topic of research. There are computational reports regarding the conversion of phenolic monomers at the interphase between the nanoparticle and the support. These studies, together with what has been exposed here, can be used to analyse the metal-catalysed hydrogenation of the phenolic tautomer that is formed on the zeolite. This would require the explicit adsorption of a metal nanoparticle on the external surface of the zeolite. Additionally, the effect of the solvent on the tautomerization process could be analysed, using both an explicit and an implicit model.

The titanium substitution of zeolite LTA was investigated in Chapter 6. The titanium distributions obtained in this chapter could be used to investigate the catalytic redox transformation of small molecules such as methanol and ammonia. In addition, the research could be further expanded in order to consider triple or higher titanium substitutions. This would provide more information related to the distribution of titanium within the zeolite.

Appendix A. Chapter 3

A.1 Pure-silica Bulk Zeolite MFI

Si-O bond distances, O-Si-O and Si-O-Si angle distributions within the bulk framework obtained with different optimization methods.

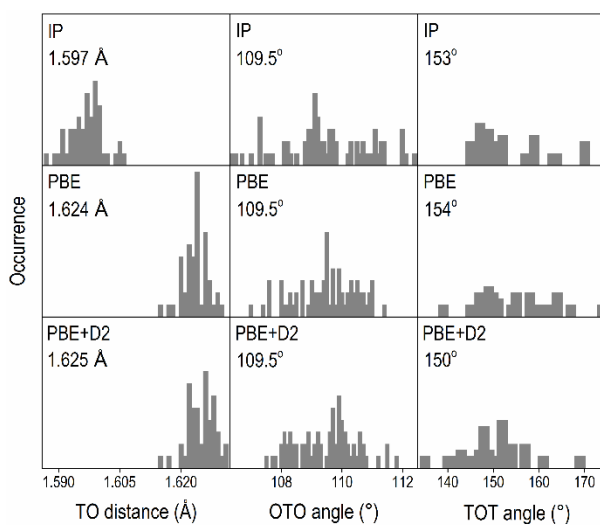


Figure A-1. Distributions of the Si-O distance (first column), intra-tetrahedral angle (second column) and the inter-tetrahedral angle (third column) for the full relaxed pure-silica cells using Interatomic Potentials (first row), PBE (second row) and PBE+D2 (third row). Average values are shown for each distribution.

A.2 Pure-silica Zeolite MFI Nanosheet

Si-O bond distances, O-Si-O and Si-O-Si angle distributions within slab frameworks with two different thicknesses.

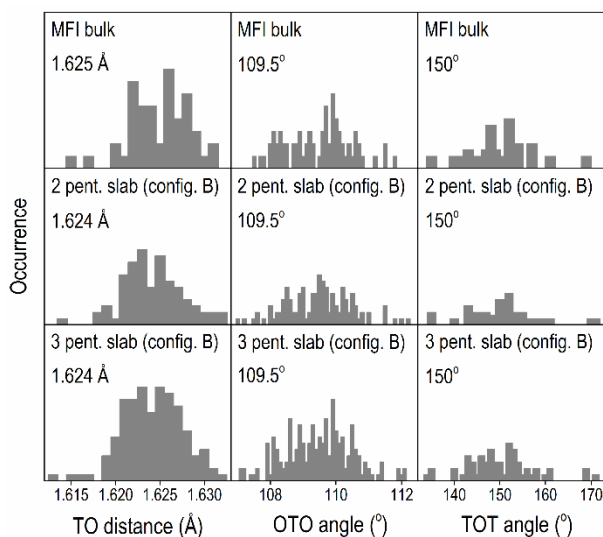


Figure A-2. Distributions of the Si-O distance (first column), the intra-tetrahedral angle (second column) and the inter-tetrahedral angle (third column) of the full relaxed pure-silica slabs with the PBE+D2 method. The data associated with the silanol groups was not considered. The pure-silica MFI bulk structure (first row) was included for comparison. Two-pentasil slab with H configuration B (second row) and three-pentasil slab with H configuration B (third row).

A.3 Termination of Surface (010) of Zeolite MFI

MFI surface terminations constraining a single hydroxyl group per terminal silicon atom. The study of the possible terminations for the (010) MFI surface termination was carried out using METADISE. For this purpose, a region representing the bulk (Region 1) was defined using five unit cells (see **Figure A-1**). Then the surface region (Region 2) was completed by a single unit cell; totalling about 1728 atoms plus the water units at the top surface to saturate the Si-O dangled bonds.

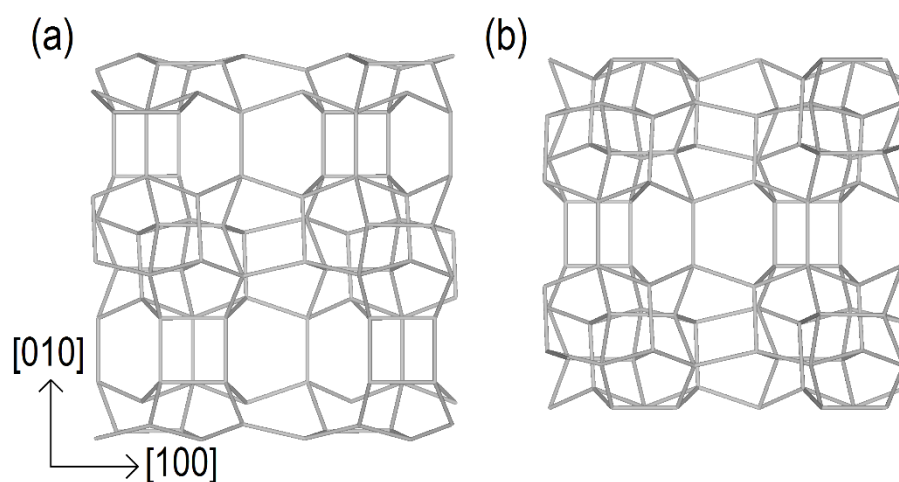


Figure A-3. MFI unit cells taken as starting structures to analyse possible terminations for the (010) MFI surface. (a) Unit cell formed by half of a pentasil layer at the top and at the bottom and a complete layer at the centre (b) Unit cell formed by two complete pentasil layers. Sets of atoms were removed from the bottom of the cell and added at its top; just those surfaces with a single dangled Si-O bond per terminal silicon atom at the top surface were accepted. The scan comprehended all possible combination of atoms and it was stopped when a half of pentasil layer was completely relocated from the bottom to the top. A total of 203 terminations were found ranging the number of silanol groups between 8 and 20. The complete pentasil layer termination carried the minimum number of silanol groups.

$$E = E_{hs} - E_{bulk} - nE_{(H+OH)}$$

Equation A-1. Thermodynamic equation to calculate the hydration energy of the completely hydrated surfaces. E_{hs} energy of the hydrated surface. E_{bulk} energy of the of the bulk. $E_{(H+OH)}$ energy of a water unit; this energy may represent the dissociation of water or any other process that finishes providing n hydrogens and n hydroxyls in order to saturate the surface silicons. This is a process that starts with the cleavage of the bulk structure to form the surface with the posterior addition of water to saturate the terminal silicons.

$$E_{ref} = \left(\frac{E_{hs}}{n} - \frac{E_{hs}^{ref}}{n^{ref}} \right) - \left(\frac{E_{bulk}}{n} - \frac{E_{bulk}^{ref}}{n^{ref}} \right)$$

Equation A-2. Equation to calculate the hydration energy without considering the water unit energy: $E_{(H+OH)}$. This equation was obtained dividing **Equation A-1** by the number of water units (n) and subtracting against reference energies (E_{hs}^{ref} and E_{bulk}^{ref}) corresponding to the complete pentasil termination.

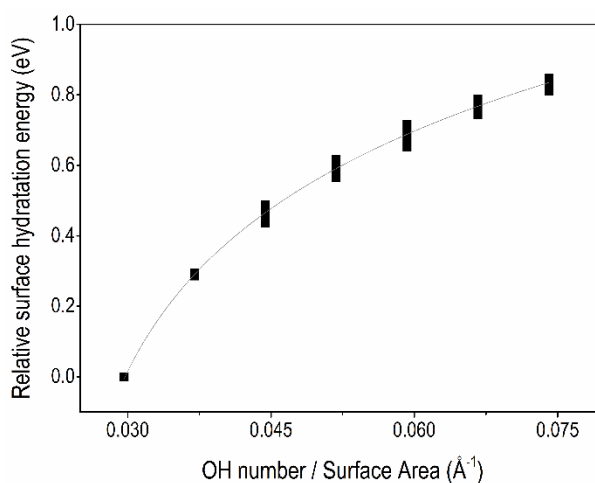


Figure A-4. Relative energy of the system using **Equation A-2** as a function of hydroxyls number per unit of area. The red line is for guiding the eye. This graph shows that the most probable termination is the one with the smallest number of water units added to saturate the terminal Si atoms or equivalently the one with the maximum number of Si-O-Si bridges in the framework.

A.4 Aluminium-substituted Zeolite MFI Nanosheet

Scattering of the T-O distance, OTO angle and TOT angle of the silanol groups.

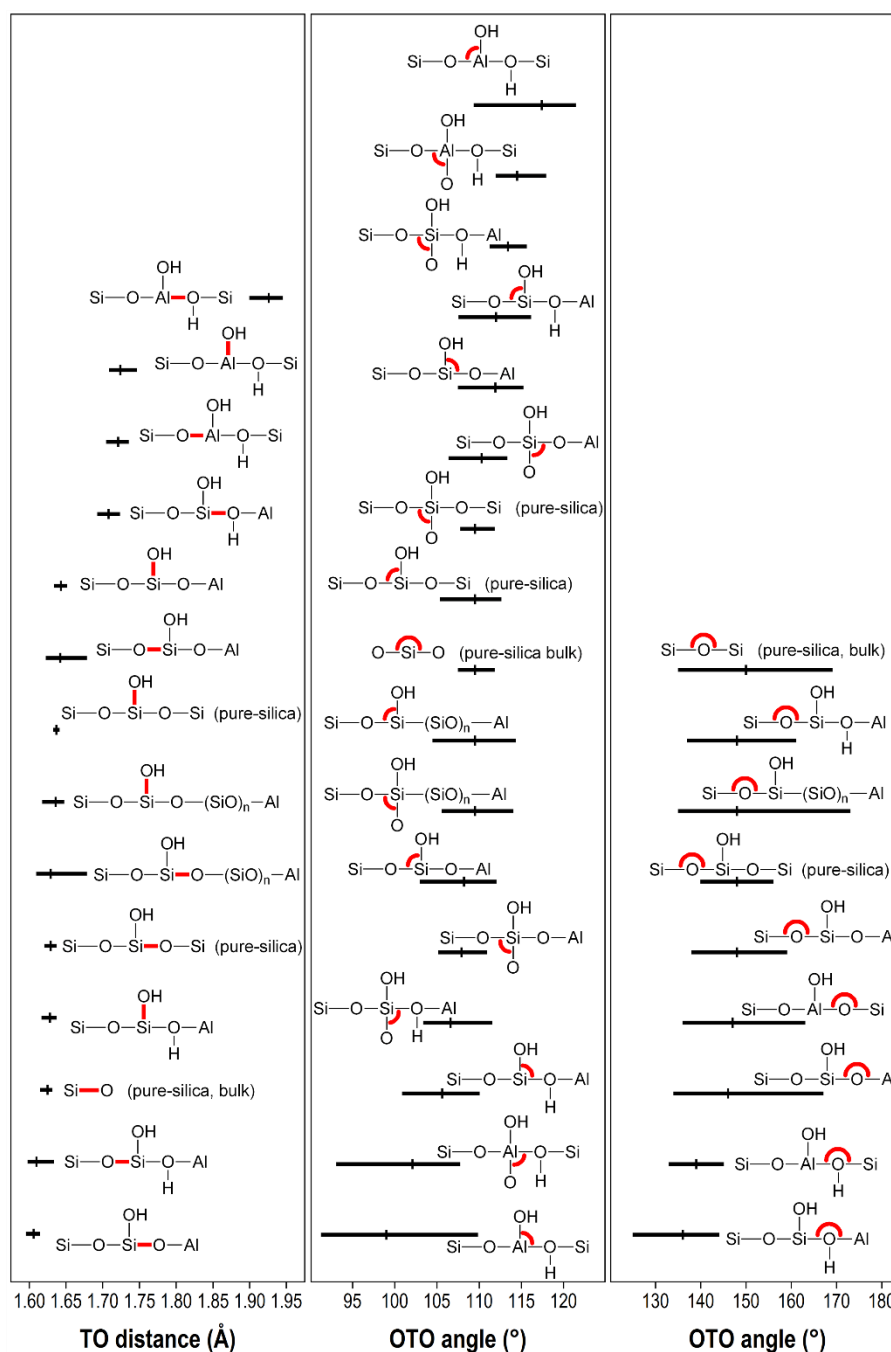


Figure A-5. Scattering of the T-O distances (a), O-T-O angles (b) and T-O-T angles (c) for the silanol and Al-substituted silanols. The horizontal lines establish the scattering ranges for the distances and angles; the average values are marked with small vertical lines. The structural scheme, besides each line, highlights in red the distance or the angle to which the range of values is referring.

A.5 Boltzmann Distribution and O-H Stretching Frequencies

Boltzmann distributions and O-H stretching frequencies for the proton as counter ion within the aluminium-substituted bulk and the two-pentasil slab.

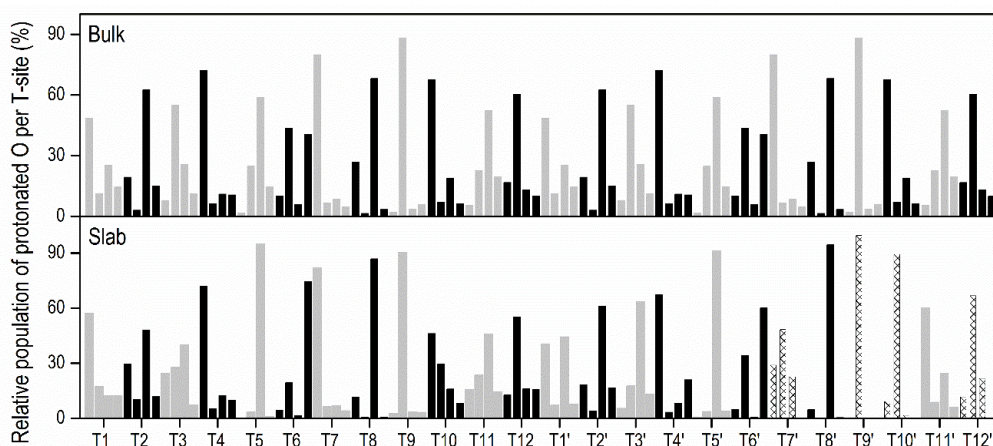


Figure A-6. Partition function (550 °C) within each set of four O atoms carrying the proton as counter ion when the Al is substituting a specific T-site; bulk (top) and slab(bottom). The first 12 T-sites in the x axis correspond to first half of the pentasil layer and located more distant from the surface; the second T-sites complete the pentasil layer and are the atoms exposed on the surface of the slab. The sets of four O atoms per T-site have alternating colours (grey and black) for better differentiation. The bars within each set correspond in increasing order to the numbers of the O-sites surrounding the Al atom. The T-sites that become silanolic positions when the structure is truncated are displayed in dense-crossed pattern. For silanolic positions the O-site with the highest numeration is missing since it form part of the Al-substituted silanol group. The O-sites for each T-site are as follow: **T1**(O1, O15, O16, O21), **T2**(O1, O2, O6, O13), **T3**(O2, O3, O19, O20), **T4**(O3, O4, O16, O17), **T5**(O4, O5, O14, O21), **T6**(O5, O6, O18, O19), **T7**(O7, O17, O22, O23), **T8**(O7, O8, O12, O13), **T9**(O8, O9, O18, O25), **T10**(O9, O10, O15, O26), **T11**(O10, O11, O14, O22), **T12**(O11, O12, O20, O24). The most stable O for each Al-substituted T-site was for the BULK: **T1**(O1), **T2**(O6), **T3**(O3), **T4**(O3), **T5**(O14), **T6**(O6), **T7**(O7), **T8**(O12), **T9**(O9), **T10**(O9), **T11**(O14), **T12**(O12). In the case of the SLAB, the variations in comparison with the BULK were: **T3**(O19), **T6**(O19) in the first half of the pentasil layer and **T1**(O16), **T3**(O19), **T6**(O19), **T7**(O17), **T10**(O10), **T11**(O10) for the second half of the pentasil layer.

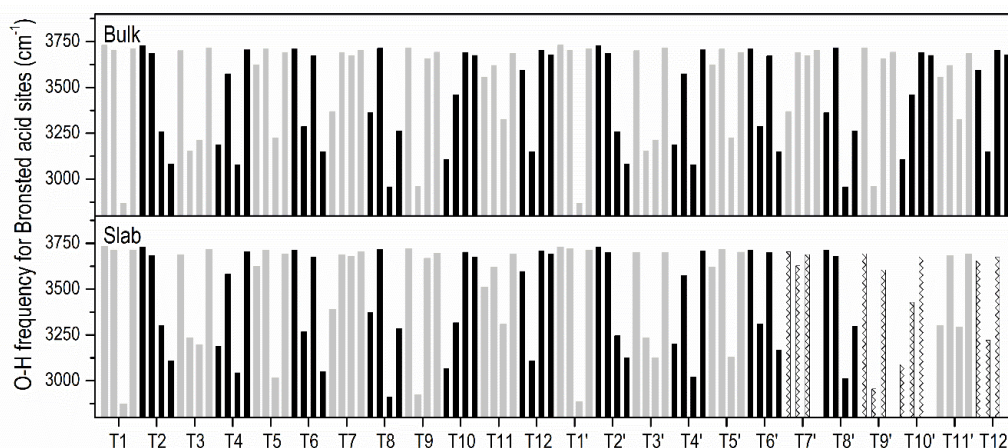


Figure A-7. Frequencies of the Bronsted acid sites for the bulk (top) and slab (bottom) structures. The first 12 T-sites in the x axis correspond to first half of the pentasil layer and located more distant from the surface; the second T-sites complete the pentasil layer and are the atoms exposed on the surface of the slab. The sets of four oxygen atoms per T-site have alternating colours (grey and black) for better differentiation. The bars within each set correspond to increasing order to the numbers of the O-sites surrounding the aluminium atom. The T-sites that become silanolic positions when the structure is truncated are displayed in dense-crossed pattern. For silanolic positions the O-site with the highest numeration is missing since it form part of the silanol-type group. The O-sites for each T-site are as follow: **T1**(O1, O15, O16, O21), **T2**(O1, O2, O6, O13), **T3**(O2, O3, O19, O20), **T4**(O3, O4, O16, O17), **T5**(O4, O5, O14, O21), **T6**(O5, O6, O18, O19), **T7**(O7, O17, O22, O23), **T8**(O7, O8, O12, O13), **T9**(O8, O9, O18, O25), **T10**(O9, O10, O15, O26), **T11**(O10, O11, O14, O22), **T12**(O11, O12, O20, O24).

References

- [1] International Zeolite Association (IZA); <http://www.iza-online.org/> (2017).
- [2] P. Bariand, F. Cesbron, R. Giraud, *Bull. La Soc. Fr. Mineral. Cristal.* 91 (1968) 34.
- [3] J.L. Schlenker, F.G. Dwyer, E.E. Jenkins, W.J. Rohrbaugh, G.T. Kokotailo, W.M. Meier, *Nature* 294 (1981) 340.
- [4] J. Bae, J. Cho, J.H. Lee, S.M. Seo, S.B. Hong, *Angew. Chemie Int. Ed.* 55 (2016) 7369.
- [5] Z.A.D. Lethbridge, J.J. Williams, R.I. Walton, K.E. Evans, C.W. Smith, *Microporous Mesoporous Mater.* 79 (2005) 339.
- [6] L.L. Hench, J.K. West, *Chem. Rev.* 90 (1990) 33.
- [7] A. Corma, M.E. Davis, *ChemPhysChem* 5 (2004) 304.
- [8] R.M. Barrer, P.J. Denny, *J. Chem. Soc.* (1961) 971.
- [9] M. Moliner, F. Rey, A. Corma, *Angew. Chemie Int. Ed.* 52 (2013) 13880.
- [10] P. Cubillas, J.T. Gebbie, S.M. Stevens, N. Blake, A. Umemura, O. Terasaki, M.W. Anderson, *J. Phys. Chem. C* 118 (2014) 23092.
- [11] P. Cubillas, S.M. Stevens, N. Blake, A. Umemura, C.B. Chong, O. Terasaki, M.W. Anderson, *J. Phys. Chem. C* 115 (2011) 12567.
- [12] R. Brent, P. Cubillas, S.M. Stevens, K.E. Jelfs, A. Umemura, J.T. Gebbie, B. Slater, O. Terasaki, M.A. Holden, M.W. Anderson, *J. Am. Chem. Soc.* 132 (2010) 13858.

- [13] D.W. Breck, W.G. Eversole, R.M. Milton, T.B. Reed, T.L. Thomas, *J. Am. Chem. Soc.* 78 (1956) 5963.
- [14] H.V. Thang, K. Frolich, M. Shamzhy, P. Eliášová, M. Rubeš, J. Čejka, R. Bulánek, P. Nachtigall, *Phys. Chem. Chem. Phys.* 18 (2016) 18063.
- [15] K. Góra-Marek, K. Brylewska, K.A. Tarach, M. Rutkowska, M. Jabłońska, M. Choi, L. Chmielarz, *Appl. Catal. B Environ.* 179 (2015) 589.
- [16] L. Regli, S. Bordiga, C. Lamberti, K.P. Lillerud, S.I. Zones, A. Zecchina, *J. Phys. Chem. C* 111 (2007) 2992.
- [17] H. Kosslick, V.A. Tuan, B. Parlitz, R. Fricke, C. Peuker, W. Storek, *J. Chem. Soc. Faraday Trans.* 89 (1993) 1131.
- [18] H. Kosslick, V.A. Tuan, G. Walther, W. Storek, *Cryst. Res. Technol.* 28 (1993) 1109.
- [19] C.T. Briden, C.D. Williams, D. Apperley, *Inorg. Mater.* 43 (2007) 758.
- [20] J. Li, P. Miao, Z. Li, T. He, D. Han, J. Wu, Z. Wang, J. Wu, *Energy Convers. Manag.* 93 (2015) 259.
- [21] N. Sapawe, A.A. Jalil, S. Triwahyono, S.H. Adam, N.F. Jaafar, M.A.H. Satar, *Appl. Catal. B Environ.* 125 (2012) 311.
- [22] M.A. Camblor, A. Corma, A. Martínez, J. Pérez-Pariente, *J. Chem. Soc., Chem. Commun.* 0 (1992) 589.
- [23] M. V. Shamzhy, P. Eliášová, D. Vitvarová, M. V. Opanasenko, D.S. Firth, R.E. Morris, *Chem. - A Eur. J.* 22 (2016) 17377.
- [24] C.M. Lew, N. Rajabbeigi, M. Tsapatsis, Tin-Containing Zeolite for the

Isomerization of Cellulosic Sugars, 2012.

- [25] G. Li, E.A. Pidko, E.J.M. Hensen, *Catal. Sci. Technol.* 4 (2014) 2241.
- [26] R.M. Barrer, *J. Chem. Soc.* 0 (1948) 127.
- [27] D.W. Breck, *J. Chem. Educ.* 41 (1964) 678.
- [28] M.E. Davis, R.F. Lobo, *Chem. Mater.* 4 (1992) 756.
- [29] W. Vermeiren, J.-P. Gilson, *Top. Catal.* 52 (2009) 1131.
- [30] M. Hunger, *Catal. Rev.* 39 (1997) 345.
- [31] M. Hunger, *Solid State Nucl. Magn. Reson.* 6 (1996) 1.
- [32] Q. Zhao, W.-H. Chen, S.-J. Huang, Y.-C. Wu, H.-K. Lee, S.-B. Liu, *J. Phys. Chem. B* 106 (2002) 4462.
- [33] C.C.H. Lin, K.A. Dambrowitz, S.M. Kuznicki, *Can. J. Chem. Eng.* 90 (2012) 207.
- [34] H. Yahiro, M. Iwamoto, *Appl. Catal. A Gen.* 222 (2001) 163.
- [35] B.M. Abu-Zied, W. Schwieger, A. Unger, *Appl. Catal. B Environ.* 84 (2008) 277.
- [36] A. Dyer, S. Amini, H. Enamy, H.A. El-Naggar, M.W. Anderson, *Zeolites* 13 (1993) 281.
- [37] S. Wang, Y. Peng, *Chem. Eng. J.* 156 (2010) 11.
- [38] D. Bastani, N. Esmaeili, M. Asadollahi, *J. Ind. Eng. Chem.* 19 (2013) 375.
- [39] K.L. Yeung, W. Han, *Catal. Today* 236 (2014) 182.
- [40] H.S. Kim, K.B. Yoon, *Coord. Chem. Rev.* 263–264 (2014) 239.

- [41] K. Tanabe, W.F. Holderich, *Appl. Catal. A Gen.* 181 (1999) 399.
- [42] E.M. Flanigen, J.M. Bennett, R.W. Grose, J.P. Cohen, R.L. Patton, R.M. Kirchner, J. V. Smith, *Nature* 271 (1978) 512.
- [43] N. Rahimi, R. Karimzadeh, *Appl. Catal. A Gen.* 398 (2011) 1.
- [44] M. Matsuoka, W.-S. Ju, H.-J. Chen, Y. Sakatani, M. Anpo, *Res. Chem. Intermed.* 29 (2003) 477.
- [45] D.G. Hay, H. Jaeger, *J. Chem. Soc. Chem. Commun.* (1984) 1433.
- [46] T.B. Reed, D.W. Breck, *J. Am. Chem. Soc.* 78 (1956) 5972.
- [47] E.L. Uzunova, G.S. Nikolov, 104 (2000) 5302.
- [48] Z. Wu, S. Goel, M. Choi, E. Iglesia, *J. Catal.* 311 (2014) 458.
- [49] S.T. Korhonen, D.W. Fickel, R.F. Lobo, B.M. Weckhuysen, A.M. Beale, *Chem. Commun.* 47 (2011) 800.
- [50] U. Olsbye, S. Svelle, M. Bjørngen, P. Beato, T.V.W. Janssens, F. Joensen, S. Bordiga, K.P. Lillerud, *Angew. Chemie Int. Ed.* 51 (2012) 5810.
- [51] M. Palomino, A. Corma, J.L. Jordá, F. Rey, S. Valencia, *Chem. Commun.* 48 (2012) 215.
- [52] A. Corma, F. Rey, J. Rius, M.J. Sabater, S. Valencia, *Nature* 431 (2004) 287.
- [53] B.W. Boal, J.E. Schmidt, M.A. Deimund, M.W. Deem, L.M. Henling, S.K. Brand, S.I. Zones, M.E. Davis, *Chem. Mater.* 27 (2015) 7774.
- [54] M. Choi, K. Na, J. Kim, Y. Sakamoto, O. Terasaki, R. Ryoo, *Nature* 461 (2009) 246.

- [55] M.W. Anderson, K.S. Pachis, J. Shi, S.W. Carr, *J. Mater. Chem.* 2 (1992) 255.
- [56] A. Corma, V. Fornes, S.B. Pergher, T.L.M. Maesen, J.G. Buglass, *Nature* 396 (1998) 353.
- [57] K. Na, M. Choi, W. Park, Y. Sakamoto, O. Terasaki, R. Ryoo, *J. Am. Chem. Soc.* 132 (2010) 4169.
- [58] J. Jung, C. Jo, K. Cho, R. Ryoo, *J. Mater. Chem.* 22 (2012) 4637.
- [59] Y. Seo, K. Cho, Y. Jung, R. Ryoo, *ACS Catal.* 3 (2013) 713.
- [60] W.J. Roth, B. Gil, B. Marszalek, *Catal. Today* 227 (2014) 9.
- [61] W.J. Roth, P. Nachtigall, R.E. Morris, J. Čejka, *Chem. Rev.* 114 (2014) 4807.
- [62] R. Rinaldi, F. Schüth, *Energy Environ. Sci.* 2 (2009) 610.
- [63] C. Li, X. Zhao, A. Wang, G.W. Huber, T. Zhang, *Chem. Rev.* 115 (2015) 11559.
- [64] T. Ennaert, J. Van Aelst, J. Dijkmans, R. De Clercq, W. Schutyser, M. Dusselier, D. Verboekend, B.F. Sels, *Chem. Soc. Rev.* 45 (2016) 584.
- [65] H. Ben, A.J. Ragauskas, *ACS Sustain. Chem. Eng.* 1 (2013) 316.
- [66] Z. Ma, V. Custodis, J.A. van Bokhoven, *Catal. Sci. Technol.* 4 (2014) 766.
- [67] C.A. Mullen, A.A. Boateng, *Fuel Process. Technol.* 91 (2010) 1446.
- [68] M. Zhang, A. Moutsoglou, *Energy & Fuels* 28 (2014) 1066.
- [69] D.-Y. Hong, S.J. Miller, P.K. Agrawal, C.W. Jones, *Chem. Commun.* 46 (2010) 1038.
- [70] C. Zhao, J.A. Lercher, *ChemCatChem* 4 (2012) 64.

- [71] W. Zhang, J. Chen, R. Liu, S. Wang, L. Chen, K. Li, *ACS Sustain. Chem. Eng.* 2 (2014) 683.
- [72] S. Kasakov, H. Shi, D.M. Camaioni, C. Zhao, E. Baráth, A. Jentys, J.A. Lercher, *Green Chem.* 17 (2015) 5079.
- [73] S.K. Singh, J.D. Ekhe, *Catal. Sci. Technol.* 5 (2015) 2117.
- [74] X. Wang, R. Rinaldi, *Angew. Chem. Int. Ed. Engl.* 52 (2013) 11499.
- [75] X. Zhu, L. Nie, L.L. Lobban, R.G. Mallinson, D.E. Resasco, *Energy & Fuels* 28 (2014) 4104.
- [76] H. Liu, T. Jiang, B. Han, S. Liang, Y. Zhou, *Science* 326 (2009) 1250.
- [77] J. Lu, S. Behtash, O. Mamun, A. Heyden, *ACS Catal.* 5 (2015) 2423.
- [78] L. Nie, D.E. Resasco, *J. Catal.* 317 (2014) 22.
- [79] L. Nie, P.M. de Souza, F.B. Noronha, W. An, T. Sooknoi, D.E. Resasco, *J. Mol. Catal. A Chem.* 388–389 (2014) 47.
- [80] Q. Tan, G. Wang, L. Nie, A. Dinse, C. Buda, J. Shabaker, D.E. Resasco, *ACS Catal.* 5 (2015) 6271–6283.
- [81] P.M. de Souza, R.C. Rabelo-Neto, L.E.P. Borges, G. Jacobs, B.H. Davis, T. Sooknoi, D.E. Resasco, F.B. Noronha, *ACS Catal.* 5 (2015) 1318.
- [82] G. Kresse, J. Hafner, *Phys. Rev. B* 47 (1993) 558.
- [83] G. Kresse, J. Hafner, *Phys. Rev. B* 49 (1994) 14251.
- [84] G. Kresse, J. Furthmüller, *Comput. Mater. Sci.* 6 (1996) 15.
- [85] G. Kresse, J. Furthmüller, *Phys. Rev. B* 54 (1996) 11169.

- [86] G.W. Watson, E.T. Kelsey, N.H. de Leeuw, D.J. Harris, S.C. Parker, *J. Chem. Soc. Faraday Trans.* 92 (1996) 433.
- [87] J.D. Gale, *Zeitschrift Für Krist. - Cryst. Mater.* 220 (2005) 552.
- [88] J.D. Gale, A.L. Rohl, *Mol. Simul.* 29 (2003) 291.
- [89] E. Schrödinger, *Phys. Rev.* 28 (1926) 1049.
- [90] M. Born, R. Oppenheimer, *Ann. Phys.* 84 (1927) 457.
- [91] Ira N. Levine, *Quantum Chemistry*, 5th ed., Prentice Hall, Upper Saddle River, New Jersey 07458, 2000.
- [92] A. Szabo, N.S. Ostlund, *Modern Quantum Chemistry. Introduction to Advanced Electronic Structure Theory*, Dover Publications Inc. Mineola New York, 1996.
- [93] P. Hohenberg, W. Kohn, *Phys. Rev.* 136 (1964) B864.
- [94] W. Kohn, L.J. Sham, *Phys. Rev.* 140 (1965) A1133.
- [95] R.G. Parr, W. Yang, *Density Functional Theory of Atoms and Molecules*, Oxford University Press, 1989.
- [96] J.P. Perdew, *Phys. Rev. Lett.* 55 (1985) 1665.
- [97] S.K. Ma, K.A. Brueckner, *Phys. Rev.* 165 (1968) 18.
- [98] J.P. Perdew, D.C. Langreth, V. Sahni, *Phys. Rev. Lett.* 38 (1977) 1030.
- [99] F.A. Hamprecht, A.J. Cohen, D.J. Tozer, N.C. Handy, *J. Chem. Phys.* 109 (1998) 6264.
- [100] J.P. Perdew, K. Burke, M. Ernzerhof, *Phys. Rev. Lett.* 77 (1996) 3865.

- [101] S. Kurth, J.P. Perdew, P. Blaha, *Int. J. Quantum Chem.* 75 (1999) 889.
- [102] P. Pulay, *Mol. Phys.* 17 (1969) 197.
- [103] Charles Kittel, *Introduction to Solid State Physics*, 8th ed., John Wiley & Sons, Inc., 2005.
- [104] F. Bloch, *Zeitschrift Für Phys.* 52 (1929) 555.
- [105] Michael P. Marder, *Condensed Matter Physics*, John Wiley & Sons, Inc., 2000.
- [106] J.D. Joannopoulos, M.L. Cohen, *J. Phys. C Solid State Phys.* 6 (1973) 1572.
- [107] D.J. Chadi, M.L. Cohen, *Phys. Rev. B* 8 (1973) 5747.
- [108] H.J. Monkhorst, J.D. Pack, *Phys. Rev. B* 13 (1976) 5188.
- [109] J.C. Phillips, *Phys. Rev.* 112 (1958) 685.
- [110] J.C. Phillips, L. Kleinman, *Phys. Rev.* 116 (1959) 287.
- [111] D.R. Hamann, M. Schlüter, C. Chiang, *Phys. Rev. Lett.* 43 (1979) 1494.
- [112] D. Vanderbilt, *Phys. Rev. B* 41 (1990) 7892.
- [113] P.E. Blöchl, *Phys. Rev. B* 50 (1994) 17953.
- [114] G. Kresse, D. Joubert, *Phys. Rev. B* 59 (1999) 1758.
- [115] S.G. Louie, S. Froyen, M.L. Cohen, *Phys. Rev. B* 26 (1982) 1738.
- [116] P.E. Blöchl, O. Jepsen, O.K. Andersen, *Phys. Rev. B* 49 (1994) 16223.
- [117] M. Methfessel, A. Paxton, *Phys. Rev. B* 40 (1989) 3616.
- [118] R.F.W. Bader, M.T. Carroll, J.R. Cheeseman, C. Chang, *J. Am. Chem. Soc.*

- 109 (1987) 7968.
- [119] R.F.W. Bader, R.J. Gillespie, P.J. MacDougall, *J. Am. Chem. Soc.* 110 (1988) 7329.
- [120] A. Ambrosetti, D. Alfè, J. Robert A. DiStasio, A. Tkatchenko, *J. Phys. Chem. Lett.* 5 (2014) 849.
- [121] J. Řezáč, K.E. Riley, P. Hobza, *J. Chem. Theory Comput.* 8 (2012) 4285.
- [122] J. Řezáč, K.E. Riley, P. Hobza, *J. Chem. Theory Comput.* 7 (2011) 2427.
- [123] D.C. Langreth, M. Dion, H. Rydberg, E. Schröder, P. Hyldgaard, B.I. Lundqvist, *Int. J. Quantum Chem.* 101 (2005) 599.
- [124] S. Grimme, *J. Comput. Chem.* 27 (2006) 1787.
- [125] S. Grimme, J. Antony, S. Ehrlich, H. Krieg, *J. Chem. Phys.* 132 (2010) 154104.
- [126] M.C. Payne, M.P. Teter, D.C. Allan, T.A. Arias, J.D. Joannopoulos, *Rev. Mod. Phys.* 64 (1992) 1045.
- [127] L. Verlet, *Phys. Rev.* 159 (1967) 98.
- [128] W.C. Swope, H.C. Andersen, P.H. Berens, K.R. Wilson, *J. Chem. Phys.* 76 (1982) 637.
- [129] S. Nosé, *J. Chem. Phys.* 81 (1984) 511.
- [130] S. Nosé, *Prog. Theor. Phys. Suppl.* 103 (1991) 1.
- [131] S. Baroni, S. De Gironcoli, A. Dal Corso, P. Giannozzi, *Rev. Mod. Phys.* 73 (2001) 515.

- [132] A. Komornicki, J.W. McIver, *J. Am. Chem. Soc.* 98 (1976) 4553.
- [133] D.A. McQuarrie, J.D. Simon, *Molecular Thermodynamics*, 1999.
- [134] G. Mills, H. Jónsson, G.K. Schenter, *Surf. Sci.* 324 (1995) 305.
- [135] H. Jonsson, G. Mills, K.W. Jacobsen, “Nudged Elastic Band Method for Finding Minimum Energy Paths of Transitions”, in “Classical and Quantum Dynamics in Condensed Phase Simulations,” World Scientific, 1998.
- [136] G. Henkelman, H. Jónsson, *J. Chem. Phys.* 111 (1999) 7010.
- [137] A. Heyden, A.T. Bell, F.J. Keil, *J. Chem. Phys.* 123 (2005) 224101.
- [138] K. Born, M.; Huang, *Dynamical Theory of Crystal Lattices*, Oxford University Press: Oxford, 1954.
- [139] P.P. Ewald, *Ann. Phys.* 369 (1921) 253.
- [140] D.E. Parry, *Surf. Sci.* 49 (1975) 433.
- [141] D.E. Parry, *Surf. Sci.* 54 (1976) 195.
- [142] R.A. Buckingham, *Proc. R. Soc. Lond. A. Math. Phys. Sci.* 168 (1938) 264.
- [143] B. Dick, A. Overhauser, *Phys. Rev.* 112 (1958) 90.
- [144] A.V. Barzykin, K. Seki, M. Tachiya, *Adv. Colloid Interface Sci.* 89–90 (2001) 47.
- [145] S. Al-Khattaf, M.N. Akhtar, T. Odedairo, A. Aitani, N.M. Tukur, M. Kubû, Z. Musilová-Pavlačková, J. Čejka, *Appl. Catal. A Gen.* 394 (2011) 176.
- [146] J. Pérez-Ramírez, C.H. Christensen, K. Egeblad, C.H. Christensen, J.C. Groen, *Chem. Soc. Rev.* 37 (2008) 2530.

- [147] G.T. Kokotailo, S.L. Lawton, D.H. Olson, W.M. Meier, *Nature* 272 (1978) 437.
- [148] W. Park, D. Yu, K. Na, K.E. Jelfs, B. Slater, Y. Sakamoto, R. Ryoo, *Chem. Mater.* 23 (2011) 5131.
- [149] K. Na, W. Park, Y. Seo, R. Ryoo, *Chem. Mater.* 23 (2011) 1273.
- [150] K. Na, C. Jo, J. Kim, W.-S. Ahn, R. Ryoo, *ACS Catal.* 1 (2011) 901.
- [151] J. Kim, W. Park, R. Ryoo, *ACS Catal.* 1 (2011) 337.
- [152] C. Jo, R. Ryoo, N. Žilková, D. Vitvarová, J. Čejka, *Catal. Sci. Technol.* 3 (2013) 2119.
- [153] A.J.J. Koekkoek, W. Kim, V. Degirmenci, H. Xin, R. Ryoo, E.J.M. Hensen, *J. Catal.* 299 (2013) 81.
- [154] K. Varoon, X. Zhang, B. Elyassi, D.D. Brewer, M. Gettel, S. Kumar, J.A. Lee, S. Maheshwari, A. Mittal, C.-Y. Sung, M. Cococcioni, L.F. Francis, A. V McCormick, K.A. Mkhoyan, M. Tsapatsis, *Science* 334 (2011) 72.
- [155] Y. Liu, X. Chen, *Phys. Chem. Chem. Phys.* 15 (2013) 6817.
- [156] S.K. Schnell, L. Wu, A.J.J. Koekkoek, S. Kjelstrup, E.J.M. Hensen, T.J.H. Vlugt, *J. Phys. Chem. C* 117 (2013) 24503.
- [157] P.W. Tasker, *Philos. Mag. A* 39 (1979) 119.
- [158] D. Santos-Carballal, A. Roldan, R. Grau-Crespo, N.H. de Leeuw, *Phys. Chem. Chem. Phys.* 16 (2014) 21082.
- [159] M.J. Sanders, M. Leslie, C.R.A. Catlow, *J. Chem. Soc. Chem. Commun.* (1984) 1271.

- [160] P.S. Baram, S.C. Parker, *Philos. Mag. Part B* 73 (1996) 49.
- [161] N.J. Henson, A.K. Cheetham, J.D. Gale, *Chem. Mater.* 6 (1994) 1647.
- [162] L. Tang, L. Shi, C. Bonneau, J. Sun, H. Yue, A. Ojuva, B.-L. Lee, M. Kritikos, R.G. Bell, Z. Bacsik, J. Mink, X. Zou, *Nat. Mater.* 7 (2008) 381.
- [163] F.M. Higgins, N.H. de Leeuw, S.C. Parker, *J. Mater. Chem.* 12 (2002) 124.
- [164] T. Bučko, J. Hafner, S. Lebègue, J.G. Ángyán, *J. Phys. Chem. A* 114 (2010) 11814.
- [165] N.Y. Dzade, A. Roldan, N.H. de Leeuw, *J. Chem. Phys.* 139 (2013) 124708.
- [166] S.S. Tafreshi, A. Roldan, N.H. de Leeuw, *J. Phys. Chem. C* 118 (2014) 26103.
- [167] S.S. Tafreshi, A. Roldan, N.Y. Dzade, N.H. de Leeuw, *Surf. Sci.* 622 (2014) 1.
- [168] K. Momma, F. Izumi, *J. Appl. Cryst.* 44 (2011) 1272.
- [169] G.P. Francis, M.C. Payne, *J. Phys. Condens. Matter* 2 (1990) 4395.
- [170] F. Birch, *Phys. Rev.* 71 (1947) 809.
- [171] S. Quartieri, R. Arletti, G. Vezzalini, F. Di Renzo, V. Dmitriev, *J. Solid State Chem.* 191 (2012) 201.
- [172] A. Ghorbanpour, J.D. Rimer, L.C. Grabow, *Catal. Commun.* 52 (2014) 98.
- [173] E.G. Derouane, J.G. Fripiat, *Zeolites* 5 (1985) 165.
- [174] N. Katada, K. Suzuki, T. Noda, G. Sastre, M. Niwa, *J. Phys. Chem. C* 113 (2009) 19208.
- [175] K. Sillar, P. Burk, *J. Phys. Chem. B* 108 (2004) 9893.

- [176] A. Redondo, P.J. Hay, *J. Phys. Chem.* 97 (1993) 11754.
- [177] R. Grau-Crespo, A.G. Peralta, A. Rabdel Ruiz-Salvador, A. Gómez, R. López-Cordero, *Phys. Chem. Chem. Phys.* 2 (2000) 5716.
- [178] A.R. Ruiz-Salvador, R. Grau-Crespo, A.E. Gray, D.W. Lewis, *J. Solid State Chem.* 198 (2013) 330.
- [179] K.-P. Schröder, J. Sauer, M. Leslie, R.C.A. Catlow, *Zeolites* 12 (1992) 20.
- [180] J. Dědeček, Z. Sobalík, B. Wichterlová, *Catal. Rev.* 54 (2012) 135.
- [181] V. V. Mihaleva, R.A. van Santen, A.P.J. Jansen, *J. Chem. Phys.* 119 (2003) 13053.
- [182] O. Bludský, M. Šilhan, P. Nachtigall, *J. Chem. Phys.* 117 (2002) 9298.
- [183] T. Demuth, J. Hafner, L. Benco, H. Toulhoat, *J. Phys. Chem. B* 104 (2000) 4593.
- [184] T. Bučko, L. Benco, T. Demuth, J. Hafner, *J. Chem. Phys.* 117 (2002) 7295.
- [185] M. Henderson, *Surf. Sci. Rep.* 46 (2002) 1.
- [186] A. Hodgson, S. Haq, *Surf. Sci. Rep.* 64 (2009) 381.
- [187] T. Bučko, L. Benco, J. Hafner, *J. Chem. Phys.* 118 (2003) 8437.
- [188] L.-E. Sandoval-Díaz, J.-A. González-Amaya, C.-A. Trujillo, *Microporous Mesoporous Mater.* 215 (2015) 229.
- [189] J. Weitkamp, *Solid State Ionics* 131 (2000) 175.
- [190] M. Moliner, C. Martínez, A. Corma, *Angew. Chemie Int. Ed.* 54 (2015) 3560.
- [191] J. Čejka, B. Wichterlová, *Catal. Rev.* 44 (2002) 375.

- [192] E.G. Derouane, J.C. Védrine, R.R. Pinto, P.M. Borges, L. Costa, M.A.N.D.A. Lemos, F. Lemos, F.R. Ribeiro, *Catal. Rev.* 55 (2013) 454.
- [193] A. Zheng, S. Bin Liu, F. Deng, *Solid State Nucl. Magn. Reson.* 55–56 (2013) 12.
- [194] J. Xu, A. Zheng, J. Yang, Y. Su, J. Wang, D. Zeng, M. Zhang, C. Ye, F. Deng, *J. Phys. Chem. B* 110 (2006) 10662.
- [195] S. Li, S.-J. Huang, W. Shen, H. Zhang, H. Fang, A. Zheng, S.-B. Liu, F. Deng, *J. Phys. Chem. C* 112 (2008) 14486.
- [196] A. Simperler, R.G. Bell, M.W. Anderson, *J. Phys. Chem. B* 108 (2004) 7142.
- [197] A. Zheng, H. Zhang, X. Lu, S.-B. Liu, F. Deng, *J. Phys. Chem. B* 112 (2008) 4496.
- [198] Y. Ni, A. Sun, X. Wu, G. Hai, J. Hu, T. Li, G. Li, *Microporous Mesoporous Mater.* 143 (2011) 435.
- [199] C. Costa, I.P. Dzikh, J.M. Lopes, F. Lemos, F.R. Ribeiro, *J. Mol. Catal. A Chem.* 154 (2000) 193.
- [200] T.J. Kwok, K. Jayasuriya, R. Damavarapu, B.W. Brodman, *J. Org. Chem.* 59 (1994) 4939.
- [201] Y. Wang, G. Jian, Z. Peng, J. Hu, X. Wang, W. Duan, B. Liu, *Catal. Commun.* 66 (2015) 34.
- [202] A. Zheng, B. Han, B. Li, S.-B. Liu, F. Deng, *Chem. Commun.* 48 (2012) 6936.
- [203] C.E. Hernandez-Tamargo, A. Roldan, N.H. de Leeuw, *J. Solid State Chem.* 237 (2016) 192.

- [204] K.-M. Ho, C.L. Fu, B.N. Harmon, W. Weber, D.R. Hamann, *Phys. Rev. Lett.* 49 (1982) 673.
- [205] C.-L. Fu, K.-M. Ho, *Phys. Rev. B* 28 (1983) 5480.
- [206] D.M. Bylander, L. Kleinman, *Phys. Rev. B* 46 (1992) 13756.
- [207] M. Tuckerman, K. Laasonen, M. Sprik, M. Parrinello, *J. Chem. Phys.* 103 (1995) 150.
- [208] G. Henkelman, A. Arnaldsson, H. Jónsson, *Comput. Mater. Sci.* 36 (2006) 354.
- [209] E. Sanville, S.D. Kenny, R. Smith, G. Henkelman, *J. Comput. Chem.* 28 (2007) 899.
- [210] W. Tang, E. Sanville, G. Henkelman, *J. Phys. Condens. Matter* 21 (2009) 84204.
- [211] P. Wernet, D. Nordlund, U. Bergmann, M. Cavalleri, M. Odelius, H. Ogasawara, L.A. Näslund, T.K. Hirsch, L. Ojamäe, P. Glatzel, L.G.M. Pettersson, A. Nilsson, *Science* 304 (2004) 995.
- [212] S.-J. Huang, C.-Y. Yang, A. Zheng, N. Feng, N. Yu, P.-H. Wu, Y.-C. Chang, Y.-C. Lin, F. Deng, S.-B. Liu, *Chem. Asian J.* 6 (2011) 137.
- [213] L. Petridis, R. Schulz, J.C. Smith, *J. Am. Chem. Soc.* 133 (2011) 20277.
- [214] L. Petridis, S.V. Pingali, V. Urban, W.T. Heller, H.M. O'Neill, M. Foston, A. Ragauskas, J.C. Smith, *Phys. Rev. E. Stat. Nonlin. Soft Matter Phys.* 83 (2011) 61911.
- [215] R. Carrasquillo-Flores, M. Kåldström, F. Schüth, J.A. Dumesic, R. Rinaldi,

ACS Catal. 3 (2013) 993.

- [216] P.T. Patil, U. Armbruster, M. Richter, A. Martin, *Energy & Fuels* 25 (2011) 4713.
- [217] M. Kleinert, T. Barth, *Energy & Fuels* 22 (2008) 1371.
- [218] E. Furimsky, *Appl. Catal. A Gen.* 199 (2000) 147.
- [219] W. Song, Y. Liu, E. Baráth, C. Zhao, J.A. Lercher, *Green Chem.* 17 (2015) 1204.
- [220] G.B. Kistiakowsky, J.R. Ruhoff, H.A. Smith, W.E. Vaughan, *J. Am. Chem. Soc.* 58 (1936) 146.
- [221] R.C. Nelson, B. Baek, P. Ruiz, B. Goundie, A. Brooks, M.C. Wheeler, B.G. Frederick, L.C. Grabow, R.N. Austin, *ACS Catal.* 5 (2015) 6509.
- [222] S. Grimme, S. Ehrlich, L. Goerigk, *J. Comput. Chem.* 32 (2011) 1456.
- [223] K. Barta, G.R. Warner, E.S. Beach, P.T. Anastas, *Green Chem.* 16 (2014) 191.
- [224] S. Sklenak, J. Dedecek, C. Li, B. Wichterlová, V. Gábová, M. Sierka, J. Sauer, *Phys. Chem. Chem. Phys.* 11 (2009) 1237.
- [225] J.A. Van Bokhoven, A.M.J. Van der Eerden, D.C. Koningsberger, *J. Am. Chem. Soc.* 125 (2003) 7435.
- [226] G. Li, J. Han, H. Wang, X. Zhu, Q. Ge, *ACS Catal.* 5 (2015) 2009.
- [227] L. Zhu, J.W. Bozzelli, *J. Phys. Chem. A* 107 (2003) 3696.
- [228] I. Gómez, E. Rodríguez, M. Reguero, *J. Mol. Struct. THEOCHEM* 767 (2006) 11.

- [229] B.D. Montejo-Valencia, M.C. Curet-Arana, *J. Phys. Chem. C* 119 (2015) 4148.
- [230] G. Yang, L. Zhou, X. Han, *J. Mol. Catal. A Chem.* 363–364 (2012) 371.
- [231] E. Nikolla, Y. Román-Leshkov, M. Moliner, M.E. Davis, *ACS Catal.* 1 (2011) 408.
- [232] H.W. Lee, S.H. Park, J.-K. Jeon, R. Ryoo, W. Kim, D.J. Suh, Y.-K. Park, *Catal. Today* 232 (2014) 119.
- [233] O. Cheung, N. Hedin, *RSC Adv.* 4 (2014) 14480.
- [234] C.A. Fyfe, G.J. Kennedy, G.T. Kokotailo, C.T. DeSchutter, *J. Chem. Soc. Chem. Commun.* (1984) 1093.
- [235] D. Jo, T. Ryu, G.T. Park, P.S. Kim, C.H. Kim, I.S. Nam, S.B. Hong, *ACS Catal.* 6 (2016) 2443.
- [236] S. Inagaki, Y. Tsuboi, M. Sasaki, K. Mamiya, S. Park, Y. Kubota, *Green Chem.* 18 (2016) 735.
- [237] J. Kim, J. Chun, R. Ryoo, *Chem. Commun.* 51 (2015) 13102.
- [238] B. Tang, W. Dai, X. Sun, N. Guan, L. Li, M. Hunger, *Green Chem.* 16 (2014) 2281.
- [239] X. Lu, W.J. Zhou, H. Wu, A. Liebens, P. Wu, *Appl. Catal. A Gen.* 515 (2016) 51.
- [240] A. Jentys, C.R.A. Catlow, *Catal. Letters* 22 (1993) 251.
- [241] C.M. Barker, D. Gleeson, N. Kaltsoyannis, C.R.A. Catlow, G. Sankar, J.M. Thomas, *Phys. Chem. Chem. Phys.* 4 (2002) 1228.

- [242] P.E. Sinclair, G. Sankar, C.R.A. Catlow, J.M. Thomas, T. Maschmeyer, J. Phys. Chem. B 101 (1997) 4232.
- [243] J. To, A.A. Sokol, S.A. French, C.R.A. Catlow, J. Phys. Chem. C 112 (2008) 7173.
- [244] R. Grau-Crespo, E. Acuay, A.R. Ruiz-Salvador, Chem. Commun. (2002) 2544.
- [245] C.E. Hernandez-Tamargo, A. Roldan, N.H. de Leeuw, J. Phys. Chem. C 120 (2016) 19097.
- [246] R. Grau-Crespo, S. Hamad, C.R.A. Catlow, N.H. de Leeuw, J. Phys. Condens. Matter 19 (2007) 256201.
- [247] P. Ravindran, L. Fast, P.A. Korzhavyi, B. Johansson, J. Wills, O. Eriksson, J. Appl. Phys. 84 (1998) 4891.
- [248] W. Voigt, Lehrbuch Der Kristallphysik, Leipzig, Berlin, 1928.
- [249] R. Arletti, O. Ferro, S. Quartieri, A. Sani, G. Tabacchi, G. Vezzalini, Am. Mineral. 88 (2003) 1416.
- [250] K. Niwa, T. Tanaka, M. Hasegawa, T. Okada, T. Yagi, T. Kikegawa, Microporous Mesoporous Mater. 182 (2013) 191.
- [251] S.F. Pugh, Philos. Mag. 45 (1954) 823.
- [252] C. Sanchez-Valle, S. V. Sinogeikin, Z.A.D. Lethbridge, R.I. Walton, C.W. Smith, K.E. Evans, J.D. Bass, J. Appl. Phys. 98 (2005) 53508.
- [253] Y. Huang, E.A. Havenga, Chem. Phys. Lett. 345 (2001) 65.
- [254] I.R. Shein, A.L. Ivanovskii, Scr. Mater 59 (2008) 1099.

- [255] A. Roldan, D. Santos-Carballal, N.H. de Leeuw, *J. Chem. Phys.* 138 (2013) 204712.
- [256] S.R. Bare, S.D. Kelly, W. Sinkler, J.J. Low, F.S. Modica, S. Valencia, A. Corma, L.T. Nemeth, *J. Am. Chem. Soc.* 127 (2005) 12924.
- [257] G. Yang, E.A. Pidko, E.J.M. Hensen, *J. Phys. Chem. C* 117 (2013) 3976.
- [258] Y. Huang, Z. Jiang, *Microporous Mater.* 12 (1997) 341.
- [259] Y. Qiao, Z. Fan, Y. Jiang, N. Li, H. Dong, N. He, D. Zhou, *Chinese J. Catal.* 36 (2015) 1733.
- [260] M. Hunger, J. Kärger, H. Pfeifer, J. Caro, B. Zibrowius, M. Bülow, R. Mostowicz, *J. Chem. Soc. Faraday Trans. 1 Phys. Chem. Condens. Phases* 83 (1987) 3459.
- [261] A.A. Sokol, C.R.A. Catlow, J.M. Garces, A. Kuperman, *J. Phys. Chem. B* 102 (1998) 10647.
- [262] J. To, A.A. Sokol, S.A. French, C.R.A. Catlow, *J. Phys. Chem. C* 111 (2007) 14720.